PNNL-32984

Final Report: Improved Understanding of Zircaloy Hydrogen Pickup Mechanisms in BWRs

NSUF Report

June 2022

Ramprashad Prabhakaran
Greg Coffey
Olga Marina
John Hardy
Dan Edwards
Andy Casella

Prepared for the U.S. Department of Energy
under Contract DE-AC05-76RL01830

PACIFIC NORTHWEST NATIONAL LABORATORY
operated by
BATTELLE
for the
UNITED STATES DEPARTMENT OF ENERGY
under Contract DE-AC05-76RL01830

Printed in the United States of America

Available to DOE and DOE contractors from
the Office of Scientific and Technical
Information,
P.O. Box 62, Oak Ridge, TN 37831-0062
www.osti.gov
ph: (865) 576-8401
fox: (865) 576-5728
email: reports@osti.gov

Available to the public from the National Technical Information Service
5301 Shawnee Rd., Alexandria, VA 22312
ph: (800) 553-NTIS (6847)
or (703) 605-6000
email: info@ntis.gov
Online ordering: http://www.ntis.gov

Final Report: Improved Understanding of Zircaloy Hydrogen Pickup Mechanisms in BWRs

NSUF Report

June 2022

Ramprashad Prabhakaran
Greg Coffey
Olga Marina
John Hardy
Dan Edwards
Andy Casella

Prepared for
the U.S. Department of Energy
under Contract DE-AC05-76RL01830

Pacific Northwest National Laboratory
Richland, Washington 99354

Executive Summary

Using an instrumented autoclave operating at 288°C and 1100 psi, electrical impedance spectroscopy (EIS) measurements were taken from three neutron irradiated fuel channel samples (Zircaloy-2 and Zircaloy-4). The three high priority fuel channel samples were tested at 288°C using a simulated PWR water with the AC frequency range extending down through 10^{-4} Hz, with corresponding DC measurements to validate the resistance measurements. EIS measurements were also taken at room temperature using a simulated PWR water from four neutron irradiated fuel channel samples (Zircaloy-2 and Zircaloy-4). and four water rod samples (Zircaloy-2). EIS measurements were also performed on unirradiated Zircaloy-2 tubes that were previously oxidized in autoclaves at various temperatures for different time durations to obtain oxide layers of different thicknesses.

These experiments proved to be more challenging than anticipated because of the small size of the samples, which required development of fixtures to allow valid testing of the materials, some of which are radioactive, under pressure and temperature.

Equivalent circuits were used to model the data. Some samples resulted in Nyquist plots where the arcs were too close to each other resulting in the inability to separate the different oxide morphological thicknesses.

Microstructural characterization in the form of optical microscopy, scanning electron microscopy and (scanning) transmission electron microscopy was performed to document the microstructural features of the oxidized Zr-2 and Zr-4 samples (oxide and metal/oxide interface) and to interpret the EIS results.

At the start of this work, it was assumed that despite the laminar cracks and porosity visible in both optical and SEM, the oxide scale is dense near the metal, effectively preventing the water from contacting the metal directly. While it is generally accepted that the large laminar cracks pores allow the water to percolate into the oxide film, it is unknown just how deep it can go, and how interconnected is the porosity, which will dictate how much the porosity is connected electrically to the water within the oxide scale. The EIS results demonstrated that there is in fact a distribution of oxide thicknesses over the various samples, and within each material condition, that are communicating to the liquid. This is derived from the fact that Nyquist plots have an arc radius whose center point is often below the Z’ axis, implying that instead of a single oxide thickness, these oxides have a distribution of thicknesses. This distribution of thicknesses produces arcs that are not clearly separable in most of the samples.

Acronyms and Abbreviations

AC	alternating current
BWR	Boiling Water Reactor
DC	Direct current
EIS	electrochemical impedance spectroscopy
eV	electron volt
°C	degree Celsius
HPUF	Hydrogen Pickup Fraction
LOCA	Loss of Coolant Accident
LWR	Light Water Reactor
nm	nanometer
NRC	Nuclear Regulatory Commission
Ω	ohmic resistance
PWR	Pressurized Water Reactor
RIA	Reactivity Insertion Accident
SEM	scanning electron microscopy
TEM	transmission electron microscopy
STEM	scanning transmission electron microscopy
Zr-2	Zircaloy-2 alloy
Zr-4	Zircaloy-4 alloy

Contents

Figures

Tables

1.0 Introduction

Zr-base alloys are used in Light Water Reactors (LWRs) as fuel cladding and fuel structural materials such as channels, water rods and spacers. Zircaloy-2 material is mainly used in BWRs and Zircaloy-4 is used in both BWRs and PWRs. In the high temperature reactor coolant environment, Zr-based alloys form a uniform corrosion layer, concurrently picking up hydrogen as a part of the corrosion process. The uptake of hydrogen in Zr-based alloys leads to the formation of zirconium hydrides, causing significant degradation of the mechanical properties of the material accentuated by neutron irradiation. Zircaloy-2 often exhibits high hydrogen pickup under BWR irradiation conditions, up to 80% hydrogen pickup fraction (HPUF) from the corrosion process. However, it is difficult to reliably predict the HPUF fraction due to the large variation that occurs at high fuel burnups (see Figure 1) [1], possibly due to different operational parameters and variations in the material processing and starting chemistry. The hydrogen pickup mechanism of Zr-based alloys is a complex phenomenon and is still not clearly understood after decades of research. An improved understanding of hydrogen pickup in Zr-based alloys have a strong impetus as it is important to the nuclear industry given the on-going Nuclear Regulatory Commission (NRC) loss of coolant accident (LOCA) rulemaking and new reactivity insertion accident (RIA) acceptance criteria. Each of these have limiting metrics that are tied to the hydrogen content of the fuel cladding and highlight the need for predicting fuel cladding hydrogen content at the end of life [2]. The NRC's proposed new LOCA rule is shown in Figure 2. Knowledge on the mechanisms and controlling parameters responsible for the high hydrogen pickup and variability at high burnup would greatly enhance the industry's ability to predict hydrogen pickup.

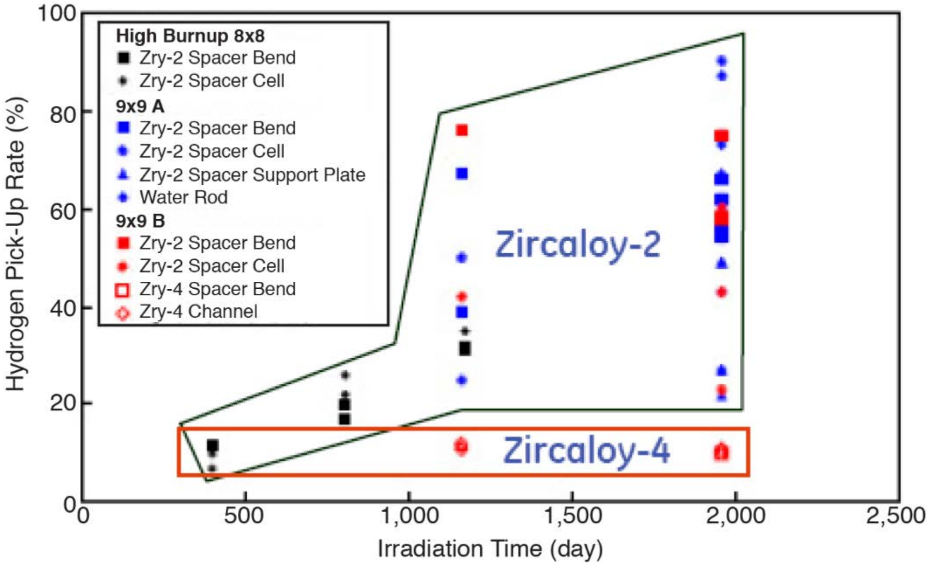

Figure 1: Hydrogen Pickup Rate vs. Irradiation Time for Non-Heat Transfer Fuel Components[1].

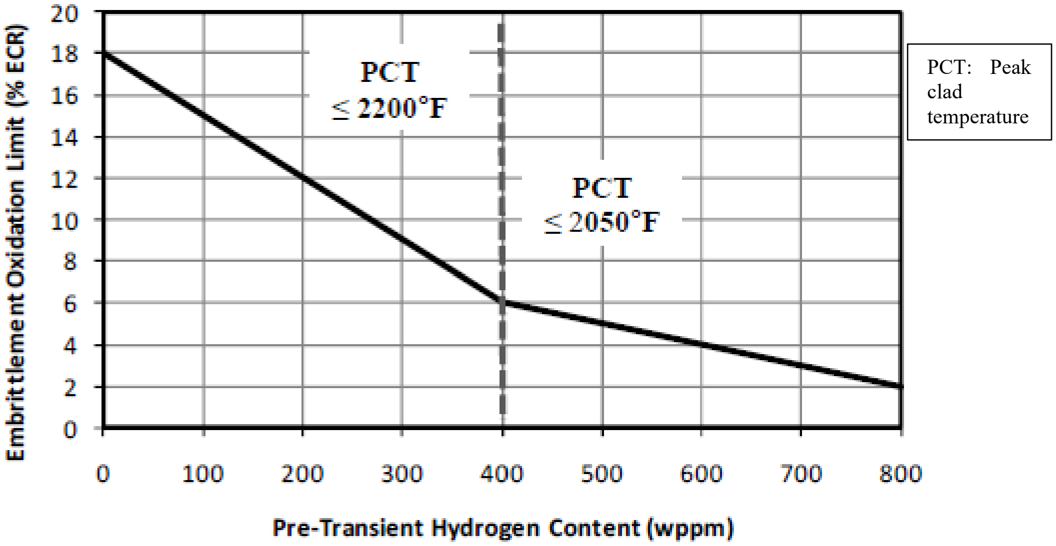

Figure 2: Allowable Equivalent Clad Reacted (%) (Percentage of Cladding Oxidized) decreases with hydrogen content and therefore NRC's upcoming new LOCA regulation will be hydrogen content dependent (rather than current requirement of 17% ECR)[2].

What is needed?

As mentioned above, although Zircaloy oxidation and the associated hydrogen uptake have been studied for the past 60 years, a complete understanding of the mechanisms involved in H uptake is still missing. Notably, the mechanisms and the chemical state (H^+ or H^0) related to hydrogen migration through the oxide layer are not yet elucidated, which makes it difficult to predict hydrogen content of the cladding to assure compliance with the new LOCA requirements shown in Figure 2.

The current consensus is that during aqueous corrosion, the hydrogen that is absorbed into the metal is a fraction of the H produced by oxidation and hence the H pickup fraction is used to describe the H uptake, which is specific to the particular Zr alloy and also could depend on heat flux, boiling, and coolant chemistry [3]. In BWRs, it is also generally accepted that Zircaloy-2 has a larger HPUF than Zircaloy-4, an alloy variant that does not incorporate Ni as an alloying element after early studies revealed that Ni promoted H uptake [1]. On the other hand, Nb in Zr-Nb alloys, which is mainly used in Pressurized Water Reactors (PWRs), proved to be an inhibitor of H uptake and reducing oxidation [3].

There are several hypotheses that have been proposed to explain the Ni effect on H uptake in Zircaloy-2. One of these is the segregation of metallic Ni and Fe as filaments along oxide grain boundaries after dissolution of SPPs, which would create shortcuts for H ingress (aka "Ni band" hypothesis) [4]. The authors of this project report and our collaborators have conducted a series of irradiated Zircaloy-2 characterization previously to support the "Ni band" hypothesis. Although much supporting evidence for this hypothesis was observed such as high metallic Ni in high HPUF Zircaloy-2 from the x-ray absorption near edge spectroscopy (XANES) measurements [5], no "Ni bands" were found in the oxide using 3D atom probe tomography (3DAPT) and transmission electron microscopy (TEM) [6]. The analysis of results indicates that different roles for Ni and Fe may exist in the Zircaloy-2 hydrogen pickup mechanism.

The other hypothesis for hydrogen pickup proposed in the literature is that metallic impurities in the oxide layer decrease the oxide resistivity, resulting in hydrogen evolution at the oxide/water interface and therefore less hydrogen pickup [7-8], schematically shown in Figure 3. Recently, in unirradiated Zircaloy-4/Zr-2.5Nb exposed to PWR conditions in laboratory autoclave studies, Couet et al. [7-8] showed a positive correlation between the oxide resistivity and the hydrogen pickup fraction, i.e., the higher the oxide resistivity, the higher the hydrogen pickup fraction. In addition, the authors found more Nb in solution in the Zr-2.5Nb oxide than Fe dissolved in the Zircaloy-4 oxides using X-ray absorption near edge spectroscopy (XANES). This is attributed in [7-8] to the doping effect of Nb aliovalent ions (+5 charge), which being embedded in the oxide, decrease the degree of positive space charge in the oxide and thus lower the electronic oxide resistivity. The basis for this inference is the assumption that H^+ is the species that migrates through the oxide unless it is discharged by an incoming electron, as shown in Figure 3 below. Consequently, the electric field across the oxide (the driving force for proton absorption in the oxide) is lower in Zr-2.5Nb alloys and thus fewer protons are absorbed leading to a lower hydrogen pickup fraction. In the case of Zircaloy-4, there are not enough Fe or Cr aliovalent ions embedded in solid solution in the oxide to compensate the space charges because of their extremely low solubility limit in Zr metal (at least an order of magnitude lower than the Nb solubility limit). The electric field would be higher in Zircaloy-4 than in the oxide of Zr-2.5Nb.

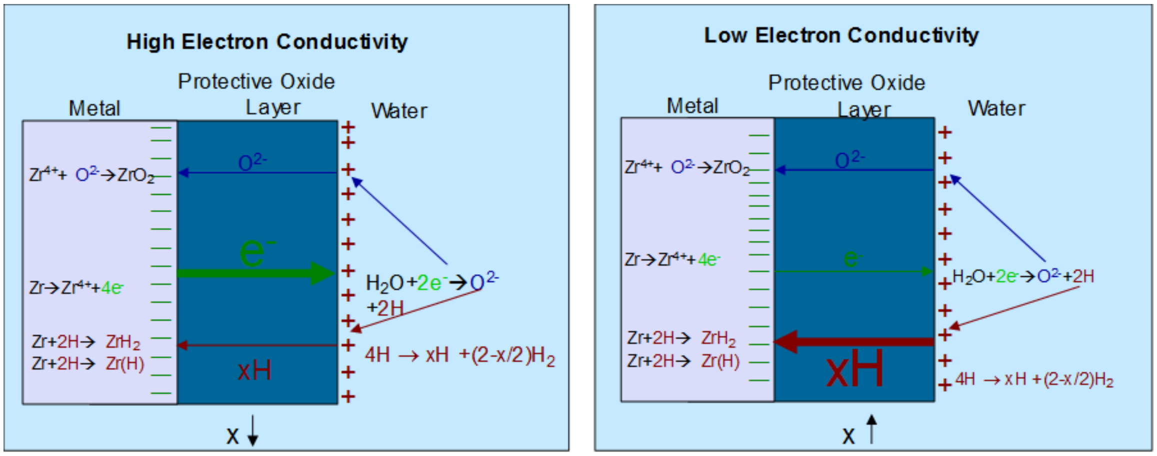

Figure 3: Schematics of hypothesis on oxide electron conductivity and hydrogen pickup relationship. *Derived from recent work by Couet* [7-8].

These correlations in references [7-8] are only valid for a couple of alloys tested in out-of-core autoclave environment in PWR conditions. It is not known if this correlation is generic for all other Zirconium alloys, including Zircaloy-2, under irradiation conditions, and in different aqueous environments. As part of the systematic study performed [5], synchrotron XANES measurements performed on various Zircaloy-2 oxides showed a positive correlation between high metallic Ni content in oxide layers with the material hydrogen pickup fraction (higher metallic Ni content in oxides, correlated to higher hydrogen pickup). Based on the electron conductivity hypothesis discussed above, lower electrical resistance would be expected in the oxide layer with higher metallic Ni content due to the existence of metallic Ni in the oxide layer [5]. The apparent conflict between the two different observations needs to be investigated further to understand the hydrogen pickup mechanism.

Prior to Couet et al. [7-8], several authors investigated the electrochemical nature of the Zircaloy oxide layers and a few of them are in references [9-11]. However, previous investigators were mainly focused on understanding the corrosion mechanism rather than understanding the hydrogen pickup mechanism. There are limited studies in the literature investigating irradiated Zircaloy-2 materials with different hydrogen pickup behavior to understand the hydrogen pickup mechanisms.

Currently efforts are ongoing to investigate whether there is a correlation between oxide resistivity and Zircaloy hydrogen pickup in irradiated Zircaloy-2 materials using in-situ electrochemical impedance spectroscopy (EIS) to confirm or refute the electron conductivity hypothesis, which is shown schematically in Figure 3.

The other hypothesis that needs to be studied is the catalytic effect of Ni on H_2 dissociation (or alternatively, hindrance of H recombination) [12,13]. This catalytic effect is well known and researched in the hydrogenation studies [14,15] but has not been clearly associated with H uptake in Zircaloy-2. It was proposed in references [12,13] that Ni present on free surfaces, either external or internal surfaces (created by cracking/pores) acts to prevent H recombination and hence promote H ingress and lead to a higher pickup fraction. In that respect, it was also proposed in the literature that Nb plays an opposite role on the oxide surfaces [16]. It is also necessary to perform a detailed review of the available hypotheses on the role of Ni and Fe on Zircaloy-2 hydrogen pickup.

The goal of this work was to measure the resistivity of the oxide films present on unirradiated Zr-2 tubes, irradiated Zr-2 and Zr-4 fuel channels and irradiated Zr-2 water rod samples using electrochemical impedance spectroscopy under autoclave testing conditions (288°C and ~1100 psi) and at room temperature in air. These measurements were performed on various fuel channel and water rod materials extracted from commercial BWRs to provide additional information to deepen our understanding on the role of various morphological features of the oxide layer. An integral part of this effort was to document the microstructure and microchemistry of the oxide and underlying Zircaloy matrix using advanced characterization tools and relate this to the measured oxide electrochemical response.

2.0 Materials

2.1 Irradiated Zircaloy-2 and Zircaloy-4 fuel channels

PNNL performed autoclave testing and microstructural characterization on two irradiated BWR Zircaloy-2 and two irradiated BWR Zircaloy-4 fuel channel coupons. Irradiation history, alloy composition, hydrogen pickup fraction and measured oxide thickness of these fuel channel coupons are provided in Table 1. These fuel channel coupons were extracted by electrical discharge machining (EDM) from fuel channels removed from a BWR. Each coupon was sectioned by a third-party vendor as a part of prior characterization program for the PIs and was marked with an orientation tail to help determine the orientation of outer and inner oxide scales. In this case, the inner oxide scale is on fuel channel's interior side that faces toward fuel rod assemblies, and the outer oxide scale faces adjacent control rod blades and/or nearby fuel channels. Each coupon contained base metal, weld and heat affected zone (HAZ). The hook-shaped orientation mark always points towards the base metal, as shown in Figure 4.

Table 1: Fuel channel coupons studied at PNNL

	Zirc-4 Archive	Zirc-2 Archive	Material 12	Material 12-1	Material 16	Material 16-1
Short ID Code			**12C**	**12A**	**22C**	**22A**
Material Type	Zirc-4	Zirc-2	Zirc-4	Zirc-4	Zirc-2	Zirc-2
Channel Side	n/a	n/a	Opposite Side	CRB	Opposite Side	CRB
Sample Elevation (inches from bottom)	n/a	n/a	55	55	55	55
Elevation where fluence was calculated (inches from bottom)	n/a	n/a	55	55	55	55
Fluence at sample elevation (10^{21} n/cm^2)	n/a	n/a	9.01	9.067	8.454	8.517
Reported outer oxide (µm)	n/a	n/a	67	72	8	42
Reported inner oxide (µm)	n/a	n/a	50	29	5	9
Elevation where Hydrogen Pickup (HPU) was measured	n/a	n/a	55	55	55	55
Component thickness (mils)	80	80	80	80	80	80
Corrected HPU	n/a	n/a	72.8	69.6	124.8	191.2
HPU (%)	n/a	n/a	n/a	80	14	44
Bundle ID/Channel ID or sample ID	4155J	6602J	4155J	4155J	6602J	6602J

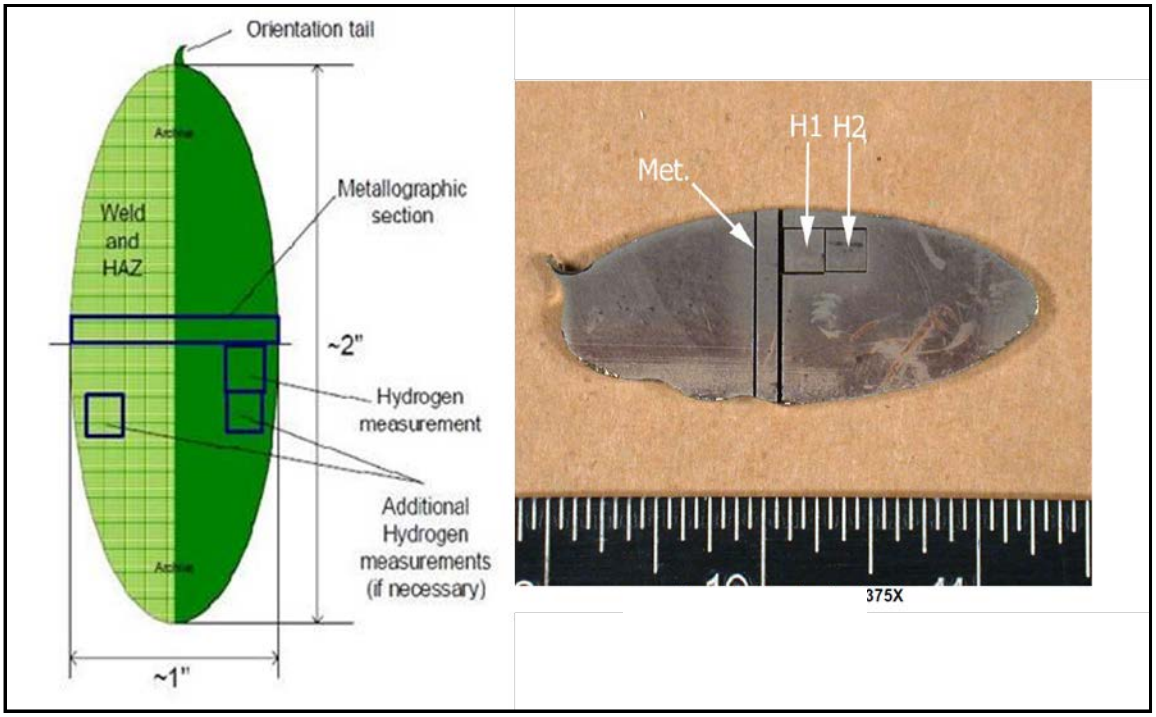

Figure 4: An example of an irradiated coupon removed from fuel channels showing rectangular specimens (right side; H1, H2, Met) utilized for previous study (blue boxes; left side). Coupon image was provided by original vendor and not identified as to which coupon.

Two Zircaloy-2 fuel channel coupons were removed from the same irradiated fuel channel at the elevation listed in Table 1, with each side experiencing nearly identical neutron fluences. One coupon was taken from a side adjacent to the control blade (CB), potentially experiencing enhanced shadow corrosion, and the other was taken from the opposite side where no fuel channel was present. A similar set (CB side and opposite side coupons) were extracted from a single BWR Zircaloy-4 fuel channel.

One-fourth of each of the irradiated fuel channel was utilized for the current study (performing electrochemical testing), as shown in Figure 5. The dose rates of each sample (one quarter) ranged from 50-80 mrem/hour @ contact and less than 5 mrem/hour @ 30 cm. The photographs of fuel channel samples (22A, 22C, 12A and 12C; Material #16-1, #16, #12-1 and #12) are shown in Figure 6-Figure 9.

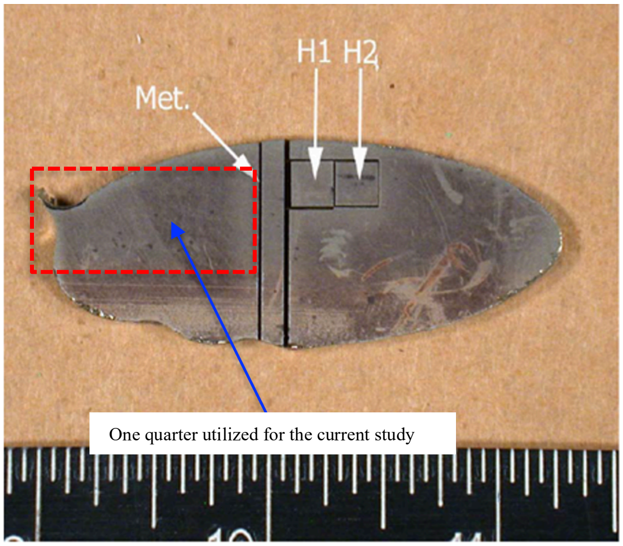

Figure 5: One-quarter of each irradiated fuel channel coupon utilized for the current study; H1, H2 and Met specimens utilized for previous study

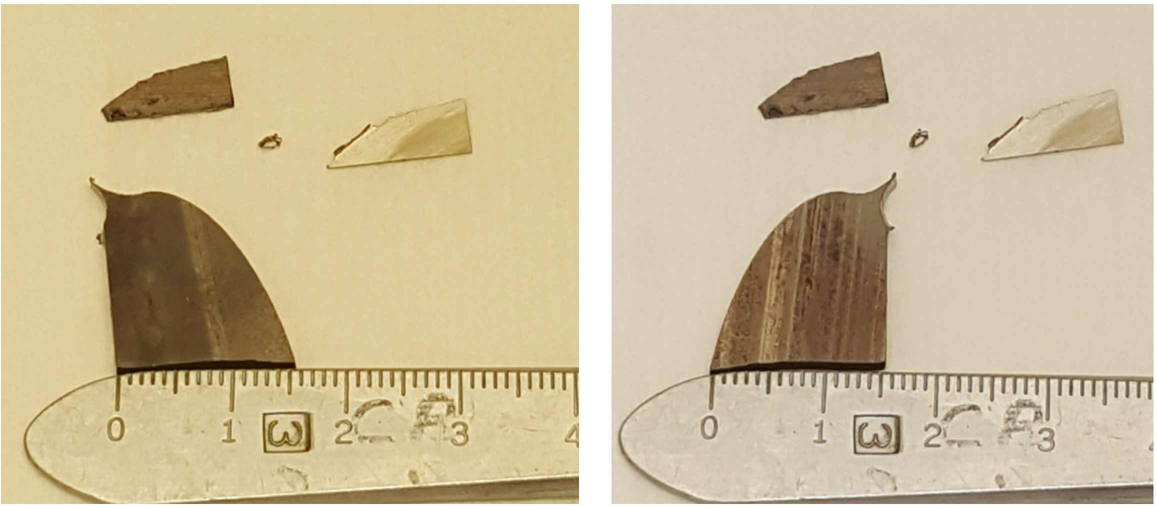

Figure 6: Irradiated fuel channel sample 22A (Material 16-1)

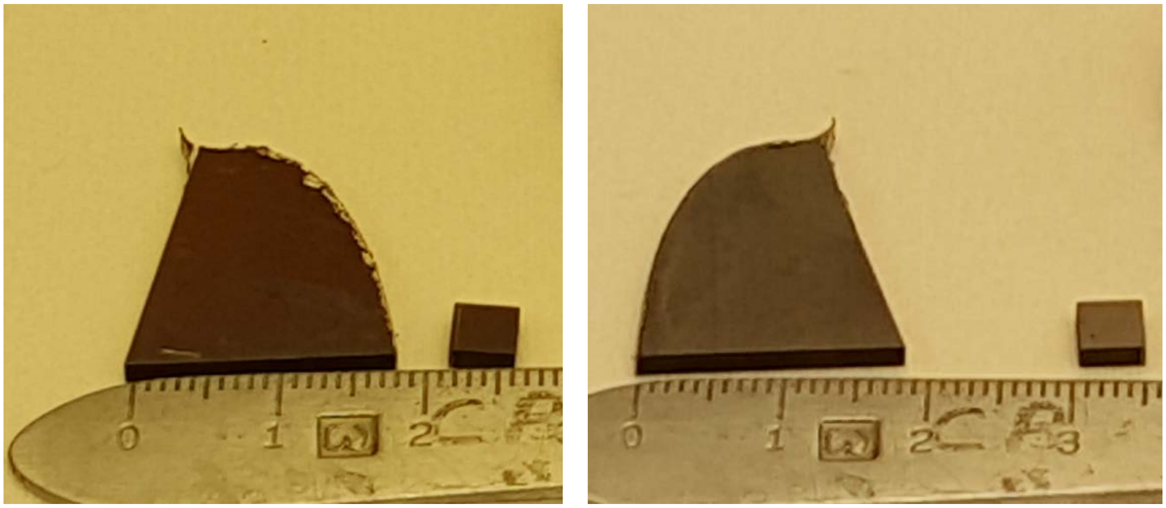

Figure 7: Irradiated fuel channel sample 22C (Material 16)

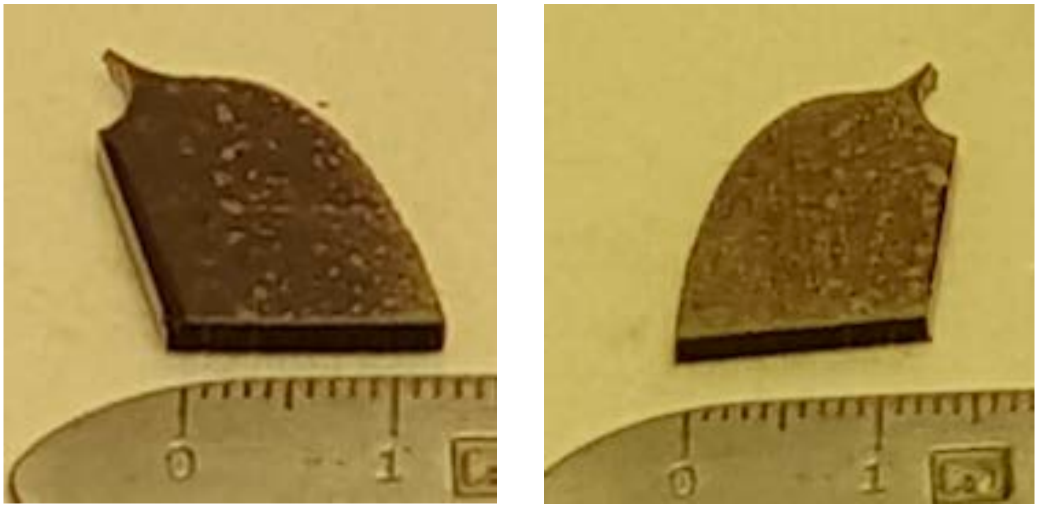

Figure 8: Irradiated fuel channel sample 12A (Material 12-1)

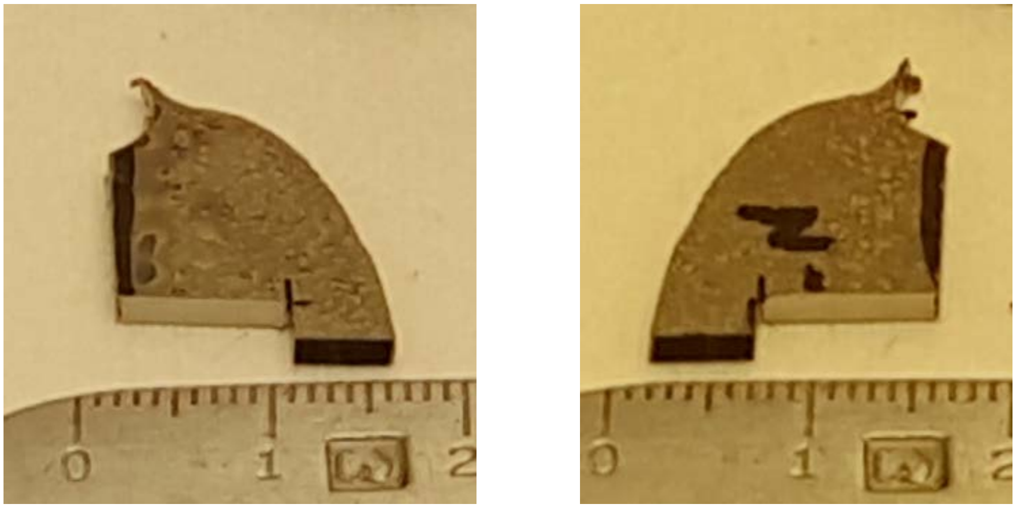

Figure 9: Irradiated fuel channel sample 12C (Material 12)

2.2 Irradiated Zircaloy-2 water rods

Four irradiated Ziraloy-2 water rod samples available at PNNL as a part of a prior PIE campaign by the principal investigators were also utilized for this study. These samples were in the form of small sections obtained from hollow irradiated water rods. Details on their irradiation history, oxide thickness and hydrogen pickup fraction are provided in Table 2. Dose rate measurements were taken for each of four water rod samples selected for corrosion testing. The dose rates of each sample ranged from 2-20 mrem/hour @ contact and less than 1 mrem/hour @ 30 cm. The photographs of irradiated water rod samples (Archive 1, Material # 10, 13, 17 and 21) are shown in Figure 10-Figure 15.

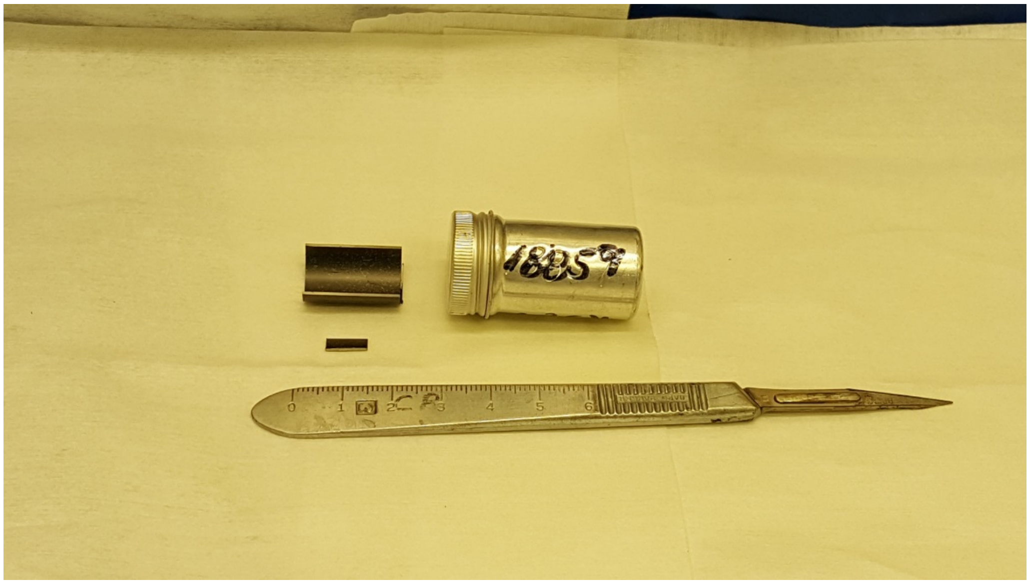

Figure 10: Irradiated water rod # 18859 (Archive 1)

Figure 11: Irradiated water rod # 18859 (Archive 1) – Other views

Table 2: Water rod (Zircaloy-2) samples tested at PNNL

	Archive 1	Material 10	Material 13	Archive 2	Material 17	Material 21
Sample Elevation (in. from bottom)	2.4	42.7	51.525	1.6	110.1	110.02
Elevation where fluence was calculated (inches from bottom)	6	40	50	6	110	110
Fluence at sample elevation (10^{21} n/cm^2)	2	9.7	13.1	2.0	7.05	9.4
Elevation where oxide thickness was measured (inches)	6	40	50	6	100	110
Reported outer oxide (µm)		23	27		3.5	16
Reported inner oxide (µm)		22	29		3	9
Elevation where HPU was measured (inches from bottom)	not measured	40	50	not measured	100	110
Component thickness (mils)	30	30	30	30	30	30
Measured HPU		250	1033		67	622
HPUF (%)		17.6	46.6		15.4	61.1
Bundle ID/Channel ID or sample ID		YJ1433/ K2086	YJ1377/ M584		LY5456	LY5455

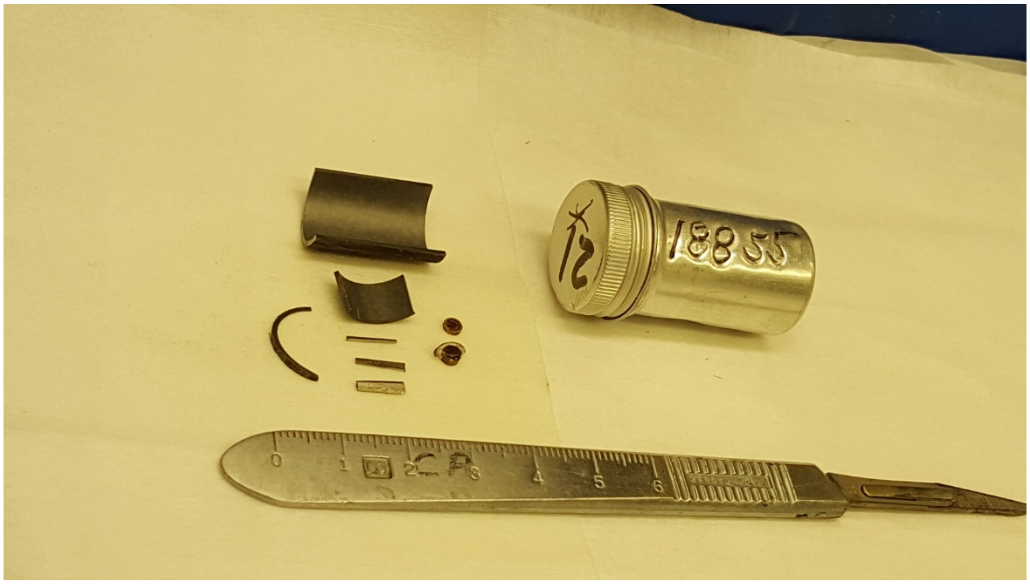

Figure 12: Irradiated water rod # 18855 (Material 21)

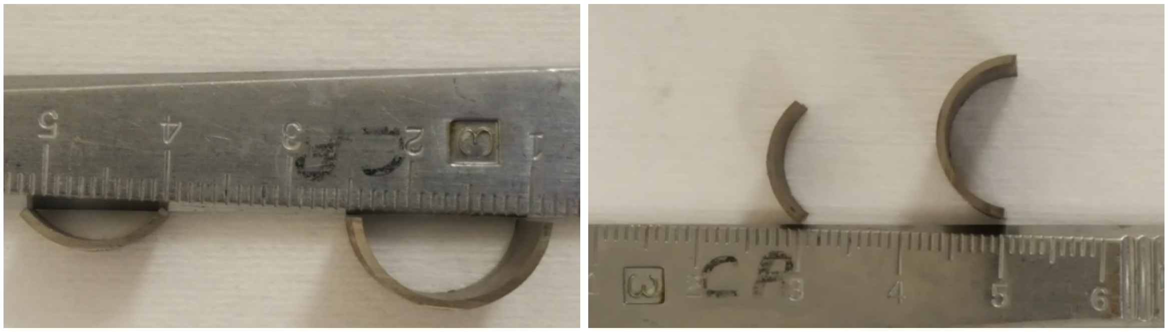

Figure 13: Irradiated water rod # 18855 (Material 21) – Other views

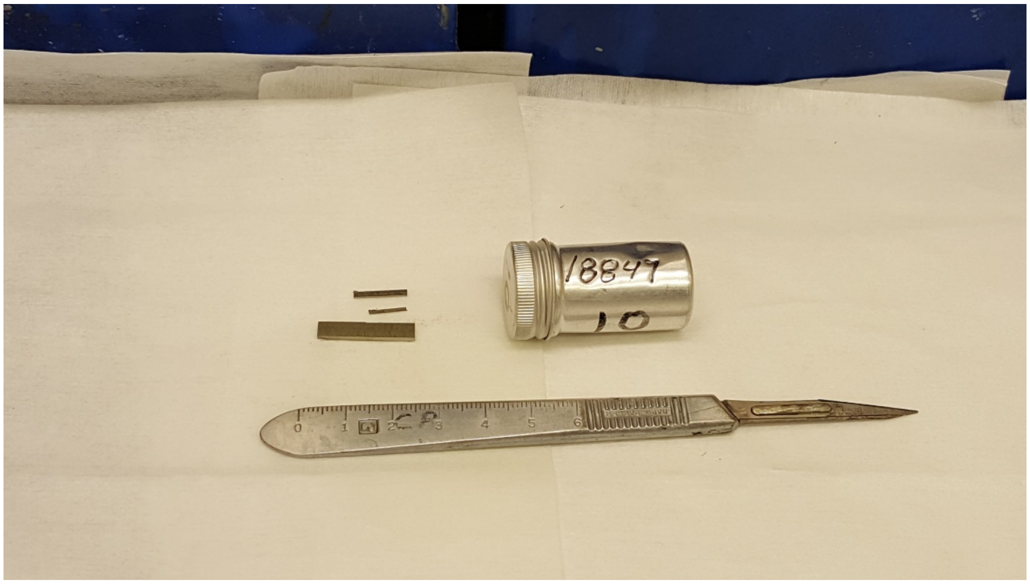

Figure 14: Irradiated water rod # 18847 (Material 10)

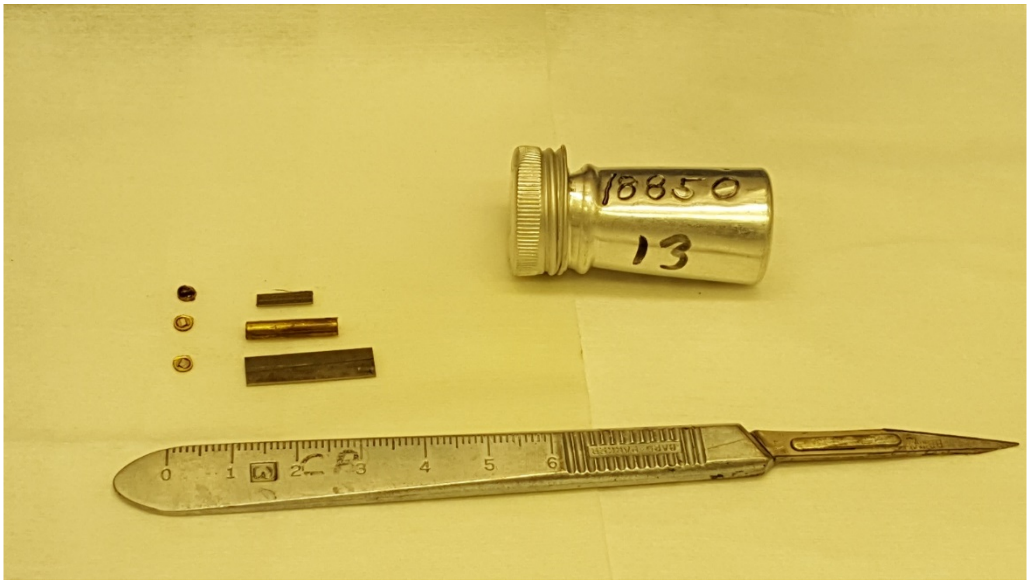

Figure 15: Irradiated water rod # 18850 (Material 13)

2.3 Unirradiated oxidized Zircaloy-2 tubes

PNNL received three unirradiated Zircaloy-2 tubes during November 2019 from Studsvik as per EPRI's request. These tubes were previously oxidized in autoclaves at Studsvik at various temperatures for different time durations to obtain oxide layers of different thicknesses.

- Zr-2; 50 mm tube; RR2015; 303-06085; A_o 83730-2; 500°C for 72 days (5-9 µm oxide layer)
- Zr-2; 50 mm tube; RR2013; 303-06979; A_o 82295; 400°C for 3 days (1 µm oxide layer)
- Zr-2; 20 mm tube; RR2013; 303-06979; A_o 82295; 415°C for 90 days (6 µm oxide layer)

Images for each of the three sets of samples are provided in Figure 16-Figure 18.

Figure 16: Unirradiated oxidized Zr-2 tube (500°C for 72 days; 5-9 µm oxide layer)

Figure 17: Unirradiated oxidized Zr-2 tube (400°C for 3 days; 1 µm oxide layer)

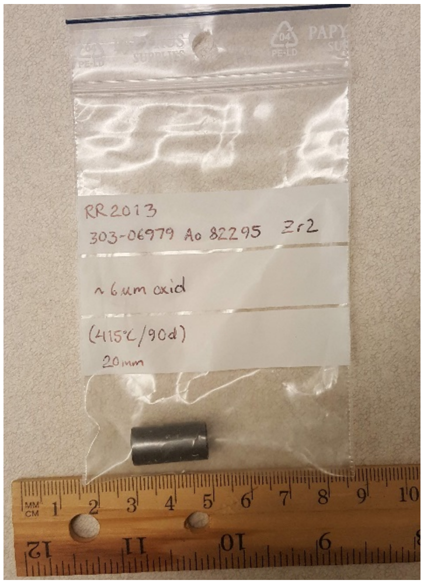

Figure 18: Unirradiated oxidized Zr-2 tube (415°C for 90 days; 6 µm oxide layer)

2.4 Unirradiated Zircaloy-4 plate

One unirradiated Zircaloy-4 plate (E9885; 205187; 4155J; 11540) obtained from EPRI was also utilized for this study. An image of the plate is provided in Figure 19.

Figure 19: Unirradiated Zr-4 plate (E9885; 205187; 4155J; 11540)

3.0 Experimental Methods

3.1 Electron Microscopy

One variable that needs to be explored is the influence of interconnected porosity and cracks on the measured electrical resistivity measurements. If the reactor water penetrates close to the metal/oxide interface due to interconnected porosity, then the oxide scale resistance will be heavily influenced by the degree of contact between the water filled porosity/cracks, the metal/oxide interface, and the relative area fraction of dense oxide that exists between the metal and porous oxide scale.

Scanning electron microscopy (SEM) analysis was conducted to document the degree of porosity within the oxide scales of the various samples upon which EIS tests were performed, the ultimate goal of which was to determine how close the cracks and pores in the oxide are to the metal/oxide interface. The samples were prepared by cutting cross-sections that included the outer and inner oxide scales, allowing us to measure the oxide scale thickness and distribution of porosity within each sample. The samples were vacuum impregnated with epoxy, mounted in epoxy, and ground through successive SiC grits for a rough polish, then polished mechanically to a final colloidal silica finish that allows nanoscale features to be observed. The SEM analysis was conducted on the JEOL 7500F field emission gun SEM at 20 keV using a moderate beam current of 10-20 nA to achieve good contrast in backscatter electron mode. An accelerating voltage of 20 keV yielded the best images of the porosity and laminar cracks in the oxide scale, penetrating 2-3 µm into the polished surface to reveal pores down to 20 nm or less in length. No elemental maps or chemistry were obtained, the focus was strictly upon the oxide structure. Prior work showed that the chemical impurities were at such low levels that elemental analysis yielded little additional information beyond the basic Zr and O contents. The second phase particles could sometimes be observed in the elemental maps, especially the Cr-rich remnants, but not at sufficient detail to confirm their size and distribution.

Transmission electron microscopy analysis was conducted to document the distribution of cracks and pores that are too small to resolve in the SEM. Most imaging was conducted in scanning transmission electron microscopy (STEM) imaging mode, where STEM high angle annular dark field and bright imaging were performed to ascertain the extent of porosity in the oxide film, documenting the size of the pores, their spatial distribution with respect to the metal oxide interface, and if nanopores were present at the metal/oxide interface. Phase contrast imaging in TEM mode was also used to a limited extent, which reveals nanoscale and larger pores/cracks by their Fresnel contrast fringes.

A TEM lamella was prepared from mounted and polished cross sections from each of the three fuel channel coupons and the unirradiated Zr-2 20 mm tube (RR2013, 303-06979) using a FEI Quanta 3D FIB/SEM. Before trenching, a 1.5 µm carbon (C) cap was placed on the surface over the desired location, followed by a 1.5 µm platinum (Pt) cap. The two caps were used to reduce curtaining during thinning, and to provide an amorphous structure for Ronchigram correction during scanning transmission electron microscopy (STEM) alignment. Using a Pt weld, the lift-out was attached to a standard Cu FIB liftout grid. An accelerating voltage of 30 keV was utilized for reducing thickness to 350 nm, followed by 5 keV for further reduction to < 150 nm. A final 2 keV cleanup procedure was employed on each side of the lamella to reduce FIB-induced artifacts. A U-shaped rim structure was left around the edge of the sample to provide support to prevent buckling of the foil due to residual stress.

3.2 Specimen Preparation for Electrochemical Corrosion Testing

Based upon the discussion with EPRI, it was decided to begin electrochemical corrosion testing with irradiated specimens obtained from fuel channel coupons first prior to water rods due to its relatively simpler geometry. Neutron-irradiated specimens were prepared using appropriate radiological laboratory fume hoods and equipment approved for handling radiological specimens.

Initial irradiated fuel channel specimen preparation for electrochemical corrosion testing using EIS in a pressurized autoclave involved various stages as described below. This method was designated as Method #1.

3.2.1 Electrochemical Corrosion Specimen Preparation Method # 1

3.2.1.1 Specimen configuration

As per the Method #1, all four cut surfaces have bare metal exposed. The thinner oxide layer on the fifth side (top) should be ground at least partially to perform spot welding. The sixth side (bottom) is the thicker oxide layer to be studied. A schematic and an example of this method (#1) are shown in Figures 20 and 21.

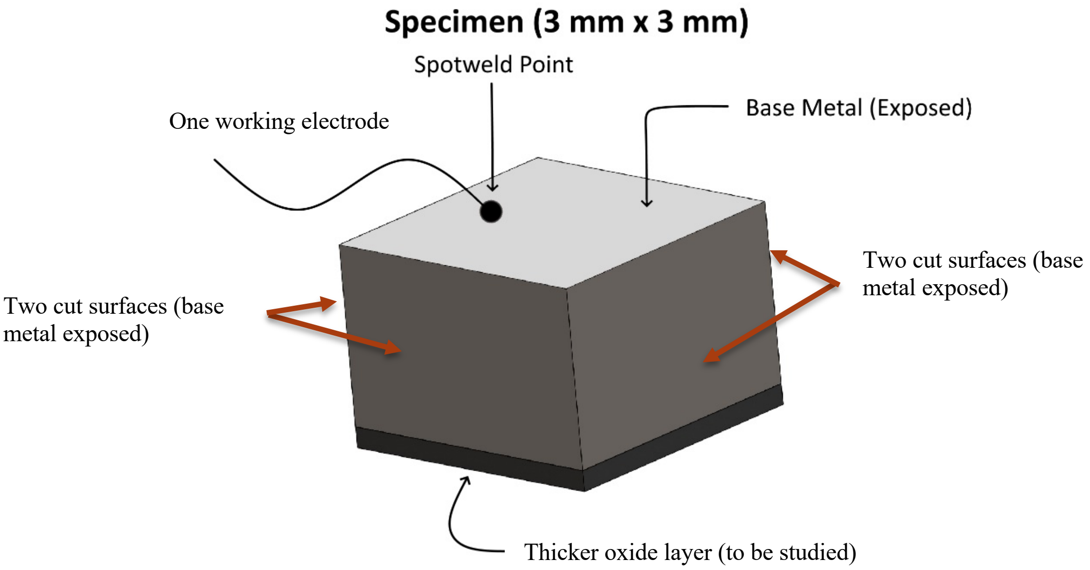

NOTE: All four cut surfaces have bare metal exposed; thinner oxide layer on the fifth side (top) was ground to perform spot welding; the sixth side (bottom) is the thicker oxide layer to be studied.

Figure 20: Irradiated fuel channel specimen configuration (Method #1)

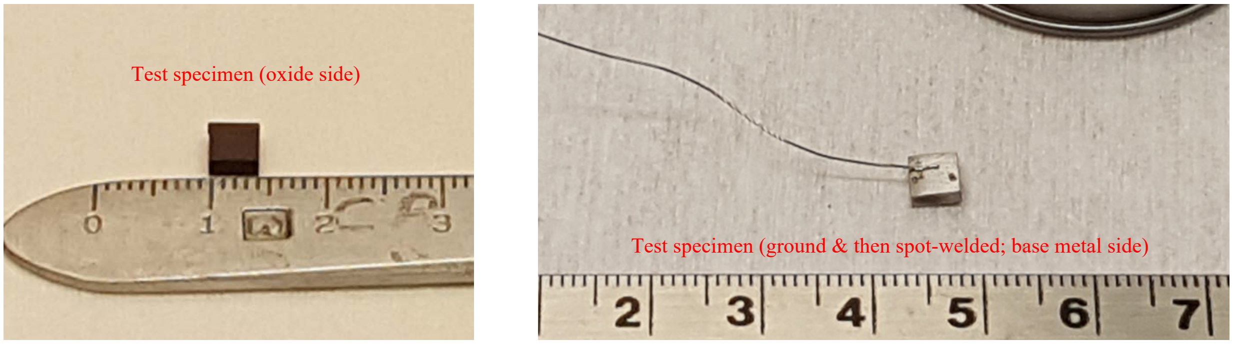

Figure 21: Irradiated fuel channel test specimen before and after spot welding (Method #1)

3.2.1.2 Specimen sectioning

A low-speed diamond saw inside a radiological laboratory fume hood was utilized for sectioning small pieces from irradiated fuel channel coupons for electrochemical corrosion testing. Efforts were made to section pieces of size approximately 4 mm x 4 mm carefully from the base metal without damaging the outer/thicker oxide layer. Tweezers were employed to minimize dosage to extremities while handling specimens. Special attention was given while choosing blades and speed to protect the thick oxide layer from damage. It is important to avoid having burrs facing the thick oxide layer because they are difficult to remove it by grinding without potentially removing the oxide layer and thus exposing bare metal, thereby affecting the multimeter continuity test (see explanation below).

3.2.1.3 Gold coating

The resistivity of the unreacted (bulk) metal is very small when compared to that of a thin oxide film. Even when a fine mesh is used as a current collector, there is a concern that the spacing of wires in the mesh is most likely much larger than the oxide thickness. Current flows through the shortest path through the resistive oxide to the conductive substrate. Therefore, to maximize the number of electrical contacts and measure the effective resistance of the entire oxide surface plane and not a finite number of point contacts, a continuous layer of gold (10-20 nm) was sputtered onto the oxide surface.

3.2.1.4 Specimen grinding

The gold-coated (on thicker oxide side) test specimen was handled using tweezers on the outer cut edges and the thinner oxide layer (on the fuel facing side) was removed using SiC grinding paper. The objective was to remove the thinner oxide layer on the bottom face and expose a sufficient region of bare base metal (silver color) to perform spot welding. Specimen grinding was performed inside a radiological hood. Efforts were made to minimize any damage to the black or brown thicker oxide layer (top face).

3.2.1.5 Continuity test

After the thinner oxide layer was completely removed and the bare metal (silver color) was exposed, it was necessary to perform a continuity test. The objective was to ensure no continuity between the base metal and oxide layer. Generally, a continuity test could be performed using a standard multimeter, by touching one lead on the exposed base metal and the other lead on thicker oxide layer. However, it is potentially possible to damage the thicker oxide layer while using a sharp multimeter lead. In addition, it is necessary to ensure that there is no region with a damaged oxide layer (in a way that it exposes the base metal) on the test specimen.

Hence, a flat platinum foil was employed, and the test specimen was placed on the foil with the oxide layer (black or brown color) facing down. The continuity test was then performed by holding one lead onto the exposed base metal (silver color) and the other lead onto the platinum foil. If the specimen was sectioned properly without burrs and if the base metal was ground and exposed properly on one side, then there would not be any continuity between the base metal and platinum foil (due to the presence of the intervening oxide layer).

3.2.1.6 Spot welding

In an electrochemical test, the bare base metal served as the working electrode and a thin platinum (Pt) wire was spot welded to that side inside a radiological fume hood. To verify proper spot-welding operation, a continuity test was performed by holding one lead to the platinum wire spot welded to bare base metal (silver color) and the other lead on base metal directly.

A continuity test was also performed by holding one lead to the platinum wire spot-welded to bare base metal (silver color) and the other lead to the platinum foil holding the test specimen with oxide side (black or brown color) facing down. If the specimen was sectioned properly without burrs and if the base metal was ground and exposed properly on one side, then there would not be any continuity between the bare base metal and platinum foil.

3.2.2 Electrochemical Corrosion Specimen Preparation Method # 2

3.2.2.1 Coating study

After analyzing the results of a few irradiated fuel channel samples, during Summer 2019, EPRI requested to coat the four cut sides and the spot-welded side with the exposed base metal using an insulating material. Hence, PNNL conducted a study using unirradiated Zr-4 specimens to identify appropriate an insulating coating that will not deteriorate or affect electrochemical test results when tested at 288ºC (~1100 psi) in simulated PWR water. This method, designated as Method #2, involves the steps described in sections 3.2.1.1 through 3.2.1.6 plus an additional insulating coating step (see below).

3.2.2.2 Sodium silicate coating

Sodium silicate (water glass) was initially chosen to be utilized as an insulating medium (to seal the exposed base metal except the oxide layer to be studied) for the EIS test specimen. An unirradiated Zr-4 plate (E9885; 205187; 4155J; 11540) obtained from EPRI was utilized to obtain specimens for this coating evaluation study, as shown in Figure 22. A low-speed saw was used to section small test specimens (about 5 mm x 5 mm) as shown in Figure 23. Optical micrographs of six sides of an unirradiated and uncoated specimen are shown in Figure 24 and Figure 25.

One larger side was ground using successively-finer SiC papers to remove any potential oxide layer. Platinum wire was spot-welded on this larger side. Two types of sodium silicate coatings (one layer and two layers) were applied on the other larger side (opposite to the spot-welded side) and four thinner sides.

A 40 wt% solution of sodium silicate was compounded. The samples were cleaned in isopropyl alcohol, dipped into the sodium silicate solution, and treated with CO_2 in order to produce the SiO_2. Once converted to SiO_2, the samples were submerged into a 0.25 molar NaCl/water solution and a multimeter was used to confirm that the SiO_2 layer was completely insulative.

Figure 22: Unirradiated Zr-4 plate utilized for the coating study

Figure 23: Specimens obtained from unirradiated Zr-4 plate for the coating study

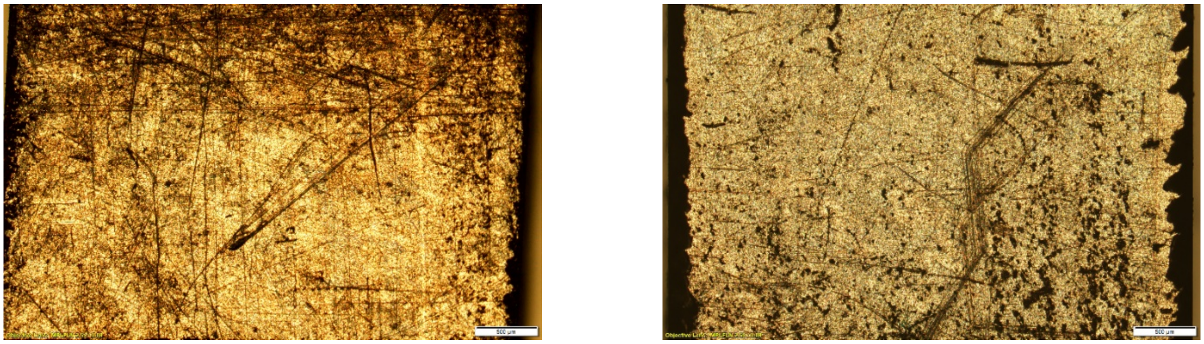

Figure 24: Uncoated Zr-4 unirradiated specimen (LHS: side 1; RHS: side 2)

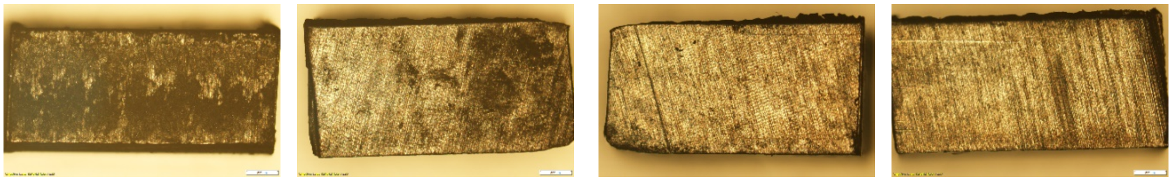

Figure 25: Uncoated Zr-4 unirradiated specimen (4 sides)

3.2.2.3 Performance check using Zr-4 specimens and autoclave

In order to evaluate the performance of sodium silicate coatings (one layer and two layers), both test specimens were inserted into Fixture #1 and kept inside an autoclave filled with PWR water at room temperature. After seven days, the temperature of the autoclave was increased from 22°C to 288°C. After exposing the coated test specimens to 288°C PWR water for 5 days, the autoclave was turned off. The coated samples were taken out of the autoclave after about 24 hours.

After autoclave performance testing of the coating, the spot-welded Pt wire was removed prior to taking optical images. Figure 26 shows the optical images of sodium silicate (one layer) coated autoclave tested (288°C; PWR water) Zr-4 specimen (LHS: side 1 spot welded - with no coating and RHS: side 2 with coating). Figure 27 shows the optical images of single-layer sodium silicate coated Zr-4 specimen (four thinner sides). As seen from these images, the sodium silicate coated sides show a pinkish shade.

Figure 28 shows the optical images of sodium silicate (two layers) coated autoclave tested (288°C; PWR water) Zr-4 specimen (LHS: side 1 spot welded - with no coating and RHS: side 2 with coating). Figure 29 shows the optical images of double layer sodium silicate coated Zr-4 specimen (four thinner sides). As seen from these images, the coated sides show a pinkish shade. The specimen surface was rough as expected for an unground and unpolished specimen. Hence, the quality of optical images was not good. Based upon optical images, it is not possible to evaluate the coating integrity with certainty.

A resistance check was performed to evaluate the effectiveness of sodium silicate coatings (single layer and double layers) after testing inside the autoclave (PWR water at 288°C). A fresh batch of NaCl solution was prepared and its resistance (measured using multimeter) was around 30 kΩ. Autoclave-tested specimens with single and double-layered water glass coating showed resistance similar to NaCl solution. Thus, the resistance check showed that the sodium silicate coating (both single and double layers) deteriorated inside the autoclave, and it is not suitable for high temperature testing in simulated PWR water.

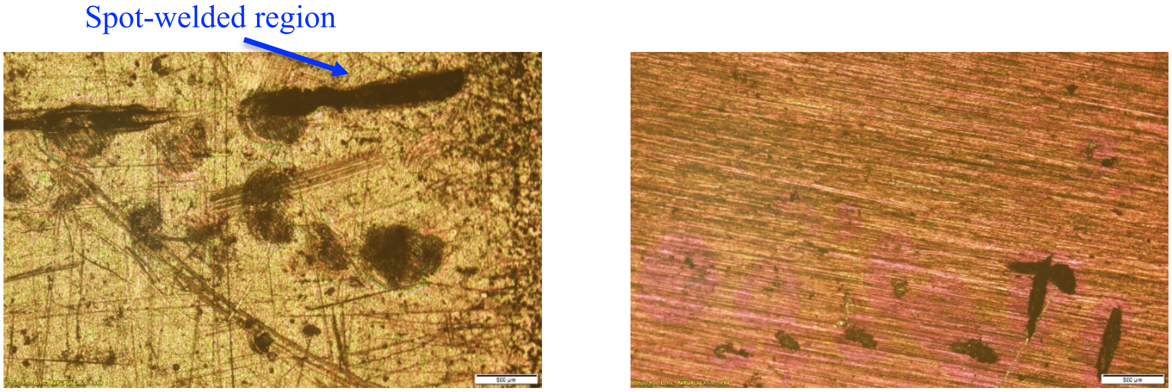

Figure 26: Sodium silicate coated (1 layer) Zr-4 unirradiated specimen after testing in autoclave (288°C; PWR water); LHS: side 1; RHS: side 2

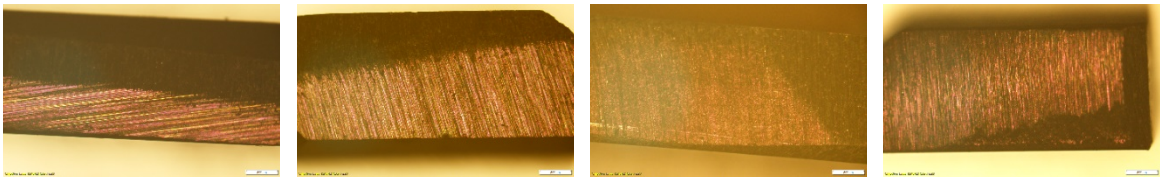

Figure 27: Sodium silicate coated (1 layer) Zr-4 unirradiated specimen after testing in autoclave (288°C; PWR water) – 4 sides

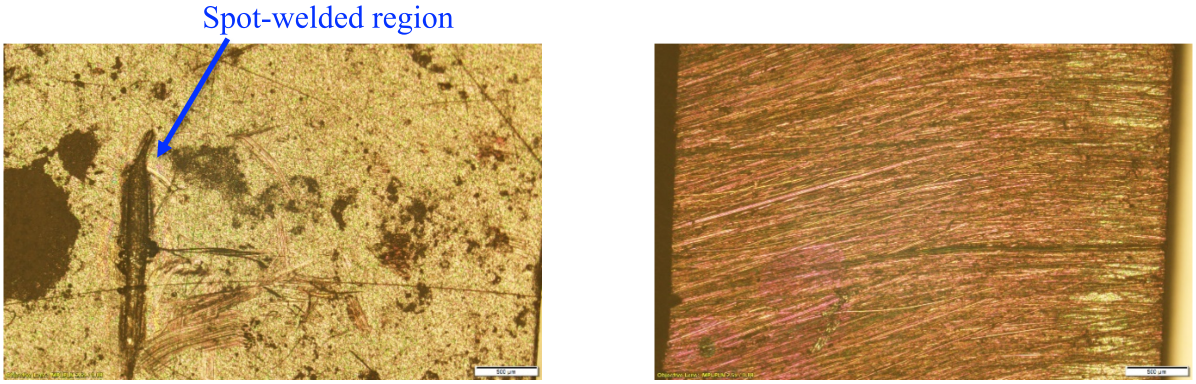

Figure 28: Sodium silicate coated (2 layers) Zr-4 unirradiated specimen after testing in autoclave (288°C; PWR water); LHS: side 1; RHS: side 2

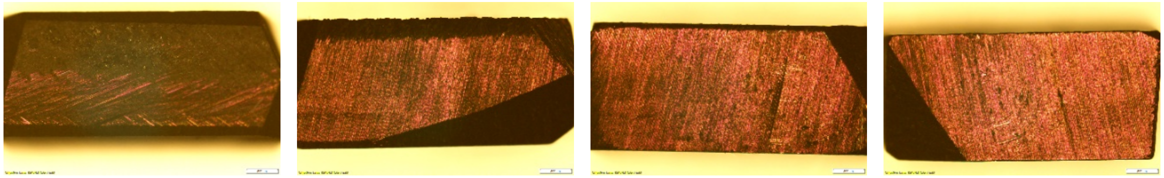

Figure 29: Sodium silicate coated (2 layers) Zr-4 unirradiated specimen after testing in autoclave (288°C; PWR water) – 4 sides

3.2.2.4 Polyimide resin coating

Based upon additional research, polyimide resin (Restek catalog # 20445) coating was selected for a detailed investigation. As per the vendor specification, this resin can be used up to 350°C but did not have any information related to its performance in high temperature water.

In order to evaluate the performance of polyimide resin in autoclave PWR water at 288°C, two unirradiated specimens from Zr-4 plate (E9885; 205187; 4155J; 11540; obtained from EPRI), as shown in Figure 22 and Figure 23 were utilized. One larger side was ground using successively-finer SiC papers to remove any potential oxide layer. A platinum wire was spot-welded on this larger side.

Polyimide coating was then applied to two unirradiated Zr-4 specimens (all sides), as shown in Figure 30. The photographs do not clearly show the application of coating on the specimen due to light reflection. Physical observation showed that the entire specimen was protected by the coating. Coating was also applied to a smaller portion of Pt wire. Certain regions on the specimen showed the presence of a thicker layer (appeared like a bubble) of coating that accumulated after drying.

A multimeter was utilized to verify the application of polyimide coating on two specimens prior to autoclave testing. The multimeter results showed that there was no continuity (i.e., the coating appeared to provide insulation). This conductivity test was performed in the same manner as the previous sodium silicate verification test.

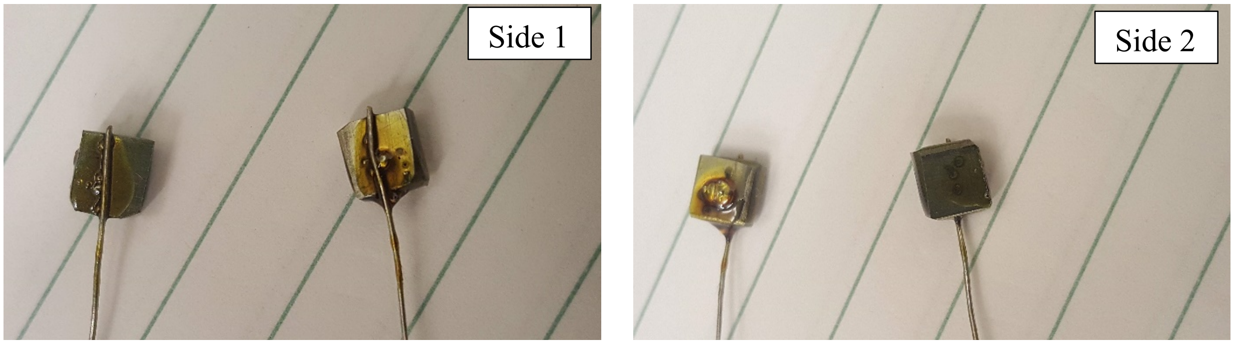

Figure 30: Polyimide resin-coated Zr-4 unirradiated specimens

3.2.2.5 Performance check using Zr-4 specimens and autoclave

In order to evaluate the performance of polyimide resin coating, two coated unirradiated specimens were inserted into Fixture # 1 and then kept inside an autoclave filled with PWR water at room temperature for about 21 hours. The temperature of the autoclave was then increased from 22°C to 288°C. After exposing the coated test specimens to 288°C PWR water for about 5 days, the autoclave was turned off. The coated samples were taken out of the autoclave after about 24 hours.

Optical metallography was not performed to evaluate the coating integrity. Based upon previous work, it was determined that the quality of optical images would not be good since the specimen surface was rough (as expected) due to not being ground or polished.

A resistance check was performed to evaluate the effectiveness of polyimide coating of the specimens after autoclave testing. A fresh sodium chloride (NaCl) solution was prepared and added to a beaker. A multimeter showed that the resistance of this solution was about 30 kΩ. An autoclave-tested specimen with a spot-welded Pt wire was then inserted into the beaker individually. A multimeter was used to measure the resistance between the Pt wire and solution, and it was about around 4.4 MΩ and 2.6 MΩ for polyimide coated specimen #1 and #2, respectively, after autoclave testing. The resistance of the NaCl solution was again measured without any specimens, and it was around 40 kΩ. Thus, the polyimide coating improved the resistance by two orders of magnitude.

3.2.2.6 Performance check using oxidized Zr-2 specimens and autoclave

As per EPRI's request, efforts were made to apply the polyimide coating on specimens obtained from oxidized Zr-2 tubes from Studsvik in November 2019.

One unirradiated oxidized Zircaloy-2 tube (length about 20 mm) that was exposed in an autoclave at 415°C for 90 days (see Figure 31) was utilized for the polyimide coating study. This sample with an oxide layer of about 6 μm was cut at one end after the autoclave exposure, so it has a fresh un-oxidized end surface.

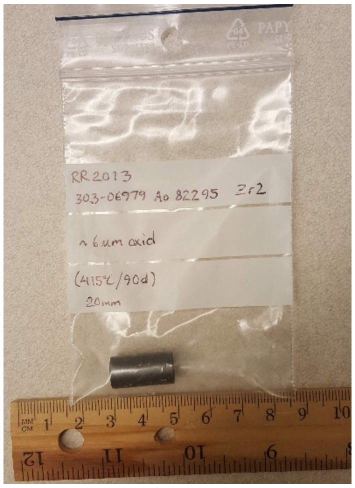

Figure 31: Unirradiated oxidized Zr-2 tube (6 μm oxide layer) utilized for polyimide coating study

Efforts were made to prevent damage of the outer oxide layer during the sectioning operation. Earlier, smaller pieces (as shown in Figure 32) were sectioned using a low speed saw longitudinally along the tube to obtain specimens with a reduced curvature (for ease of handling while testing).

Tweezers were employed to carefully hold small test specimens over the edges, and grinding was performed using SiC paper to remove the inner oxide layer before spot-welding. It was difficult to spot weld Pt wire without potentially damaging the outer oxide layer via weld-bleeding (due to the reduced width). Water rod specimens were difficult to prepare (grind and spot weld) without damaging the exterior oxide layer, compared to fuel channel because of the reduced thickness and width.

Later, efforts were made to section slightly larger specimens (as shown in Figure 33) so that spot welding (using Pt wire) could be performed successfully without affecting the exterior oxide layer. A continuity check was performed to verify proper spot welding. A continuity check was also performed to verify that the outer oxide layer was not damaged during specimen preparation operations, and the results showed no continuity through the oxide.

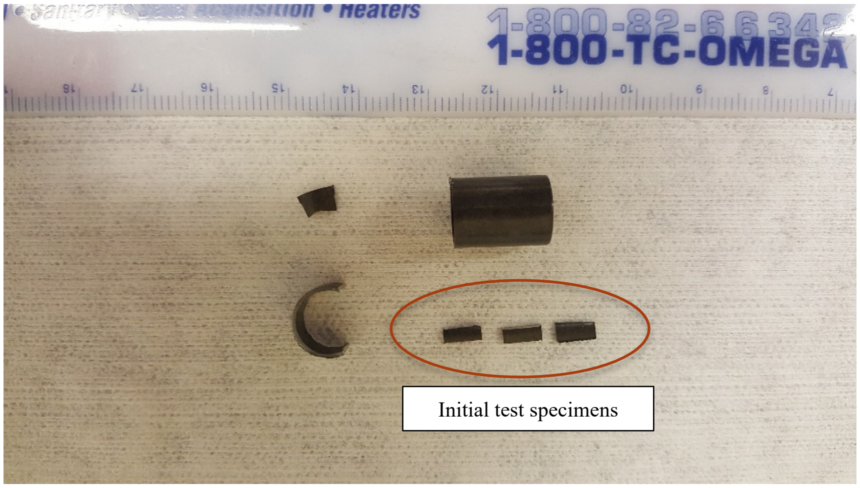

Figure 32: Initial oxidized Zr-2 specimens for polyimide coating study

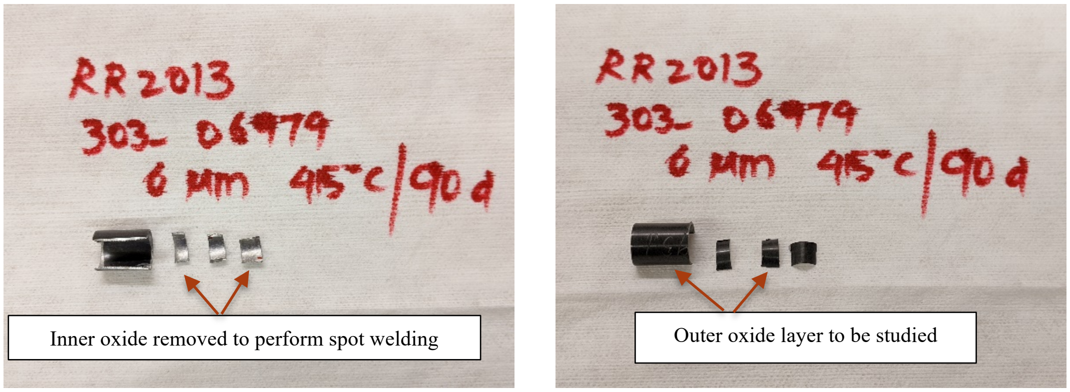

Figure 33: Oxidized Zr-2 specimens for polyimide coating study; Left: Inner side ground for spot welding; Right: Outer oxide layer to be studied

Polyimide coating was applied on the interior side of the test specimen, where the oxide layer was removed to expose the base metal in order to perform spot welding. Coating was also applied on the four cut sides and a small portion of the Pt wire, as shown in Figure 34. Even though the oxide layer to be studied (top side) is supposed to remain uncoated (polyimide), a smaller amount of insulating coating was applied in areas that appeared weak (oxide layer potentially damaged) as shown in Figure 35. The photographs do not clearly show the application of coating on the specimen due to light reflection. Physical observation showed that the specimen was protected by the coating in the intended regions. Certain regions on the specimen showed the presence of a thicker layer (bubble-like appearance) of coating that accumulated after drying. The exposed area was determined using an optical micrograph and comparing with the known dimensions.

Figure 34: Polyimide coated unirradiated oxidized specimen (spot-welded side)

Figure 35: Polyimide coated unirradiated oxidized Zr-2 specimen (oxide side)

3.2.3 Electrochemical Corrosion Specimen Preparation Method # 3

During project meetings with EPRI and their collaborators in Spring 2020, emphasis was placed on designing a new fixture that would provide a gap (for electrolyte) between the oxide layer and a counter electrode. Besides the gap, the objective of identifying a new design is to eliminate the need for an insulating coating to protect cut/exposed surfaces.

Hence, PNNL began a study to design a new fixture that can achieve these two objectives. Once a new fixture design (#3) was identified at PNNL, the drawing/concept (see section 3.4.3) was shared with EPRI and collaborators. After a few interactions, the design was finalized for fabrication. This design required the specimen geometry to be in the form of a circular shape. Hence, a core drill was utilized for preparing test specimens.

One unirradiated oxidized Zircaloy-2 tube (length about 20 mm) that was exposed in an autoclave at 415°C for 90 days (see Figure 31) was utilized for preparing specimens using core drilling, as shown in Figure 36.

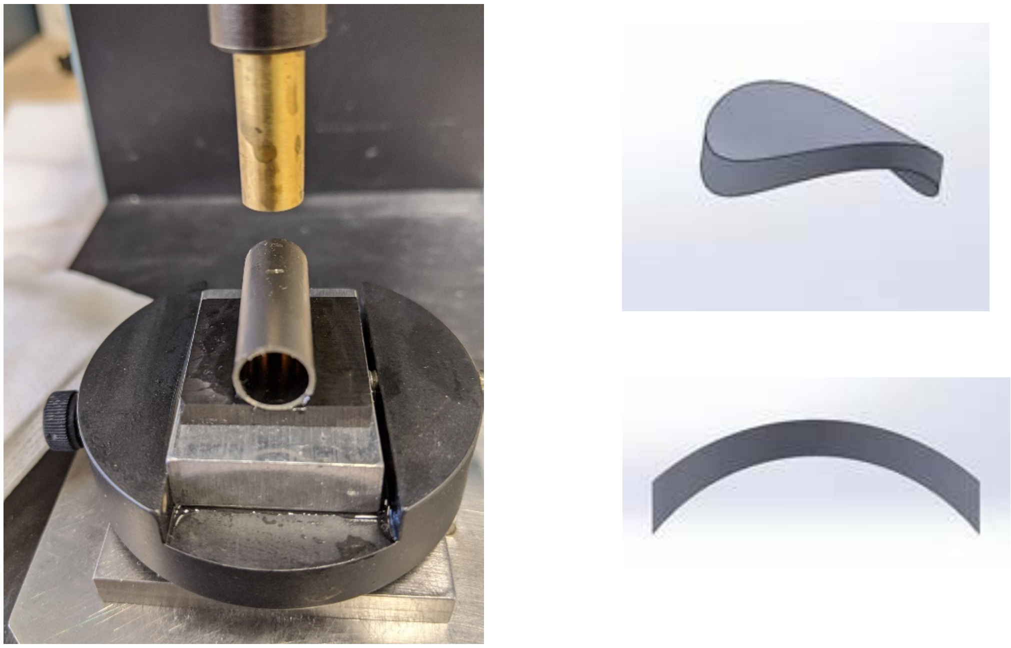

Figure 36: Core-drilled unirradiated oxidized Zr-2 test specimen

3.3 Electrochemical Corrosion Test Fixtures and Designs

3.3.1 PNNL Test Fixture and Design #1

At the beginning of the project, PNNL designed an electrochemical corrosion test fixture designated as Design #1, where a ceramic sample holder was used to hold the test specimen using a spring-loaded alumina tube inside the autoclave. As per this design, two thin Pt wires were spot-welded to a Pt foil as shown in Figure 37. A fine Pt mesh was wrapped over the Pt foil. The objective of this design is to hold the test specimen inside the autoclave in the presence of simulated PWR water in such a way, the oxide layer of the specimen is constantly in contact with the Pt mesh. This Pt mesh serves as a current collector on the oxide side of the specimen. As mentioned earlier, a Pt wire was spot welded inside a radiological hood to the opposite side of the specimen (base metal side) to serve as the working electrode.

The ceramic sample holder as shown in Figure 38 was firmly connected to the Argon inlet line. A ceramic rod of appropriate length was placed at the bottom of sample holder to serve as a base. An alumina tube was inserted into the ceramic sample holder and its top end was connected to a spring. A thin ceramic disc was placed between the spring-loaded alumina tube and ceramic rod, as shown in Figure 39. As per this design, the spring-loaded alumina tube and ceramic disc were moved up

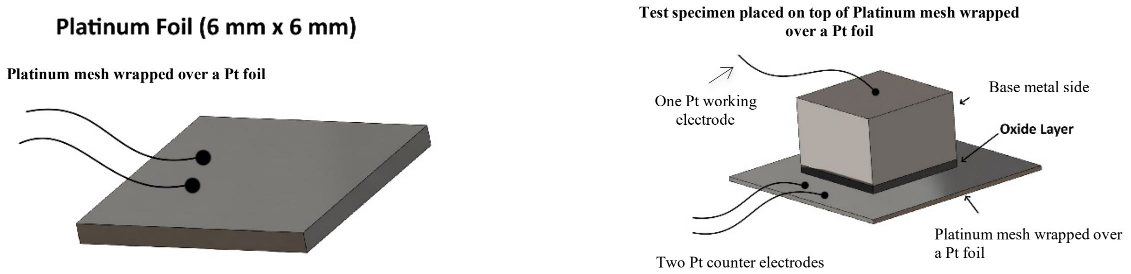

Figure 37: Spot welded working and counter electrodes

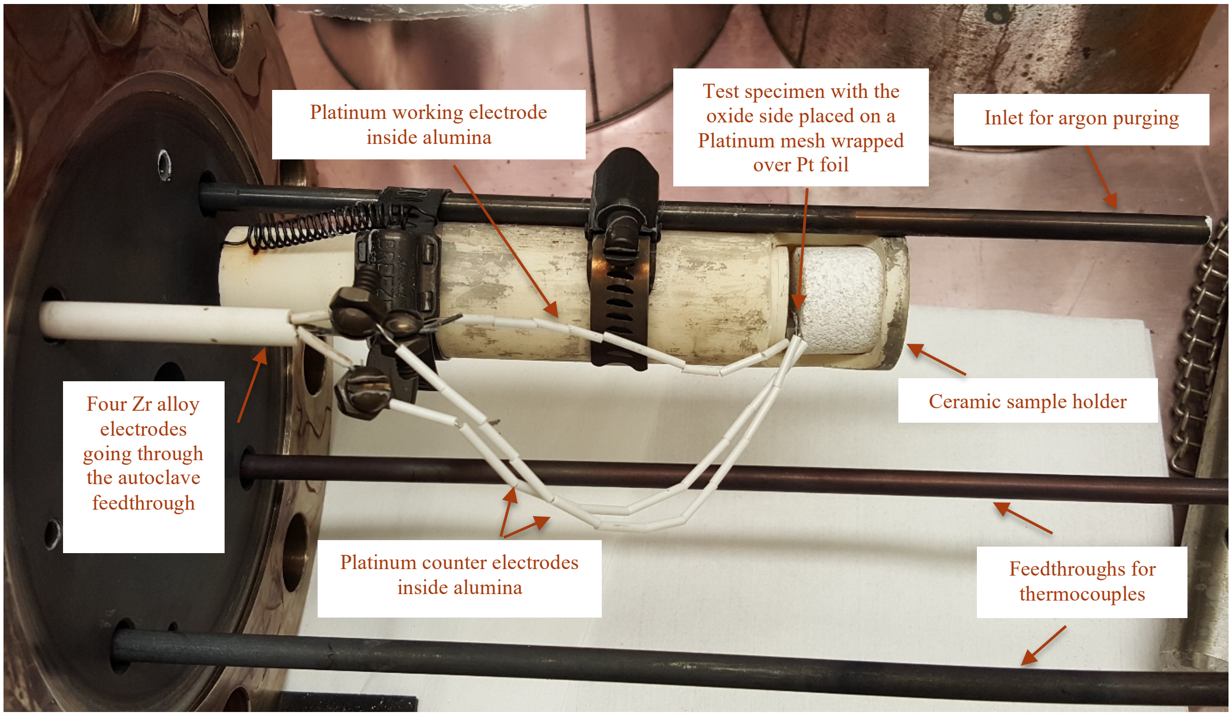

Figure 38: Electrochemical corrosion test fixture design #1

to produce a gap, and the test specimen along with the Pt foil (wrapped with a Pt mesh) was placed between the ceramic disc and rod at the base of sample holder.

After checking the specimen's position on top of the Pt mesh, thin alumina tubes were inserted onto working and counter electrodes (Pt wires) acting to provide insulation. The other ends of the working and counter electrodes (Pt wires) were connected to four thicker Zircaloy wires individually, as shown in Figure 38. These thick Zircaloy wires were placed inside a 4-bore alumina tube and were taken out of the autoclave feedthrough using a gas-tight Swagelok fitting to make sure there was no electrical connection between the wires or to the autoclave body, as shown in Figure 39.

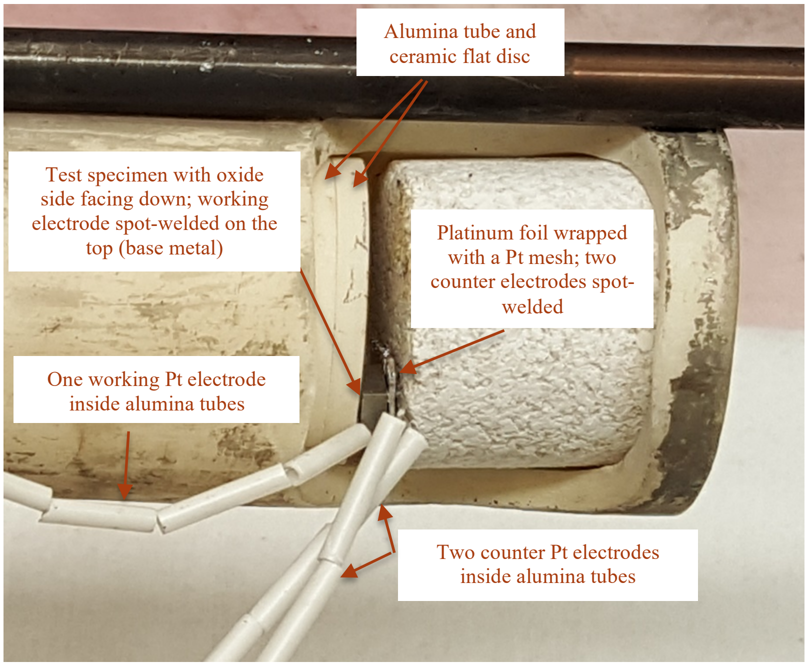

Figure 39: Electrochemical corrosion test specimen inside fixture design #1

A continuity test was performed by holding one lead to the platinum wire spot-welded to the bare base metal and the other lead to platinum wires connected to the platinum foil (wrapped with Pt mesh) holding the test specimen with the oxide side (black or brown color) facing down. If the specimen was sectioned properly without burrs and if the base metal was ground and exposed properly on the other side prior to spot welding, then there would not be any continuity between the bare base metal and the platinum foil (due to the presence of the highly resistive oxide layer).

As per this design (#1), the four leads (working, working sense, counter and counter sense) from the Potentiostat were connected to the four thicker Zircaloy wires at the top of water-cooled autoclave feedthrough. As per this design, the sample holder and thicker Zircaloy wires were used for all tests. The only variable item is the test specimen with spot welded Pt wire on the base metal side. Before each test, a continuity test was periodically performed between the four thick Zircaloy wires going through the water-cooled autoclave feedthrough at both ends (outside the autoclave and inside the lid) to make sure there were no broken wires or cross-connection inside the 4-bore alumina tube.

This setup has an argon inlet for purging the system prior to heating the autoclave to 288ºC, as shown in Figure 40. This setup also has closed-end feedthroughs to insert two thermocouples to monitor autoclave temperature.

This PNNL design (#1) was utilized for performing EIS studies on irradiated fuel channels without employing insulating coatings on specimen exposed surfaces (cut sides and ground side to expose base metal and perform spot welding) in the autoclave at 288ºC using simulated PWR water. A preliminary PNNL NSUF report [17] covering these details was prepared and shared with NSUF and EPRI during March 2019.

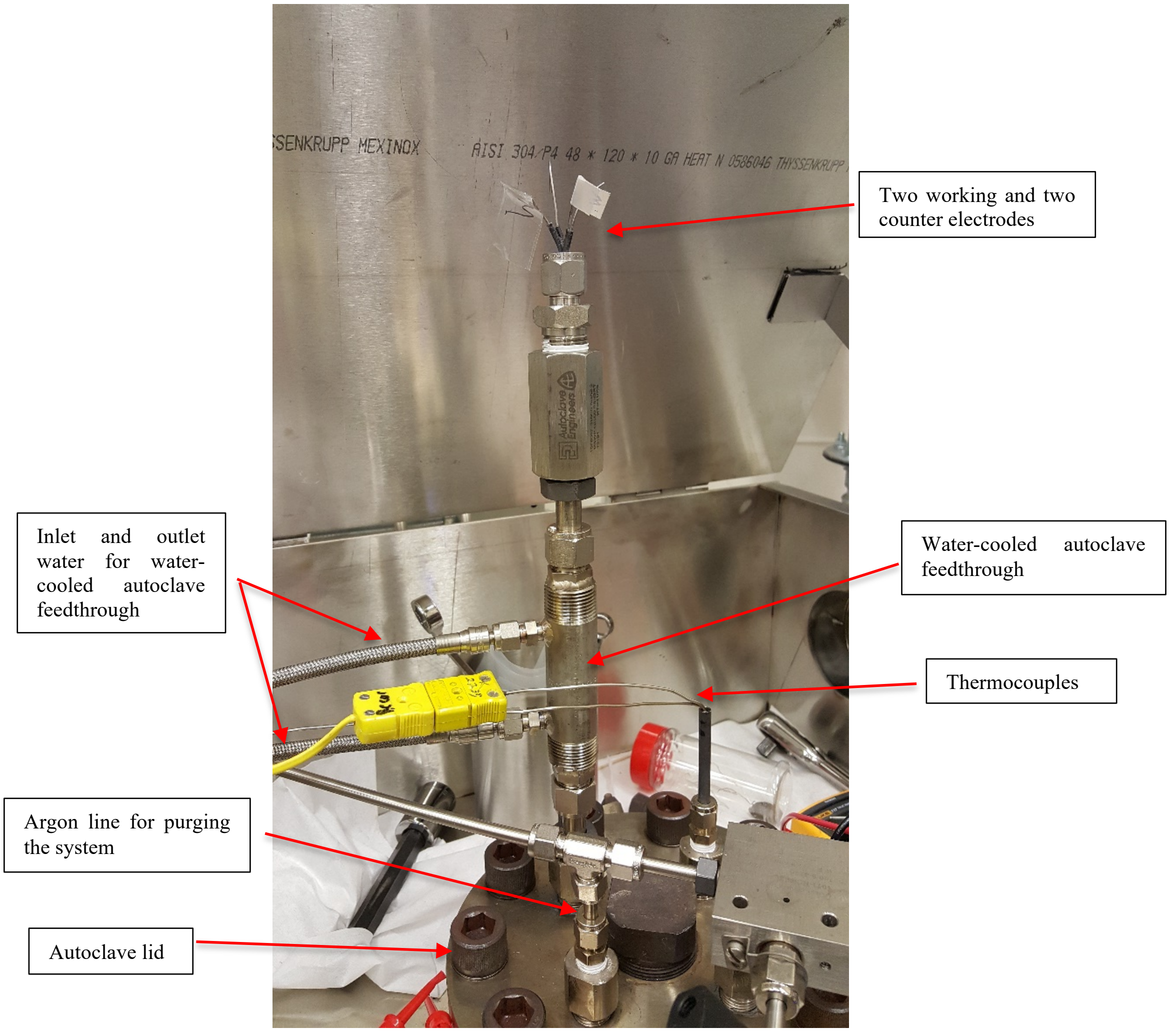

Figure 40: Autoclave setup – Design #1

3.3.2 PNNL Test Fixture and Design #2

During Summer 2019, EPRI discussed the initial irradiated fuel channel test results published in the form of a PNNL NSUF report [17] with PNNL and its external collaborators. One of the items discussed during the meetings was protecting the exposed/cut surfaces of test specimens (except the oxide layer) to reduce the active surface and improve the EIS data quality. Various types of insulating materials that could be utilized for this study without affecting the test specimen and oxide layer were evaluated. However, none was identified as a promising insulating coating to be utilized in the autoclave at 288ºC (~1100 psi).

Hence, PNNL conducted a study (see section 3.2) to identify appropriate insulating coating to protect all exposed/cut sides of test specimen (except the oxide layer). Polyimide coating was found to be most promising based upon initial screening.

PNNL's Design #2 involved the application of Polyimide coating and using the same fixture as described in section 5.1. In order to verify its performance and test the quality of EIS data, unirradiated, oxidized Zr-2 tubes obtained from Studsvik (during November 2019) were selected to apply the polyimide insulating coating and were tested in the autoclave using PWR water at 288ºC (~1100 psi).

3.3.3 PNNL Test Fixture and Design #3

During project meetings with EPRI and their collaborators in Spring 2020, emphasis was placed on designing a new fixture that would provide a gap (for electrolyte) between the oxide layer and the counter electrode. Besides the gap, the objective of identifying a new design was to eliminate the utilization of insulating coating to protect cut/exposed surfaces.

Hence, PNNL began an effort to design a new fixture to achieve these two objectives. Once a new design (#3) was identified at PNNL, the concept was shared with EPRI and their collaborators. After a few project meetings, the design was finalized for fabrication. PNNL began ordering parts in March 2020. However, fixture fabrication was delayed due to the COVID-19 shutdown.

The cutaway illustration of the EIS test fixture and design #3 is shown in Figure 41. The materials utilized in this design are stainless steel, Rulon, Teflon, porous alumina and platinum wire. The cutaway illustration of specimen and holder is shown in Figure 42. This figure clearly shows the gap (for the liquid electrolyte) between the platinum mesh and oxide layer of the specimen. Deionized water is used as a nonconductive, incompressible filler in order to equalize pressure on both sides of the specimen. This is done to minimize any deflection of the specimen and prevent damage to the oxide layer.

Figure 43 shows the setup to fix the distance between the specimen and platinum mesh. As shown in the figure, a conical wedge forces the Rulon into the cut face of the sample, thereby sealing the cut edges. Porous alumina allows liquid electrolyte free access to the platinum mesh electrode. Porous alumina also holds the platinum mesh at a fixed distance from the oxide surface.

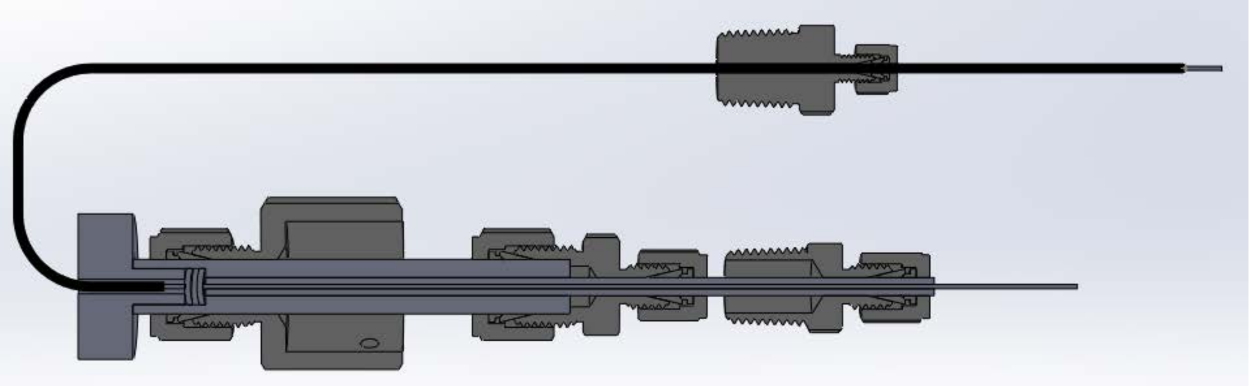

Figure 41: Cutaway illustration of EIS test fixture and design #3

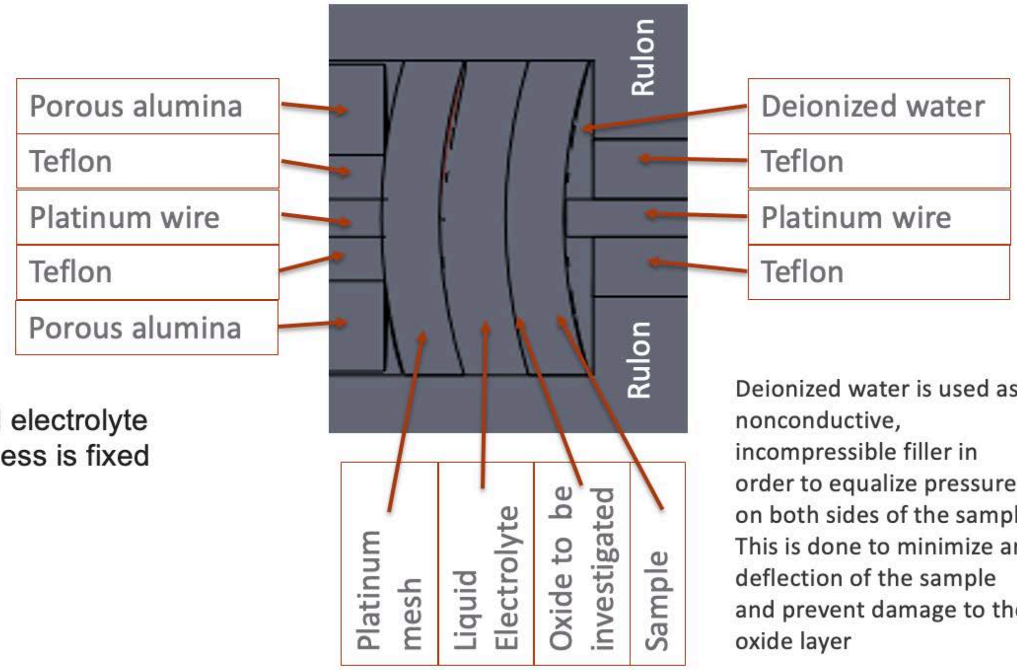

- Liquid electrolyte thickness is fixed

Deionized water is used as a nonconductive, incompressible filler in order to equalize pressure on both sides of the sample. This is done to minimize any deflection of the sample and prevent damage to the oxide layer

Figure 42: Cutaway illustration of sample and holder arrangement

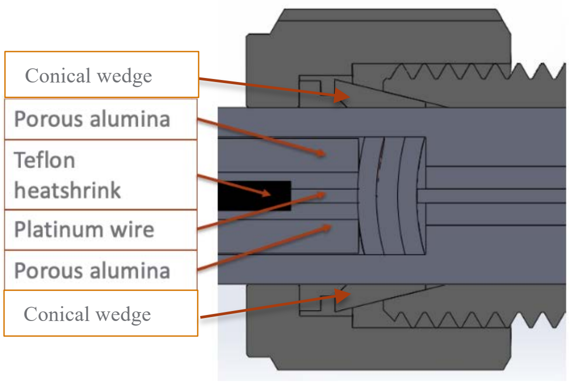

Figure 43: Setup to fix the distance between the Pt mesh electrode and sample

The platinum mesh is held against the surface of the porous alumina and the springs hold the porous alumina against the Rulon sample holder, thus it is held in place, as shown in Figure 44. A Swagelok reducing union (3/8"X1/8") is used to seal and prevent electrolyte from "shorting" the cell, as shown in Figure 45. Swagelok fittings are used to seal the leads at the autoclave lid, as seen in Figure 46.

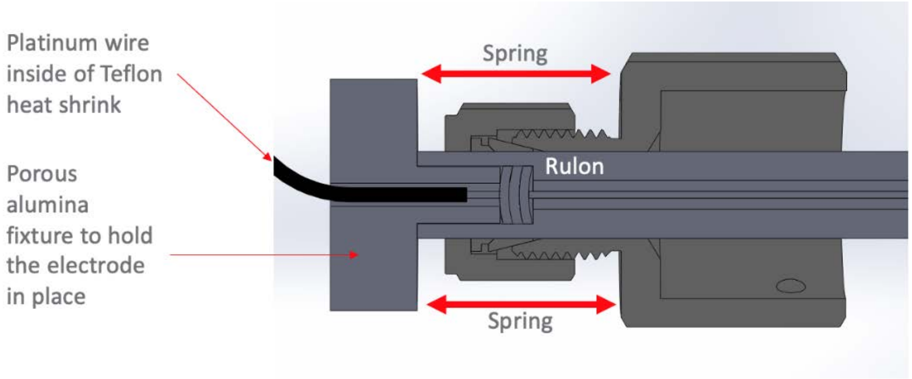

Figure 44: Springs hold the porous alumina against the Rulon sample holder

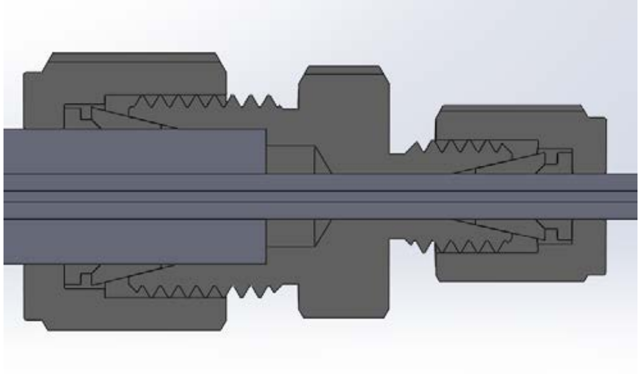

Figure 45: Sealing the Rulon sample holder to the 1/8 Teflon tubing

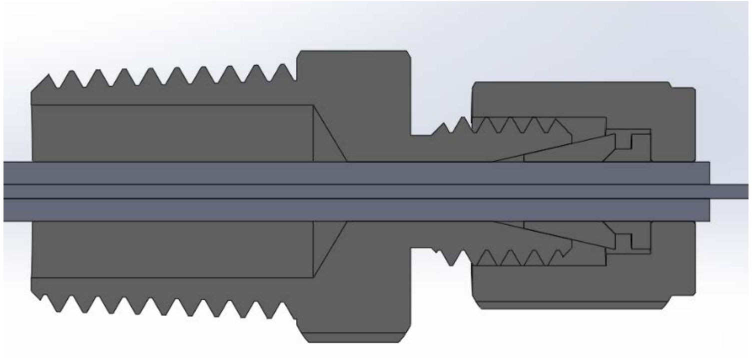

Figure 46: Swagelok fittings to seal the leads at the autoclave lid

The photographs of the fabricated test fixture and design (#3) is shown in Figure 47. The new design was electrically and pneumatically tested at room temperature and 125 psi pressure, using reverse osmosis (RO) and tap water. The fixture was sealed in a smaller Parr reactor. When filled with RO water (18MΩ), the resistance between the two wires was infinite when checked with a multimeter. However, when filled with tap water, the resistance between the two wires was stable and in the KΩ range.

Figure 47: Photograph of EIS test fixture and design #3

Efforts were made to modify the non-radioactive autoclave in order to accommodate this new design (#3). The new fixture was tested inside the autoclave at 288ºC (~1100 psi) using an unirradiated oxidized Zr-2 specimen obtained by core drilling (see section 3.3) to evaluate its performance and obtained EIS data to compare with other results.

3.3.4 PNNL Test Fixture and Design #4

During a Fall 2021 meeting with NSUF and EPRI, a decision was made to step back and perform only room temperature measurements on both irradiated fuel channel and water rod samples and wrap up this project. Previously, irradiated fuel channel samples were tested up to 288ºC (~1100 psi).

As per this new test fixture design #4, the sample was sectioned using a low-speed saw. A platinum wire was spot welded to the cut surface (see Figure 48 and 49). Irradiated water rod samples were not available in the shape of rods. They were available only as strips. Unirradiated water rods were available and small sections of water rods were obtained for trial testing. The back, and the cut edges were sealed in epoxy. The exposed wire was fed through the polymer tubing and this tubing was embedded into the epoxy before it cured. The sample was suspended into the simulated PWR water in a vertical manner. A cylinder of platinum gauze was utilized as the counter electrode (Figure 50). The counter electrode was inserted into a beaker that was filled with simulated PWR water and the sample was suspended within the counter electrode assembly (Figure 51). Figure 48 illustrates how the two different electrodes were configured. This was very similar to the configuration of the polyimide-coated (except the oxide side) samples shown earlier (Design #2).

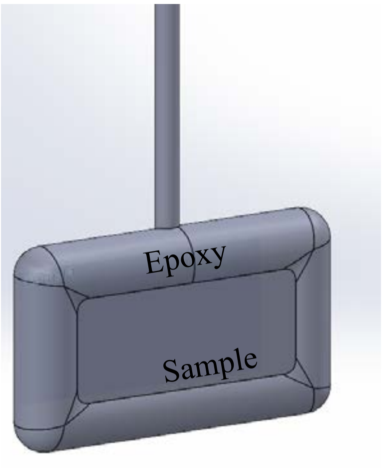

Figure 48: Irradiated specimen configuration

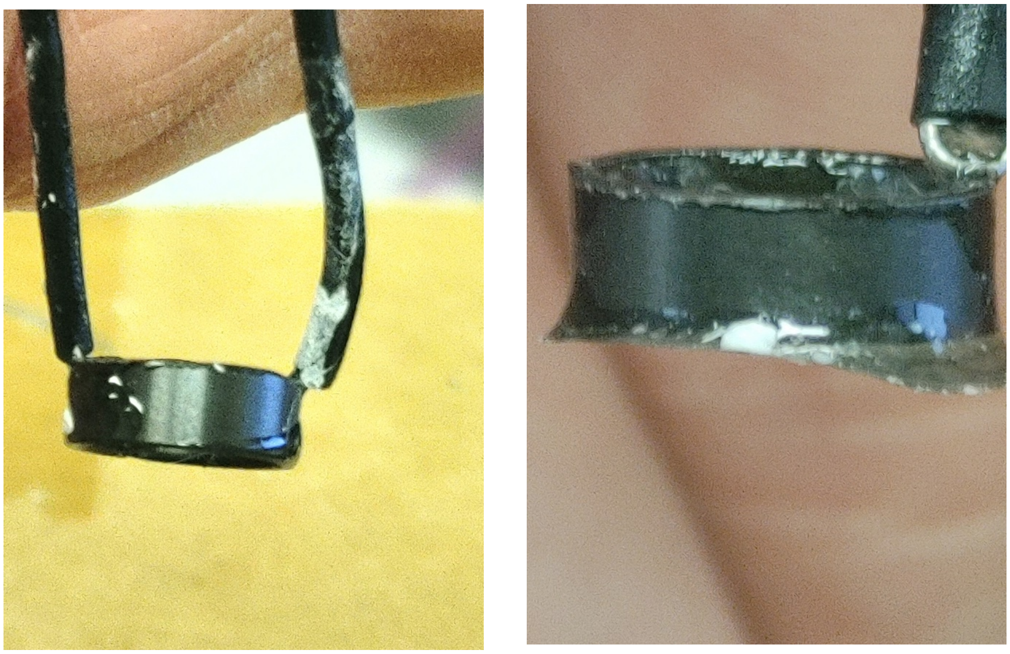

Figure 49: Unirradiated water rod specimen configuration

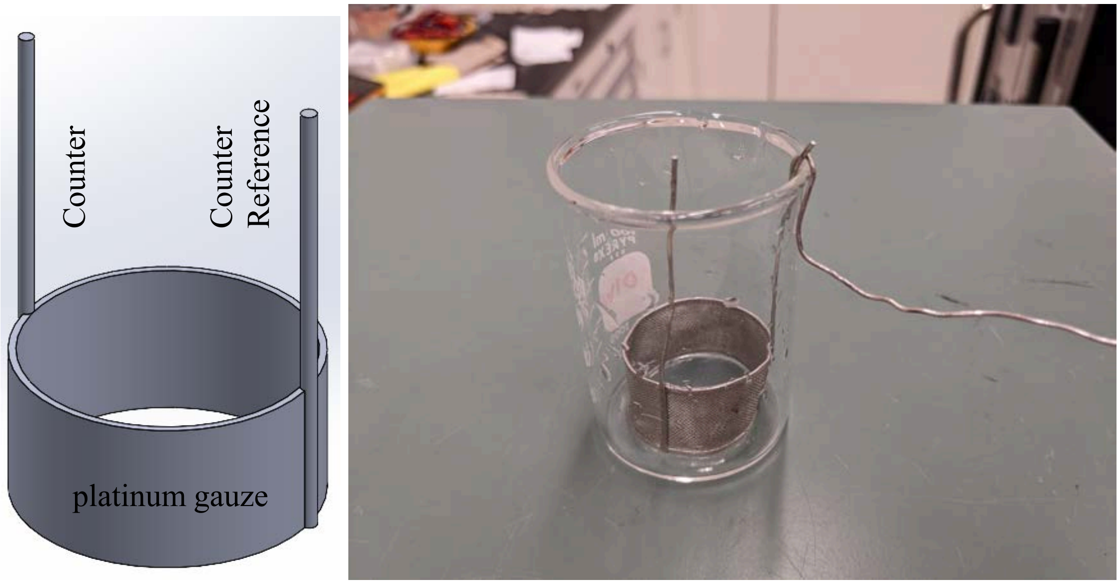

Figure 50: Counter and counter reference configuration

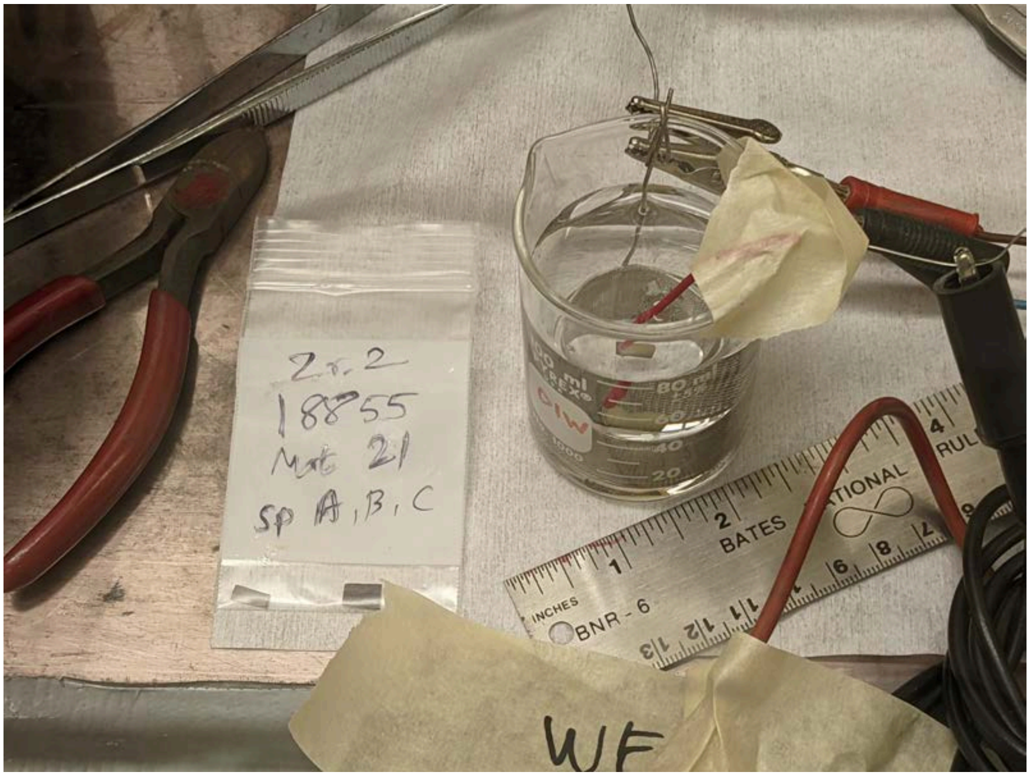

Figure 51: PNNL fixture design #4 for a wet chemistry measurement of the oxide resistance.

3.4 Electrochemical Corrosion Testing of Samples

An autoclave (Figure 52) was employed to perform electrochemical testing at different temperatures (22°C to 288°C). Simulated PWR water (conductivity: 20.8 µS/cm; pH: 6.6-6.7; B^{3+}: 1000 ppm; Li^{+}: 2.000 ppm), a solution of ultrapure water, boric acid, and lithium hydroxide was utilized for this study. The autoclave was filled with 1-gallon of test solution prior to testing.

Figure 52: Electrochemical test setup with an autoclave

Electrochemical testing was performed by utilizing a Solartron Analytical 1287A Potentiostat/Galvanostat and a Solartron 1260A Impedance/Gain-Phase Analyzer. A four-electrode (working, working reference, counter and counter reference) setup was employed for this study. The Solartron provides the high accuracy, wide bandwidth measurement capability that can measure a range of both AC and DC test capabilities used in this work. Two high resolution digital voltmeters provide the necessary simultaneous voltage and current measurements with high accuracy, stability and linearity throughout the entire range of the instrument. The measurement resolution and accuracy are in the 1µV range for the reference electrodes and 1pA for the working electrode.

A Solartron 1260A Impedance/Gain-Phase Analyzer was matched with the Potentiostat/Galvanostat, providing a high frequency range spanning from 10 µHz to 32 MHz with 0.015 ppm resolution. It has an accuracy of 0.1% and 0.1°, and a resolution of 0.001 dB and 0.01°. This unit uses single-sine correlation techniques to remove the noise and harmonic distortion and can measure impedances >100 MΩ.

In order to perform the EIS testing, the platinum wires spot-welded to the bare base metal (top) and platinum foil (wrapped with Pt mesh) touching the thicker oxide layer (bottom) were connected to Zr alloy working and counter electrodes, respectively, present in the autoclave feedthrough (see Figure 37-Figure 40). A continuity test was again performed on these electrodes to ensure that there was no electrical connection between the working and counter electrodes, and autoclave body.

The autoclave lid with specimen fixture was then taken from the radiological hood and placed inside the radiological autoclave. The autoclave was filled with 1-gallon of simulated PWR water prior to testing to ensure that the test specimen was completely immersed inside the test solution. A continuity test was again performed prior to tightening the autoclave bolts using a torque-wrench with appropriate settings.

The autoclave has an inlet and outlet for purging with argon (see Figure 40). Prior to electrochemical testing, the system was purged with argon for at least an hour. The autoclave also has two feedthroughs for inserting two thermocouples. The autoclave system has a temperature controller, over-temperature shut-off safety feature, pressure gauge and over-pressure regulator to ensure proper operation during heating.

A four-electrode (working, working reference, counter and counter reference) setup was employed for this study. The cables from the Solartron 1287/1260 system were connected to the four wires coming out of the autoclave (see Figure 40). A commercial "dummy cell" with a known set of resistors was periodically used to ensure proper functioning of the electrochemical test system.

Efforts were made to measure the in-situ electrochemical impedance spectra to document the EIS behavior of the existing oxide film on the test specimen formed during exposure inside the reactor. EIS tests (DC potential: 0 V) were performed at various temperatures (22°C, 100°C, 150°C, 200°C, 250°C and 288°C) by applying 100 mV AC amplitude. A few tests were also performed using a 20 mV AC amplitude, but this showed considerable noise and was abandoned in favor of 100 mV. ZPlot and ZView software was utilized for running and displaying EIS test results. EIS tests were performed over a large frequency range (10^7 to 10^{-5} Hz; Logarithmic; Points/Decade: 10).

Following EIS measurements, all EIS spectra were interpreted in terms of equivalent electrical circuits, comprising linear elements of resistance, capacitance, and inductance. The goal is to determine the oxide resistivity, kinetic effects at the interfaces, interfacial reactions, for comparison to the hydrogen pickup data for tested materials. The correlation between experimental impedance data, simulated (fitted) data and hydrogen pickup data is expected to assist in elucidating the hydrogen pickup mechanism.

Besides EIS testing, DC tests were also performed on test specimens. CorrWare and CorrView software was utilized for running (vertex potentials: -50 and +50 mV; -100 and +100 mV; scan rate: 5 mV/second) and displaying cyclic voltammogram test results.

4.0 Results

4.1 Electrochemical Corrosion Testing using Design #1 (without Insulating Coating)

Typical EIS and I-V data collected from the archive (unirradiated) oxidized Zircaloy-2 specimen are given in Figure 53 and Figure 54. It is seen that two distinct electrochemical techniques are in good agreement and the resistance value determined using both techniques was around 3000 Ω. This indicates the validity of the chosen approach. A summary of electrochemical tests performed with irradiated specimens (fuel channels) is presented in Table 3

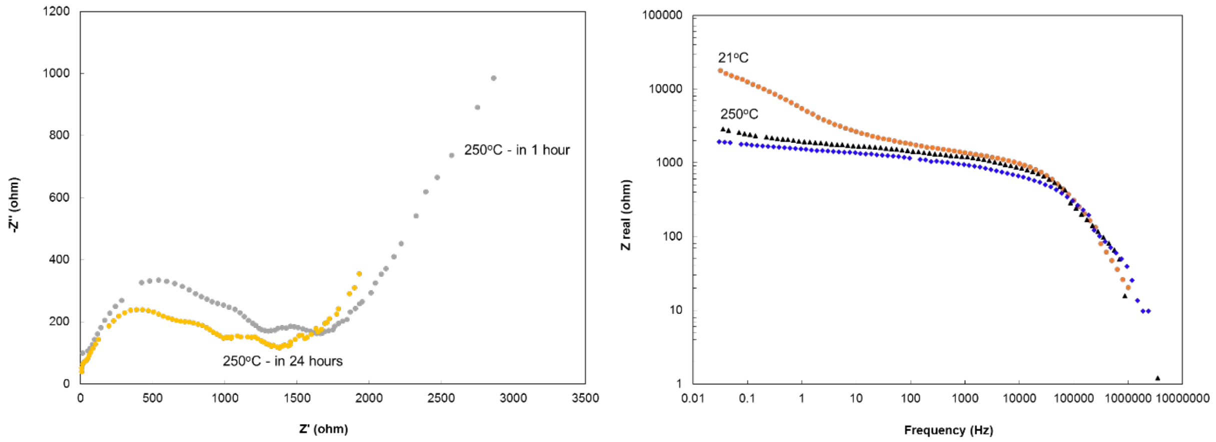

Figure 53: EIS spectra (Nyquist and Bode plots) obtained from the unirradiated Zr-2 archive sample in DI water (not corrected for sample size).

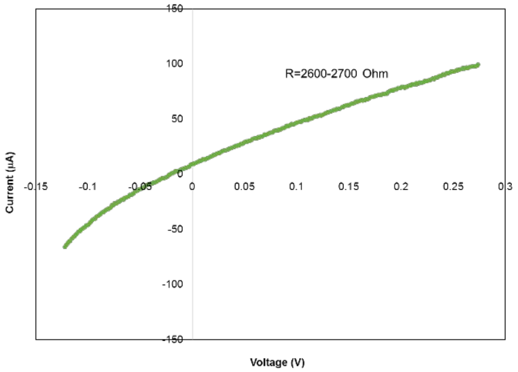

Figure 54: Current-voltage characteristics of the unirradiated Zr-2 archive sample collected in DI water (not corrected for sample size).

Table 3: Electrochemical test (irradiated fuel channel specimens) description

Sample	*Area*	*EIS*	*Frequency Range*	*Temperature*	*Comments*
22A 1-1 Material #16-1	0.178 cm^2	EIS	10^{-3}-10^{6} Hz	100ºC	Completed
		EIS	10^{-3}-10^{6} Hz	150ºC	Completed
		EIS	10^{-3}-10^{6} Hz	200ºC	Completed
		EIS	10^{-3}-10^{6} Hz	250ºC	Completed
		EIS	10^{-4}-10^{6} Hz	288ºC	Completed
22A 1-3 Material #16-1	0.112 cm^2	EIS	10^{-3}-10^{6} Hz	100ºC	Completed
		EIS	10^{-3}-10^{6} Hz	150ºC	Completed
		EIS	10^{-3}-10^{6} Hz	200ºC	Completed
		EIS	10^{-3}-10^{6} Hz	250ºC	Completed
		EIS	10^{-4}-10^{6} Hz	288ºC	Completed
22C-1 Material #16	0.145 cm^2	EIS	10^{-3}-10^{6} Hz	100ºC	Completed
		DC	N/A	100ºC	Completed
		EIS	10^{-3}-10^{6} Hz	150ºC	Completed
		DC	N/A	150ºC	Completed
		EIS	10^{-3}-10^{6} Hz	200ºC	Completed
		DC	N/A	200ºC	Completed
		EIS	10^{-3}-10^{6} Hz	250ºC	Completed
		DC	N/A	250ºC	Completed
		EIS	10^{-5}-10^{6} Hz	288ºC	Incomplete test. The autoclave was turned off at 10^{-4} Hz due to a power spike.
		DC	N/A	288ºC	To be collected
12C-1 Material #12	0.070 cm^2	EIS	10^{-3}-10^{6} Hz	100ºC	Completed
		DC	N/A	100ºC	Completed
		EIS	10^{-3}-10^{6} Hz	150ºC	Completed
		DC	N/A	150ºC	Completed
		EIS	10^{-3}-10^{6} Hz	200ºC	Completed
		DC	N/A	200ºC	Completed
		EIS	10^{-3}-10^{6} Hz	250ºC	Completed
		DC	N/A	250ºC	Completed
		EIS	10^{-5}-10^{6} Hz	288ºC	Completed
		DC	N/A	288ºC	Completed

EIS data obtained from the 22A-1-1 specimen (Material 16-1) at room temperature in air and simulated PWR water are given in Figure 55. EIS data obtained at 90-288ºC are given in Figure 56 and Figure 56. At least two processes could be separated by EIS. A low frequency process with the summit at ~0.0002 Hz and a mid-frequency process with a summit at 5 Hz could be clearly observed. In addition, at very high frequencies the electrolyte resistance could be separated.

An equivalent circuit analysis was performed using several different circuits, a Rs(R1Q1), Rs(R1(R2Q2)Q1), Rs(R1Q1)(R2Q2), and Rs(R1Q1)(R2Q2)(R3Q3), where Rs is the ohmic resistance of the electrolyte, (RQ) is a circuit consisting of a resistance and a constant phase element, the annotations 1, 2 and 3 indicate a time constant increase. No good fit was achieved for any of the models. The first two equivalent circuits were effectively used in literature [17] and attributed to the either one-layered or two-layered oxide films, Figure 58.

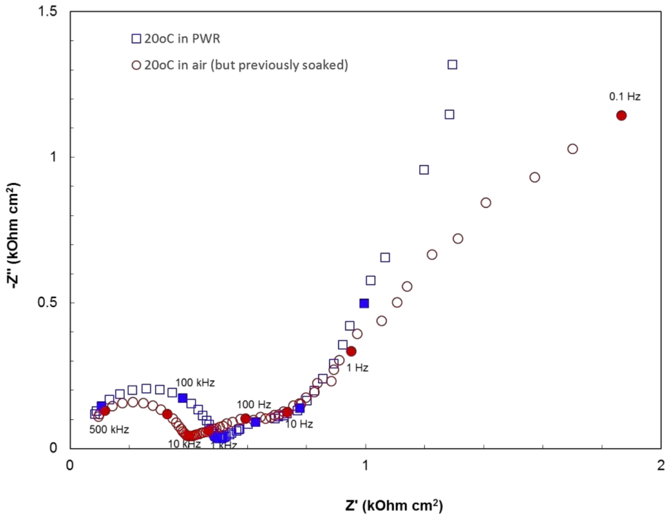

Figure 55: EIS spectra collected from 22A-1-1 (Material 16-1) in air and in simulated PWR water.

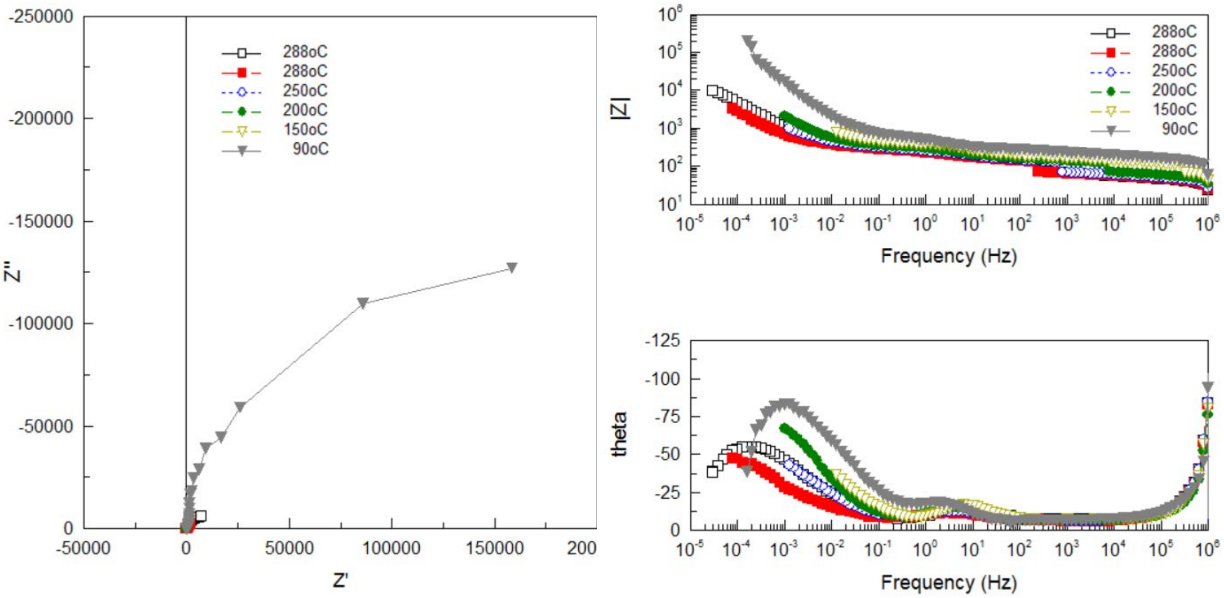

Figure 56: EIS spectra collected from 22A-1-1 (Material 16-1) in simulated PWR water at 90-288ºC. Z' and Z'' are area specific and are expressed in Ohm·cm^2

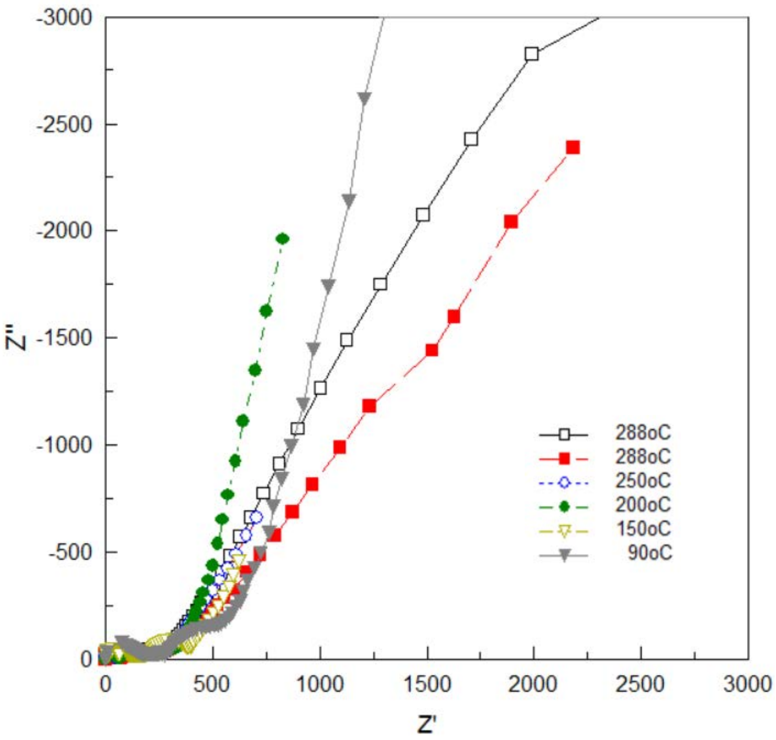

Figure 57: Zoomed in Nyquist plot of the impedance spectra collected from 22A-1-1 (Material 16-1) in simulated PWR water at 90-288ºC. Z' and Z'' are area specific and are expressed in Ohm·cm^2

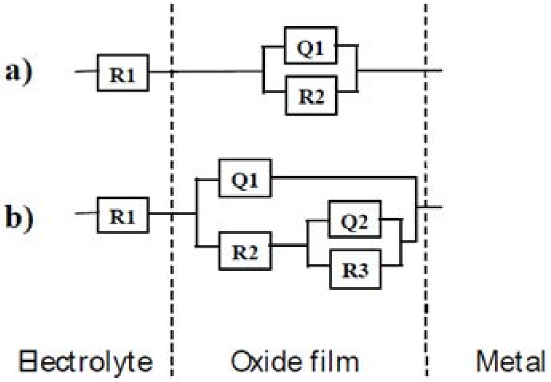

Figure 58: Equivalent circuit of a (a) one-layered oxide film and (b) two-layered oxide film in high conductivity electrolyte (S. Forsberg, et al., 2004)[22].

EIS data obtained from the 22A-1-3 (Material 16-1) specimen after heating it in the autoclave to 288ºC in simulated PWR water and repeated 3 days later are given in Figure 59. A low frequency process with the summit at ~0.0001 Hz and a mid-frequency process with a summit at 1000 Hz were observed. Other impedance spectra obtained at 100-288ºC are shown in Figures 57-59. It is seen that the mid-frequency process summit shifted to a higher frequency and the corresponding resistance (size of the arc) decreased with temperature (Figures Figure 60-Figure 61). The low frequency process summit shifted to a lower frequency with the temperature increase, Figure 61. It should be noted that after the sample reached 250ºC, there was a power failure and the autoclave was cooled down. After restarting the test and heating back to 250ºC and subsequently to 288ºC, changes in the impedance spectra (increase in resistances) and the shifts in the summit frequencies was observed, Figure 62.

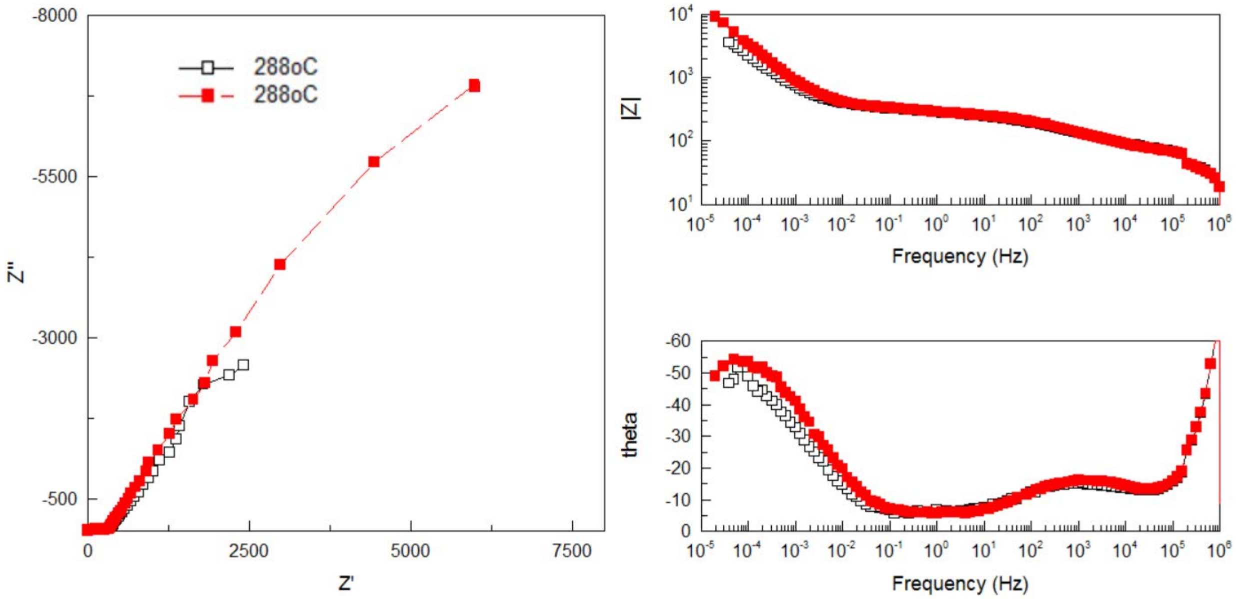

Figure 59: EIS spectra collected from 22A-1-3 (Material 16-1) in simulated PWR water after heating to 288ºC (black) and then again 3 days later (red). Z’ and Z’’ are area specific and are expressed in Ohm·cm^2.

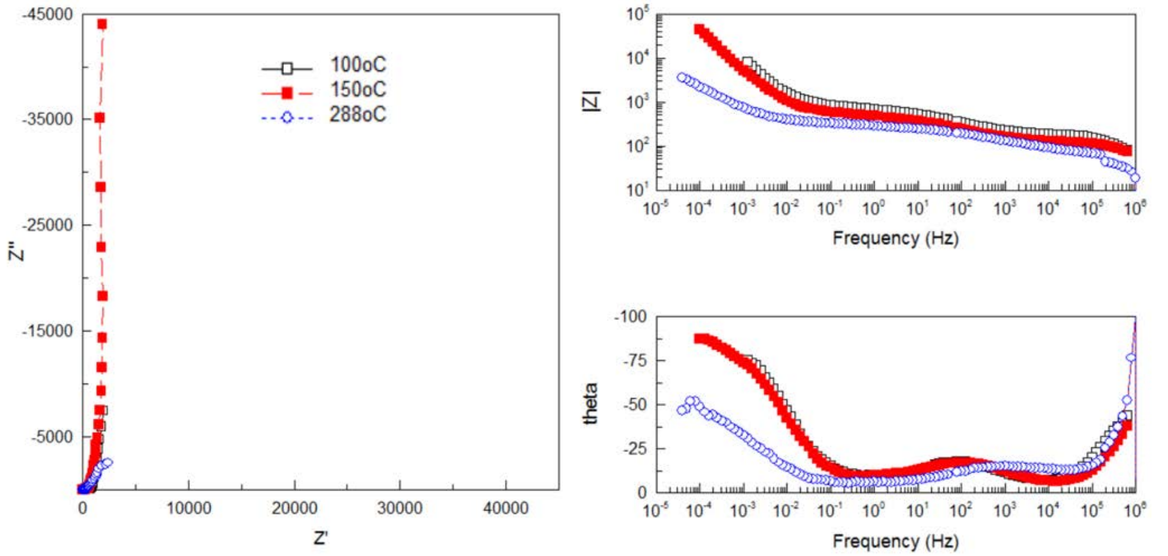

Figure 60: EIS spectra collected from 22A-1-3 (Material 16-1) in simulated PWR water at 100, 150 and 288ºC. Z’ and Z’’ are area specific and are expressed in Ohm·cm^2.

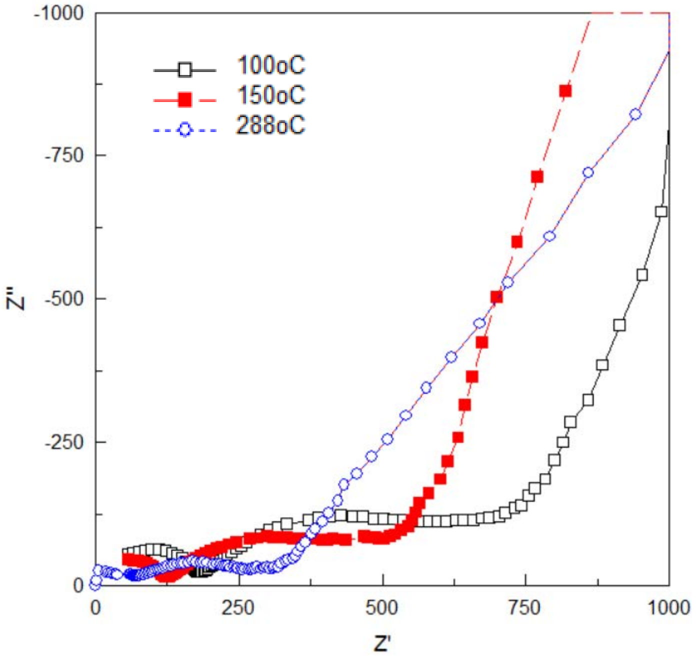

Figure 61: Zoomed in EIS spectra collected from 22A-1-3 (Material 16-1) in simulated PWR water at 100, 150 and 288ºC. Z’ and Z’’ are area specific and are expressed in Ohm·cm^2.

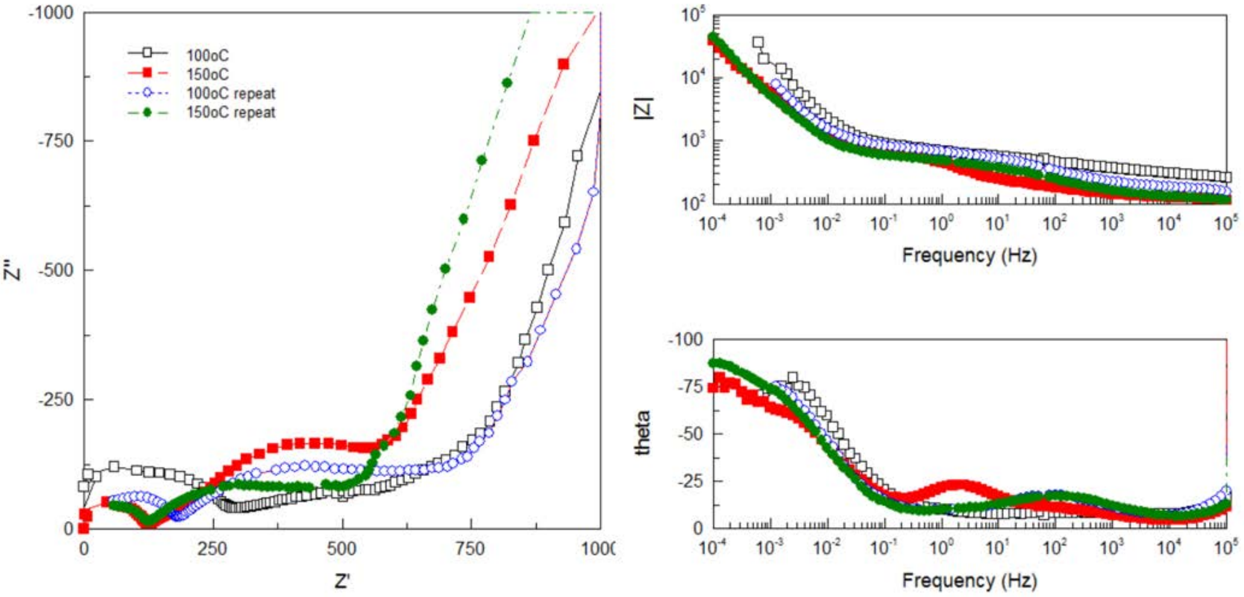

Figure 62: EIS spectra collected from 22A-1-3 (Material 16-1) in simulated PWR water at 100 and 150ºC after restarting the autoclave. Z’ and Z’’ are area specific and are expressed in Ohm·cm^2.

EIS data obtained from the 22C-1 specimen (Material 16) after heating it the autoclave to 288ºC in simulated PWR water are given in Figures Figure 63-Figure 64. As in previously collected impedance spectra from the 22A specimen (Material 16-1), at least two separate processes are observed. The mid-frequency process is very suppressed, with a summit at 250 Hz, and its contribution is not as significant as the one for 22A. The low frequency process with the summit at ~0.0001 Hz dominates at all temperatures measured.

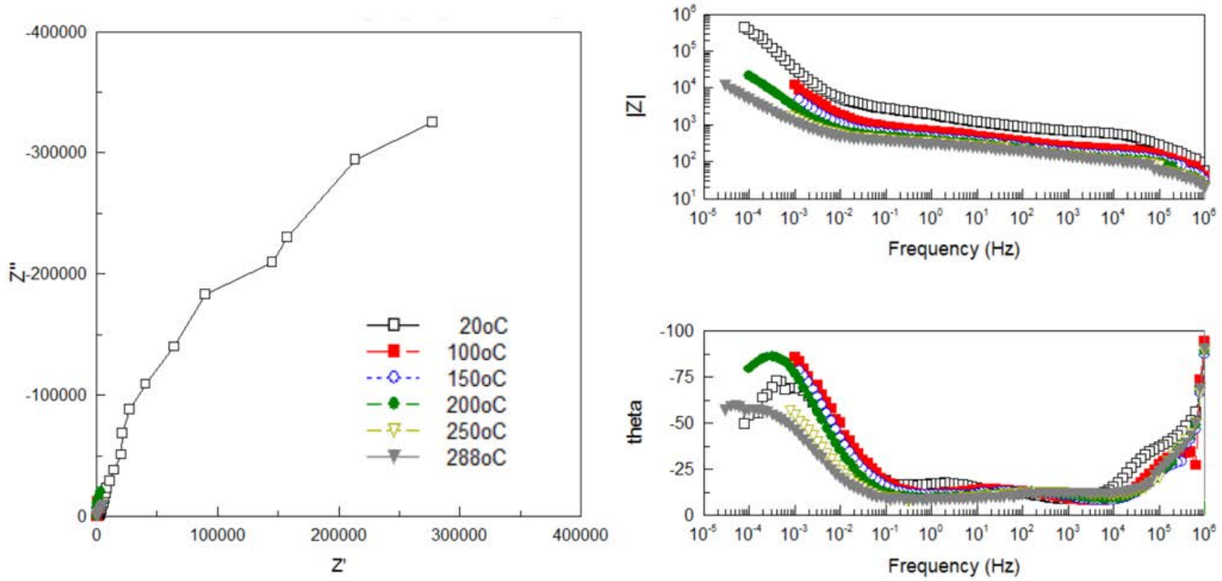

Figure 63: EIS spectra collected from 22C-1 (Material 16) in simulated PWR water at 20-288ºC. Z’ and Z’’ are area specific and are expressed in Ohm·cm^2.

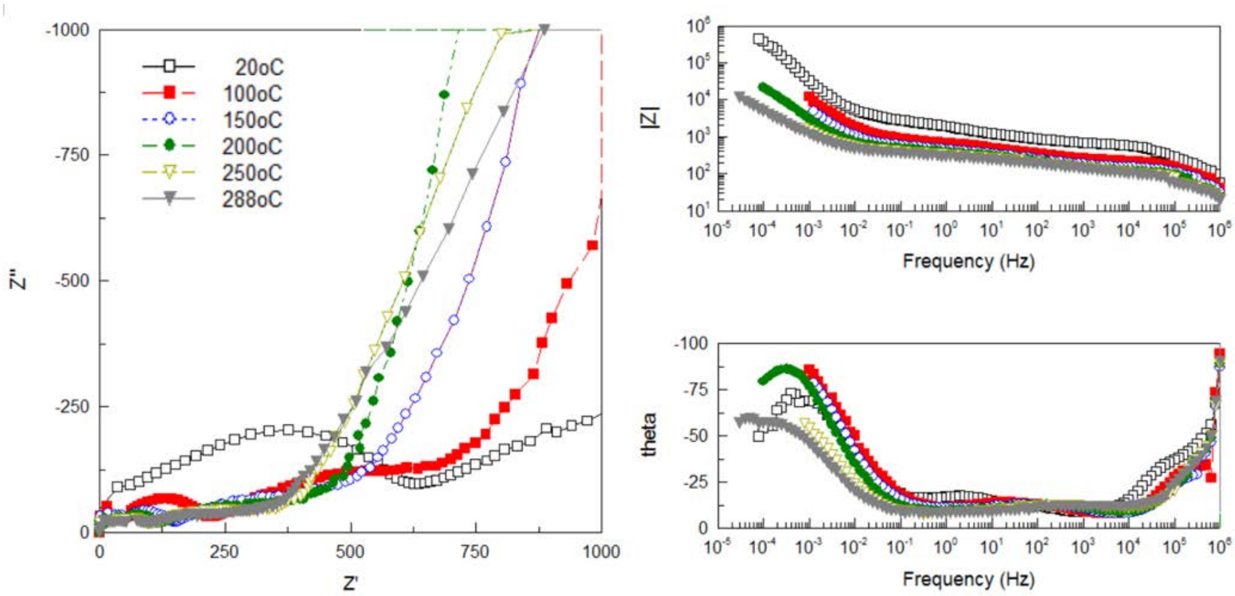

Figure 64: Zoomed in EIS spectra collected from 22C-1 (Material 16) in simulated PWR water at 20-288ºC. Z’ and Z’’ are area specific and are expressed in Ohm·cm^2.

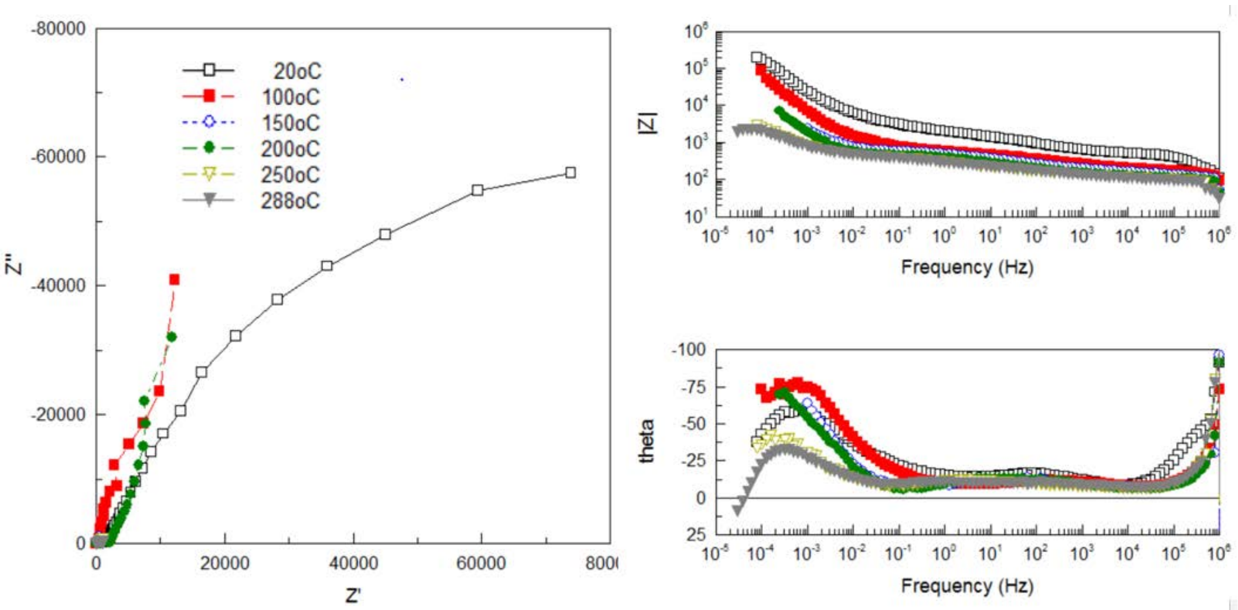

Figure 65: EIS spectra collected from 12C-1 (Material 12) in simulated PWR water at 20-288ºC. Z’ and Z’’ are area specific and are expressed in Ohm·cm^2.

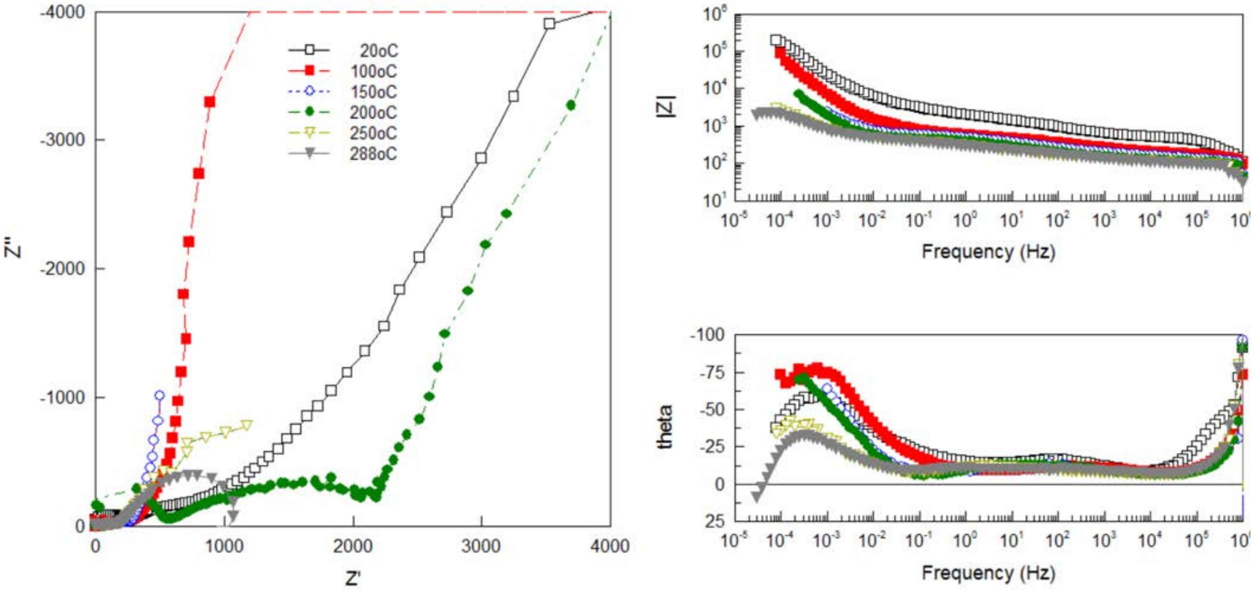

Figure 66: Zoomed in EIS spectra collected from 12C-1 (Material 12) in simulated PWR water at 20-288ºC. Z’ and Z’’ are area specific and are expressed in Ohm·cm^2.

EIS data obtained from the 12C-1 (Material 12) specimen after heating it the autoclave to 288ºC in simulated PWR water are given in Figure 65-Figure 66. Again, as in the 22C specimen (Material 16), the mid-frequency process is very suppressed, especially at high temperatures, with a summit around 200 Hz. The low frequency process with the summit at ~0.0001 Hz significantly decreases with the temperature increase.

Fits to the EIS data were attempted using both $R_s(R_1(R_2Q_2)Q_1)$ and $R_s(R_1Q_1)(R_2Q_2)$ equivalent circuits. Neither of the equivalent circuits gave an accurate value. Preliminary values are listed in Table 4 and Table 5, respectively.

Table 4: Fitted parameters (preliminary values; to be recalculated) using equivalent circuit $R_s(R_1(R_2Q_2)Q_1)$

Rs(R1[R2Q2]Q1)		22A-1-1	22A-1-1_2	12C-1	12C-1_2	22C-1	22A-1-3	22A-1-3_2
	Rs	6.45E+02	7.09E+02	5.23E+02	4.57E+02		3.72E+02	3.81E+02
	R1	1.11E+05	1.45E+05	3.96E+04	1.20E+05		7.91E+05	5.00E+05
	Q1	3.92E-04	2.11E-04	2.63E-04	2.76E-04		3.65E-05	4.49E-05
	n1	4.21E-01	5.49E-01	2.44E-01	2.25E-01		3.56E-01	3.38E-01
	R2	1.37E+03	1.12E+03	4.42E+03	5.02E+03		2.58E+03	2.60E+03
	Q2	9.26E-03	6.77E-03	9.87E-03	6.81E-03		4.56E-03	4.73E-03
	n2	6.87E-01	7.24E-01	8.41E-01	8.97E-01		6.74E-01	6.17E-01
	R1+R2	1.13E+05	1.46E+05	4.40E+04	1.25E+05		7.94E+05	5.03E+05

The EIS obtained from specimen 22C-1 (Material 16) could not be fit using this model.

Table 5: Fitted parameters (preliminary values; to be recalculated) using equivalent circuit $R_s(R_1Q_1)(R_2Q_2)$.

Rs(R1Q1)(R2Q3)		22A-1-1	22A-1-1_2	12C-1	12C-1_2	22C-1	22A-1-3	22A-1-3_2
	Rs	5.11E+02	5.11E+02	4.02E+02	3.78E+02	1.64E+02	3.74E+02	3.89E+02
	R1	2.02E+03	2.02E+03	6.43E+03	8.86E+03	3.10E+03	2.53E+03	2.53E+03
	Q1	5.14E-04	5.14E-04	3.32E-04	3.63E-04	1.54E-04	3.54E-05	4.28E-05
	n1	2.79E-01	2.79E-01	1.88E-01	1.78E-01	2.10E-01	3.59E-01	3.45E-01
	R2	4.34E+04	4.34E+04	1.00E+04	1.30E+04	6.32E+05	4.74E+05	2.94E+05
	Q2	1.84E-02	1.84E-02	5.72E-02	2.95E-02	6.48E-03	4.78E-03	5.08E-03
	n2	7.51E-01	7.51E-01	9.58E-01	9.23E-01	7.29E-01	6.70E-01	6.17E-01
	R1+R2	4.54E+04	4.54E+04	1.65E+04	2.19E+04	6.35E+05	4.76E+05	2.97E+05

An attempt was made to determine the oxide properties from equivalent circuit analysis. The oxide behaves as a capacitor in the impedance measurements and the overall oxide thickness, d, can be determined as following:

$$d=\varepsilon\,\varepsilon_0 A / Q_1^{1/n1},$$

where ε is dielectric constant of ZrO_2, ε_0 is permittivity of a vacuum, Q_1 is a constant phase element (capacitance), n is the dispersion factor, and A is the sample area. Yet, the conductivity values calculated using the parameters from Table 4 appeared to be inconsistent, within the large range.

In addition, the current-voltage characteristics were measured by sweeping the voltage over +/- 50 mV or +/-100 mV. The specimen resistance was measured from a slope of each i-V curve, $R=V/I$, and plotted in Figures Figure 67a and b. The conductance was determined as $S=1/(R*A)$, where A is the specimen area.

Apparent activation energy of the conductance was calculated from the Arrhenius plots given in Figure 68 and was 10-13 kJ/mol (0r 0.11-0.13 eV). Room temperature data is plotted in Figures 66-67 but were not included in apparent activation energy calculations.

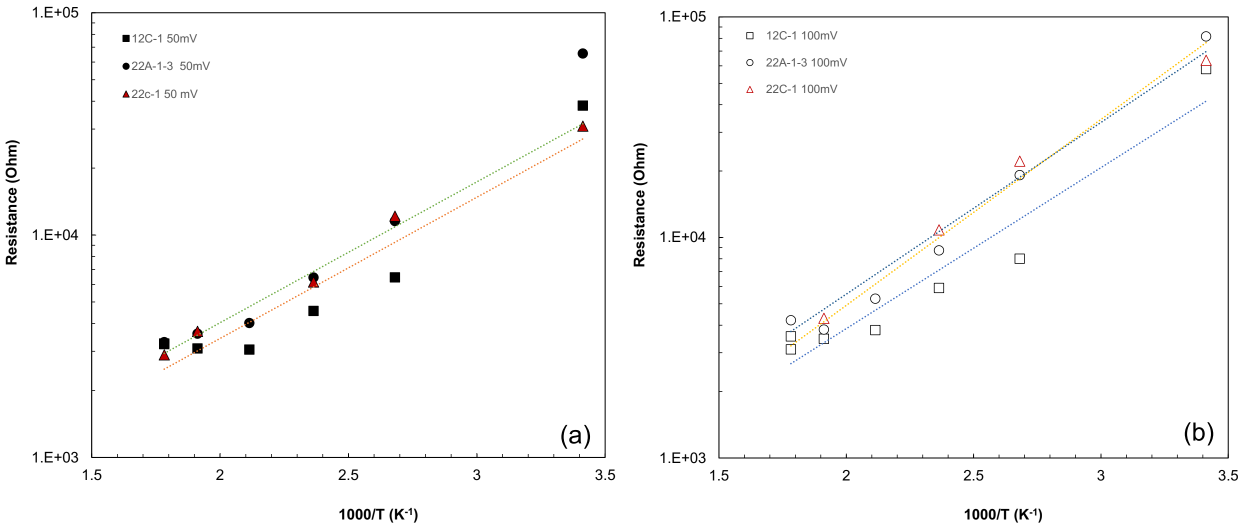

Figure 67: Arrhenius plots of specimen resistance determined from the dc data in simulated PWR water at 20-288ºC.

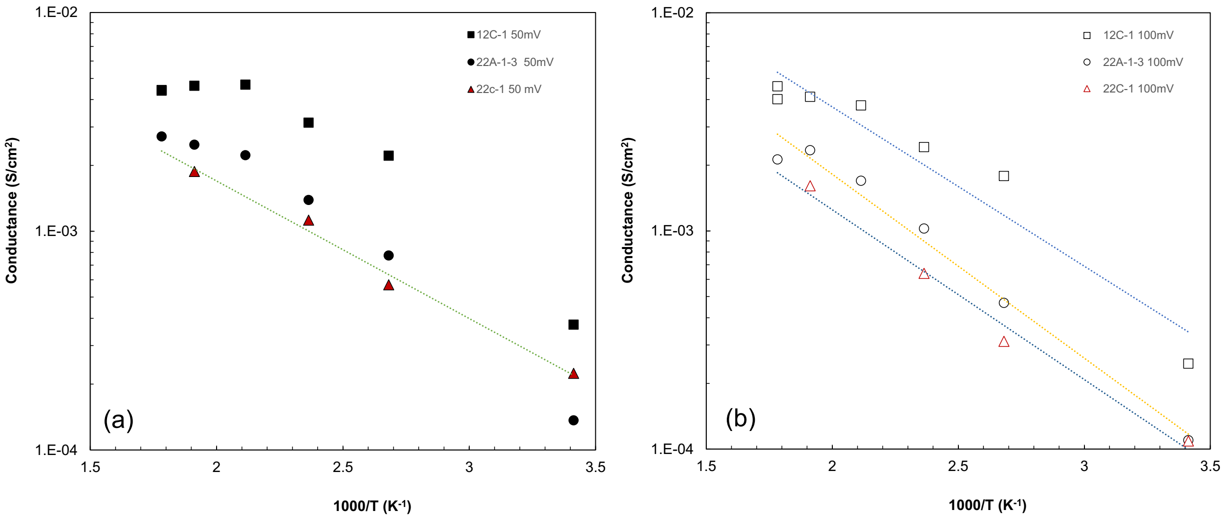

Figure 68: Arrhenius plots of specimen conductance (S/cm^2) in temperature range 20-288ºC.

Conductivity, σ, was calculated following: $\sigma = d/(R*A)$, where A is the specimen area, R is the resistance and d is the oxide thickness. The data from the DC measurements are provided in Table 6

Table 6: Conductivity of specimens determined from the dc data.

Sample name			22A-1-1	22A-1-3	22C-1	12C
Composition			Zr-2	Zr-2	Zr-2	Zr-4
Ni	wt%		0.06	0.06	0.06	0
Known Oxide Thickness	meter	*d*	3.80E-05	3.80E-05	7.00E-06	7.00E-05
dc Resistance at 288C	ohm	R		3299.8	2891.9	3233.3
Area	m^2	A	1.78E-05	1.12E-05	1.45E-05	7.00E-06
Calc. conductivity from dc	S/cm			1.03E-03	1.67E-04	3.09E-03

Efforts to determine the correct equivalent circuits will continue. This will likely be done in conjunction with input from the PIs and their team of experts from other institutions. A careful examination of the tested samples and the oxide films will be conducted to determine if there are extraneous factors that may be not accounted for in the EIS analysis. This could include uneven oxide thickness, local spallation, and insufficient electrical contact in the fixture between the specimen and the Pt wire mesh.

4.2 Electrochemical Corrosion Testing using Design #2 (with Polyimide Insulating Coating)

During Summer 2019, EPRI discussed the initial irradiated fuel channel test results published in the form of a PNNL NSUF report [17] with PNNL and its external collaborators. One of the items discussed during the meetings was protecting the exposed/cut surfaces of test specimens (except the oxide layer) to reduce the active surface and improve the EIS data quality. Various types of insulating materials that could be utilized for this study without affecting the test specimen and oxide layer were evaluated. However, none was identified as a promising insulating coating to be utilized in the autoclave at 288ºC (~1100 psi).

Hence, PNNL conducted a study (see section 3.2) to identify appropriate insulating coating to protect all exposed/cut sides of test specimen (except the oxide layer). Polyimide coating was found to be most promising based upon initial screening.

PNNL’s Design #2 involved the application of Polyimide coating and using the same fixture as described in section 5.1. In order to verify its performance and test the quality of EIS data, unirradiated, oxidized Zr-2 tubes obtained from Studsvik (during November 2019) were selected to apply the polyimide insulating coating and were tested in the autoclave using PWR water at 288ºC (~1100 psi). Design #2 is similar to design # 1 and the only difference is the application of polyimide insulating coating to protect all cut/exposed surfaces except the oxide layer to be studied.

The surface area of the oxide layer is about 1.96 x 10^{-5} m^2 and the oxide thickness (as per the information provided by Studsvik) was about 6 x 10^{-6} m. Efforts were made to study the effect of various excitation potentials (20, 50 and 100 mV) on EIS measurements. In addition, tests were performed to compare EIS and cyclic voltammetry resistance measurements (i.e., AC vs DC measurements). The results showed that the relative data noise decreased with frequency amplitudes up to 100 mV. In addition, the high and low amplitude data appear very similar (see Figures 69-73.

As per the cyclic voltammetry test result (see Figure 71), conductivity$_{dc}$ was determined to be 1.03 x 10^{-3} S/m (R=I/V; Temperature: 290ºC; Run time 1.3 minutes).

As per the EIS measurement performed using 50 mV excitation, the conductivity$_{ac}$ was determined to be 8.75 x 10^{-4} S/m and R=3732 Ω (Temperature, 290ºC; Total time ≈ 10 minutes). The modeled process occurred between 2 and 5 minutes. Three conduction mechanisms were active in this sample, the one with the largest time constant is probably ions in the water, as shown in Figure 72.

As per the EIS measurement performed using 100 mV excitation (see Figure 70), the conductivity$_{ac}$ was determined to be 2.18 x 10^{-4} S/m. This conduction mechanism is slow. As per EIS resistivity data (see Figure 71), the conductivity$_{Bode}$ was determined to be 2.97 x 10^{-4} S/m (R=I/V; Temperature: 290ºC; Run time 18 minutes).

Based upon this study, it was found that when utilizing similar time scales, DC agrees with EIS to within about 15%. It is likely that if the total DC scan had been taken over a 5-minute period, the data would have been in closer agreement. The results showed that three conduction processes are active, and the time constants are in seconds, minutes, and hours. An intermediate PNNL NSUF report [18] covering these details was prepared and shared with NSUF and EPRI during Sep 2020.

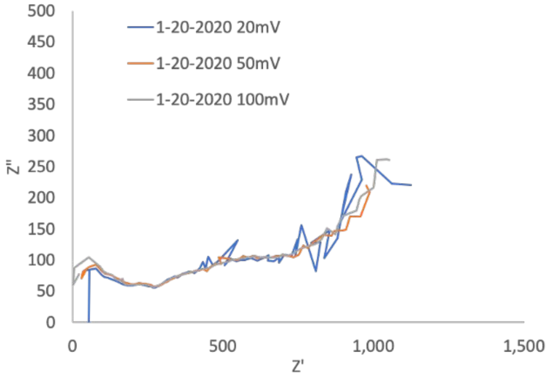

Figure 69: Effect of excitation potential on data noise (Sp# 9; Polyimide coated unirradiated oxidized Zr-2)

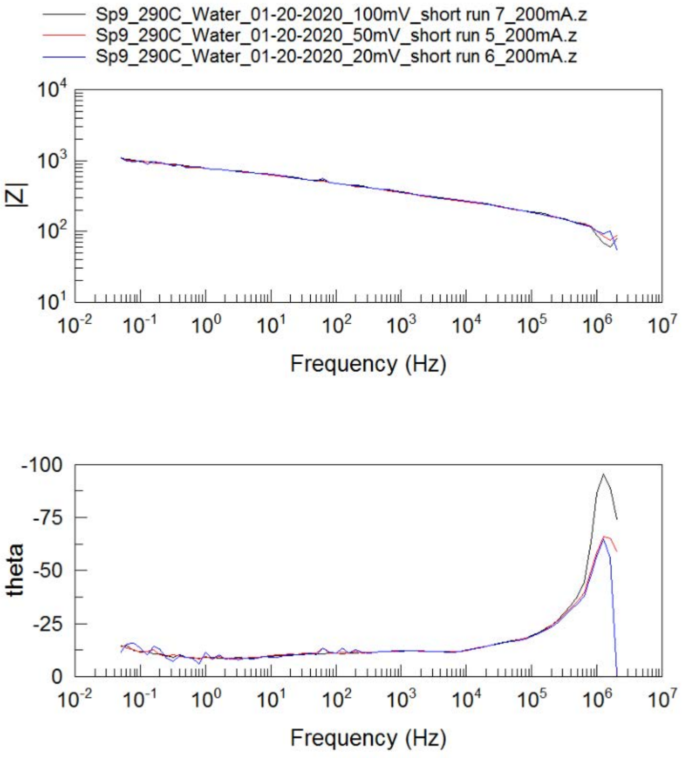

Figure 70: Effect of excitation potential on EIS test data (Sp# 9; Polyimide coated unirradiated oxidized Zr-2)

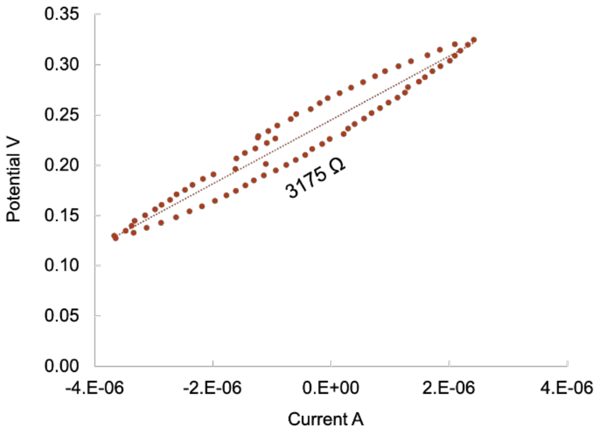

Sp#9_01-17-2020
± 100mV, Scan Rate 5mV/S
Total run time 1 minute 19 seconds

Figure 71: Cyclic voltammetry – DC resistance measurements on Sp# 9 (Polyimide coated unirradiated oxidized Zr-2)

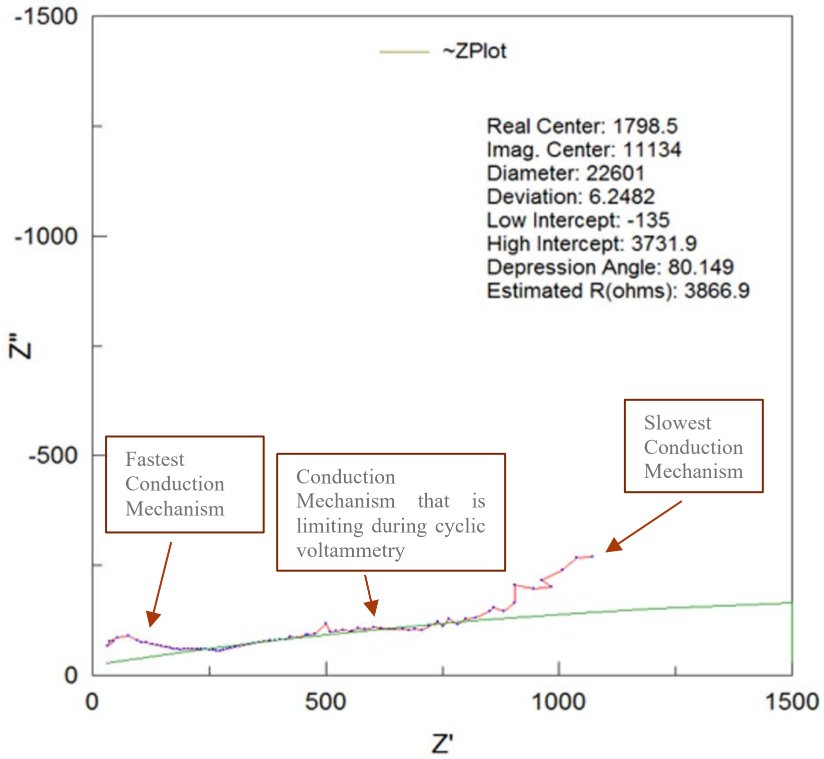

Figure 72: EIS measurements: 50 mV excitation - Sp# 9 (Polyimide coated unirradiated oxidized Zr-2)

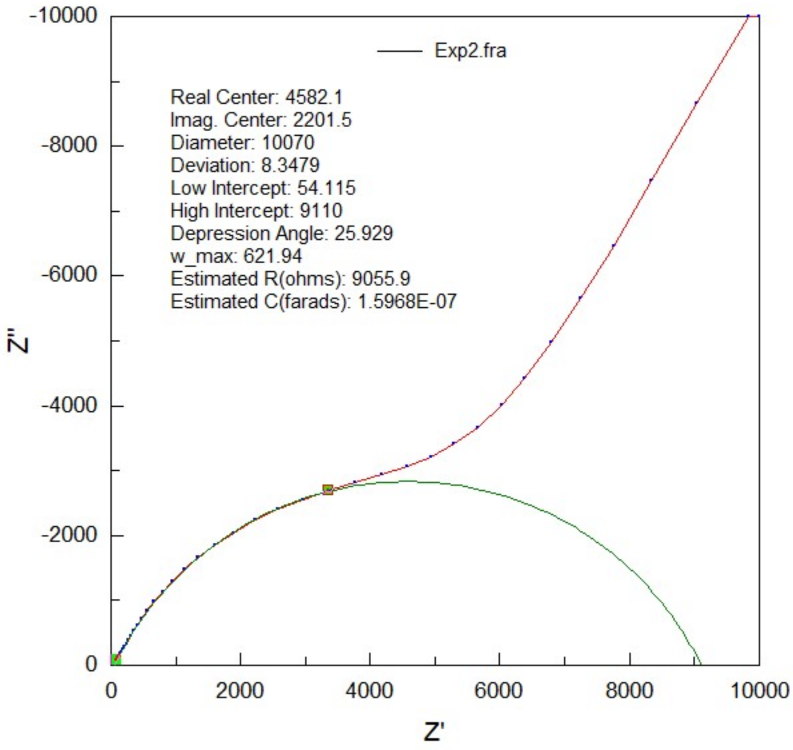

A	2.581E-05
e	22
e_0	8.85E-12
C	1.597E-07
d	3.15E-08 = 31.5 nm

Figure 73: EIS measurement (18 hours) using 100 mV excitation - Sp# 9 (Polyimide coated unirradiated oxidized Zr-2)

- d = thickness
- ε =ZrO_2 dielectric constant = 22
- ε_o = permittivity 8.85E-12
- A = area = 2.58E-5
- C = Capacitance

$$d = \frac{\varepsilon \varepsilon_o A}{C}$$

Figure 74: Equation, constants and variables required to calculate thickness from capacitance

4.3 Electrochemical Corrosion Testing using Design #3 (with Rulon cylindrical sample holder without an Insulating Coating)

During project meetings with EPRI and their collaborators in Spring 2020, emphasis was placed on designing a new fixture that would provide a gap (for electrolyte) between the oxide layer and the counter electrode. Besides the gap, the objective of identifying a new design was to eliminate the utilization of insulating coating to protect cut/exposed surfaces.

Hence, PNNL began an effort to design a new fixture to achieve these two objectives. Once a new design (#3) was identified at PNNL, the concept was shared with EPRI and their collaborators. After a few project meetings, the design was finalized for fabrication. The cutaway illustration of the EIS test fixture and design #3 is shown in Figure 41. The materials utilized in this design are stainless steel, Rulon, Teflon, porous alumina and platinum wire. Refer to section 3.4.3 for additional information about this design.

A unirradiated oxidized Zr-2 tube (see section 2.3) that was previously exposed in an autoclave at 415ºC/90 days with a 6 µm oxide layer was utilized for the trial testing of the fixture. A specimen was sectioned as described in section 3.3 and it was tested using this fixture inside an autoclave at 288ºC with PWR water. The test fixture handled the test environment quite well (see Figure 75).

Figure 75: PNNL Fixture Design #3 (before and after 288ºC testing inside an autoclave with PWR water)

EIS tests (DC potential: 0 V) were performed at 288°C by applying a 100 mV AC amplitude. Based upon these tests, the estimated oxide thickness was in the range of 2.03-2.45 µm, as shown in Figure 76.

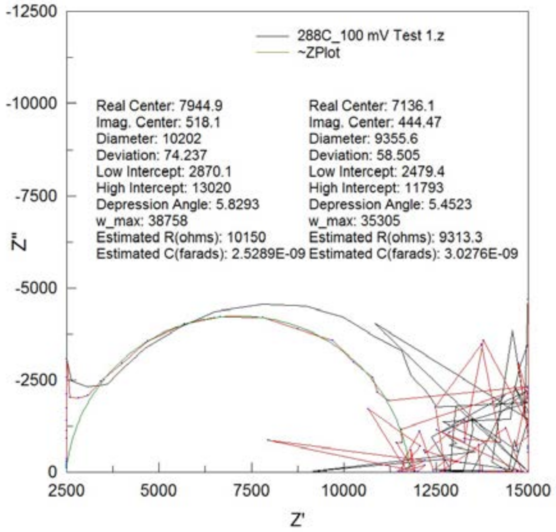

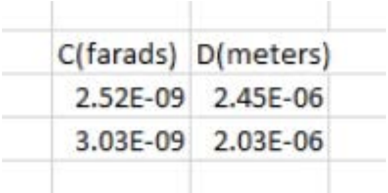

C(farads)	D(meters)
2.52E-09	2.45E-06
3.03E-09	2.03E-06

Figure 76: Estimated oxide thickness (D) from EIS test data (100 mV AC amplitude) - unirradiated Zr water rod sample with a 6-micron oxide layer tested in PWR water at 288ºC.

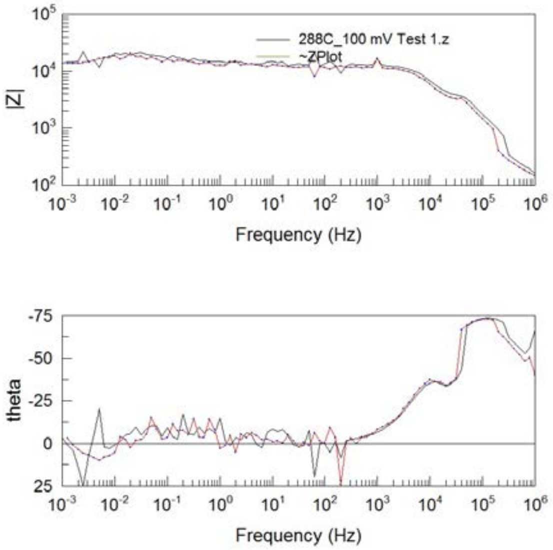

Figure 77: EIS test results obtained from unirradiated Zr water rod sample with a 6-micron oxide layer tested in PWR water at 288ºC.

An EIS repeat test (Figure 78 and 79) was performed at 288°C by applying a 100 mV AC amplitude and the estimated oxide thickness was 1.75 µm and 3.12 µm based upon the larger circle and smaller circle, respectively.

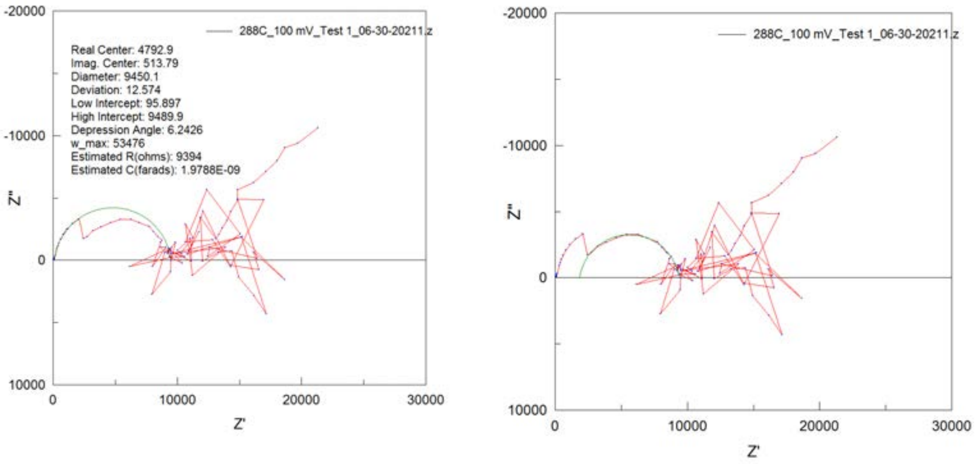

100mV	larger circle		smaller circle	
d	1.75E-06	m	3.12E-06	m
C	3.52E-09		1.98E-09	
e	22		22	
e_0	8.85E-12		8.85E-12	
A_{in}	0.0490625	in	0.0490625	in
A_{cm}	0.316531625	cm	0.316531625	cm
A_m	3.16532E-05	m	3.16532E-05	m

Figure 78: Estimated oxide thickness (D) from repeated EIS test data (100 mV AC amplitude) - unirradiated Zr water rod sample with a 6-micron oxide layer tested in PWR water at 288ºC.

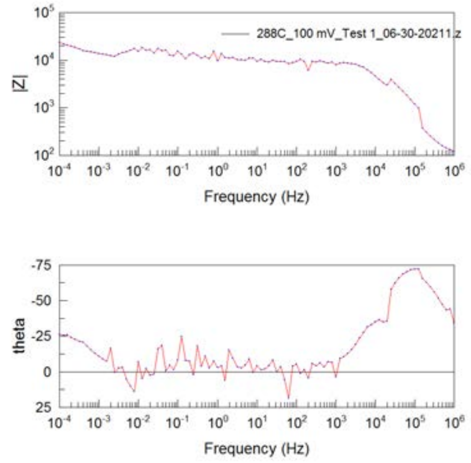

Figure 79: EIS test results (repeat) obtained from unirradiated Zr water rod sample with a 6-micron oxide layer tested in PWR water at 288ºC.

These results were shared with EPRI, and their collaborators and discussions were ongoing to improve the quality of test data at 288ºC.

4.4 Electrochemical Corrosion Testing using Design #4 (with Insulating Coating)

During a late fall 2021 meeting with NSUF and EPRI, a decision was made to step back and perform only room temperature measurements on both irradiated fuel channel and water rod samples and wrap up this project. Earlier, irradiated fuel channel samples were tested up to 288ºC using PNNL fixture design #1.

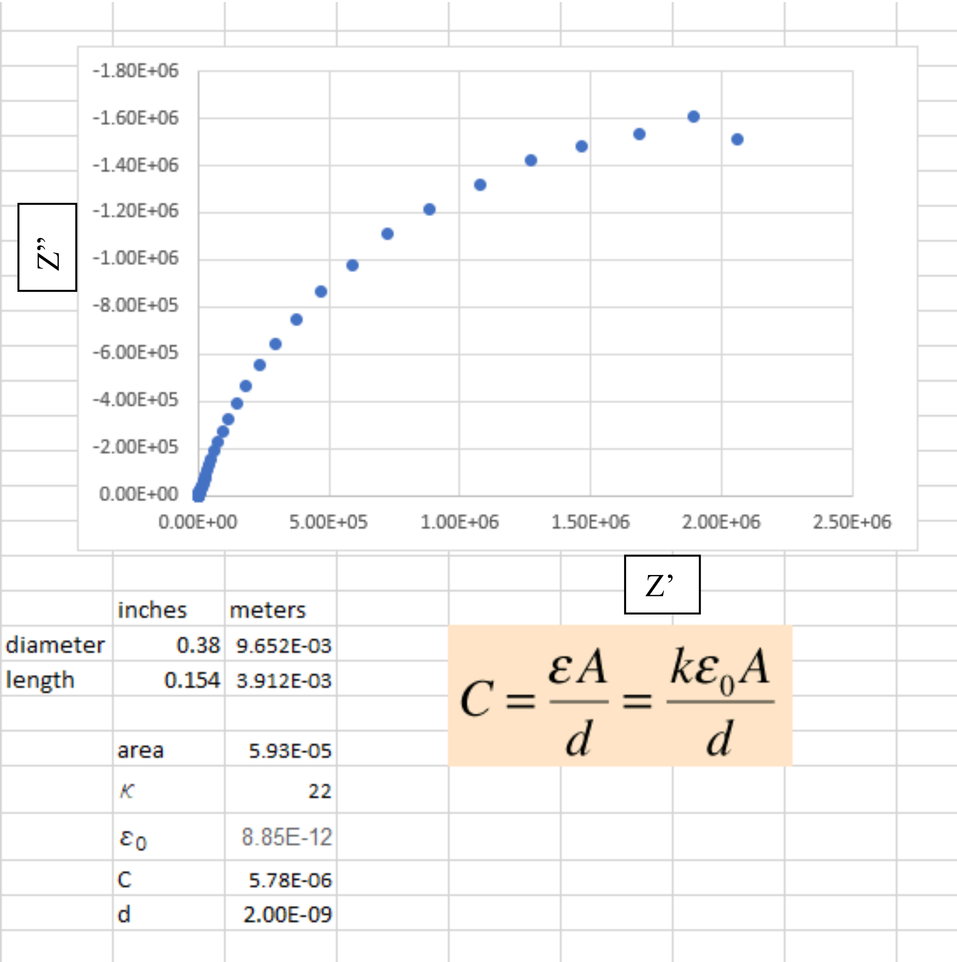

	inches	meters
diameter	0.38	9.652E-03
length	0.154	3.912E-03
	area	5.93E-05
	κ	22
	ε_0	8.85E-12
	C	5.78E-06
	d	2.00E-09

$$C = \frac{\varepsilon A}{d} = \frac{k\varepsilon_0 A}{d}$$

Figure 80: A 6-micron oxide sample - Nyquist plots and thickness determination

See the section 3.4.4 for information related to the fixture design #4 for room temperature testing of irradiated fuel channels and water rods. This design involved the use of insulating coating (epoxy). Initially, unirradiated water rods with two levels (one and six micron; see section 2.3) of oxide thicknesses were utilized to perform trial EIS testing using 0.5 M sodium sulfate solution at room temperature. Nyquist data plots are given as Figures 80 and 81. κ is permittivity of material in F/m; ε_o is permittivity of vacuum in F/m; R is resistance in ohms; C is capacitance in F; d is the thickness in m. Based upon the EIS testing, the estimated oxide thickness is in the range of nm instead of µm. See section 4.5 for additional information.

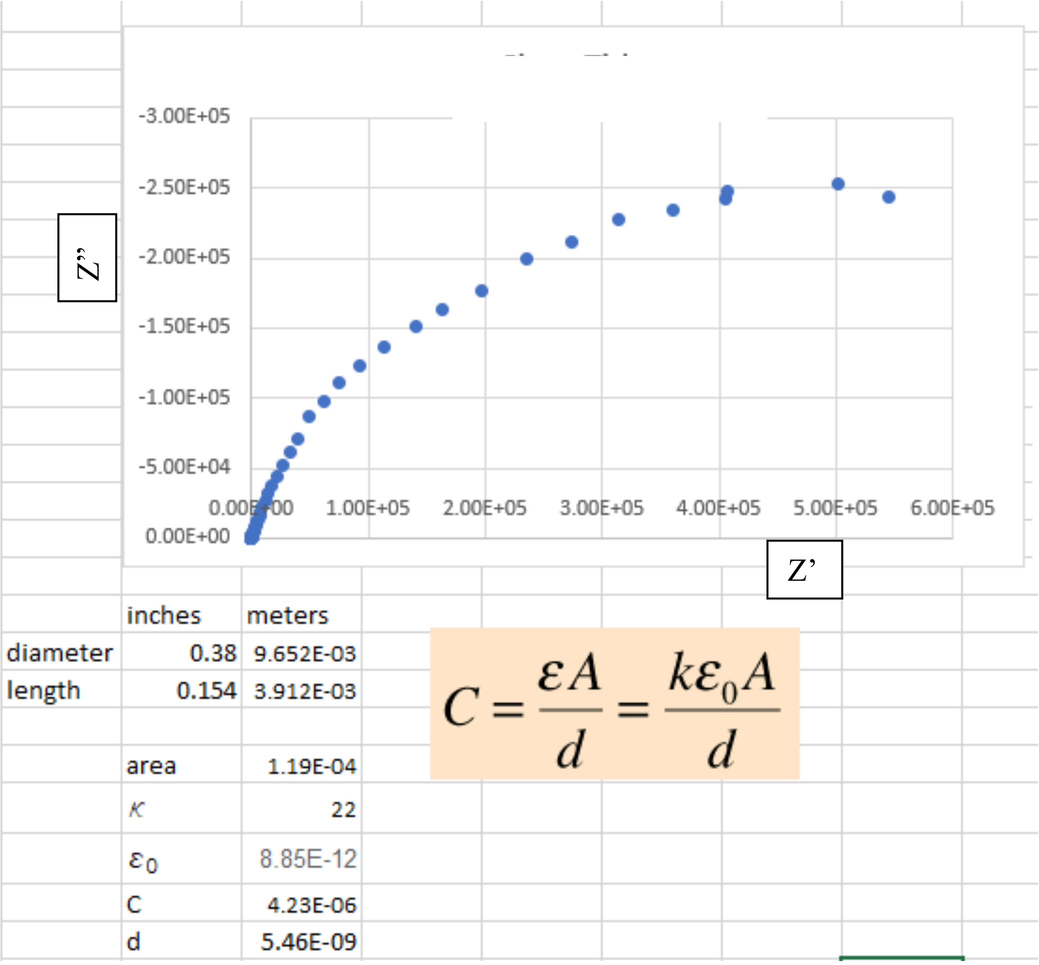

	inches	meters
diameter	0.38	9.652E-03
length	0.154	3.912E-03
	area	1.19E-04
	κ	22
	ε_0	8.85E-12
	C	4.23E-06
	d	5.46E-09

$$C = \frac{\varepsilon A}{d} = \frac{k\varepsilon_0 A}{d}$$

Figure 81: A 1-micron oxide sample nyquist plots and thickness determinization

EIS tests (DC potential: 0 V) were performed on irradiated fuel channel and water rod samples using PWR water at room temperature by applying 100 mV AC amplitude. A few tests were also performed using lower AC amplitudes, but this showed considerable noise and was abandoned in favor of 100 mV. Figure 82 shows a typical EIS plot with clearly separated RC arcs. Figure 83 shows a typical plot where the EIS arcs are not clearly seperable. Table 7 shows various information (capacitance, resistance and estimated thickness based on EIS data) about the oxide layer of irradiated fuel channel and water rod samples.

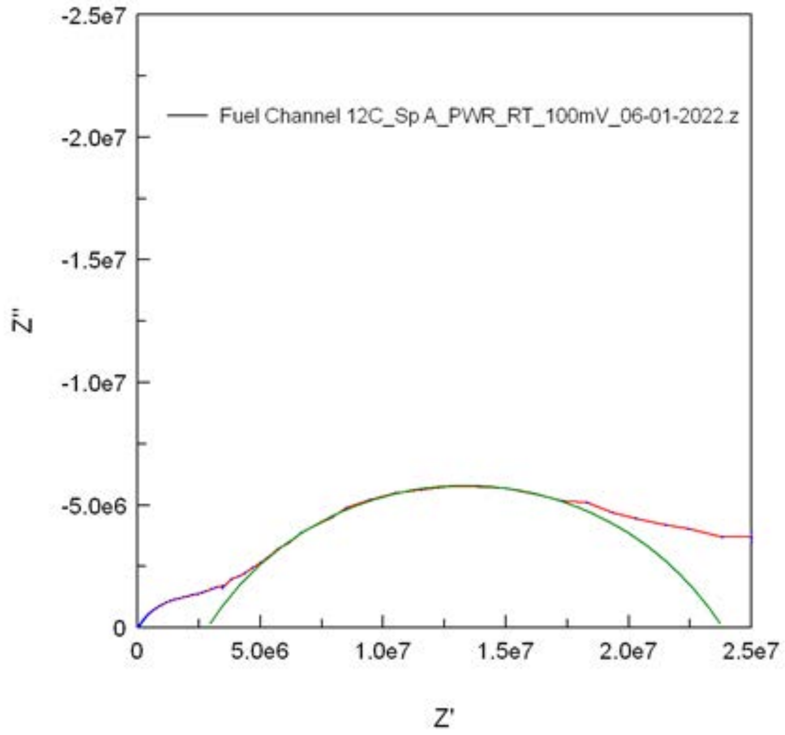

Figure 82: Typical EIS data with clearly separated RC arcs - obtained from irradiated fuel channel sample 12C (Material 12)

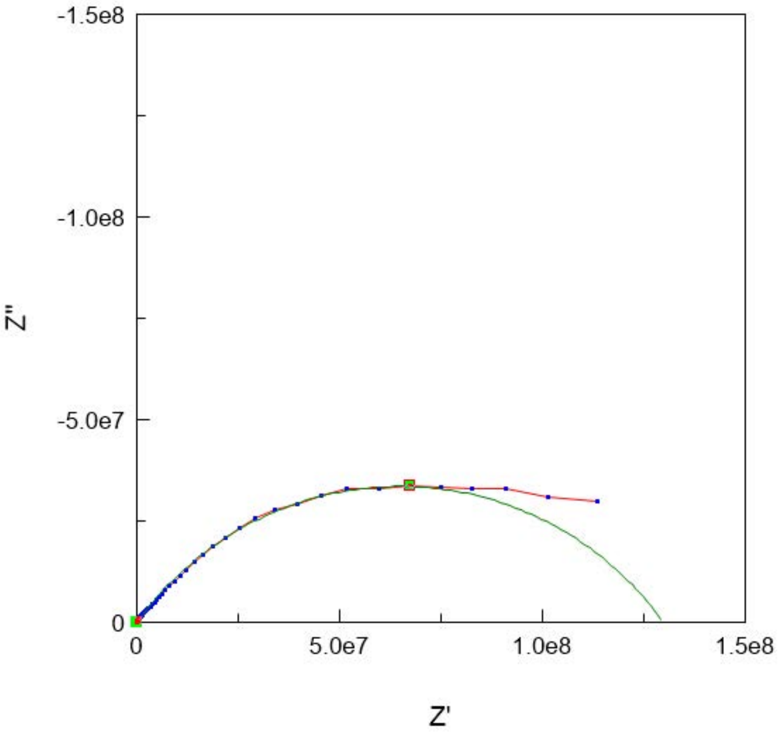

Figure 83: Water Rod 18859, Typical data where the EIS arcs are not clearly seperable

Table 7: Irradiated fuel channel and water rod data, where multiple arcs were clearly separated the second arc is given below the first

Fuel Channel	C (f)	R (Ω)	D (m)	D (nm)
12C Sp A (Material 12)	1.74E-07	2.46E+07	5.54E-08	55.4
12C Sp A; second arc (Material 12)	4.58E-09	5.20E+06	2.10E-06	2100
22C Sp A (Material 16)	8.09E-06	2.47E+06	6.59E-10	0.66
12A SP 1 (Material 12-1)	5.31E-07	7.66E+06	8.03E-09	8.0
22A SP A1 (Material 16-1)	2.46E-06	1.07E+07	2.80E-09	2.8
Water Rod				
18847 (Material 10)	2.09E-09	1.11E+07	3.91E-06	3960
18850 (Material 13)	3.14E-07	4.63E+07	4.96E-08	50
18850 (Material 13) second arc	1.06E-07	1.22E+07	1.47E-7	147
18855 (Material 21)	2.44E-08	3.06E+06	3.69E-07	369
18859 (Archive 1)	2.95E-07	1.30E+08	2.19E-08	22

When preforming EIS analysis, it is important to remember that, for the analysis to be valid the different arcs must be clearly separable. We are assuming that the oxide scale is dense, and any pores or cracks are not communicating electrically to the water surface within the scale. This is clearly not the case. In our case there is a distribution of oxide thicknesses that are communicating to the liquid. In an ideal situation the radii of these arcs reside on the Z' axis. The fact that the radii is below the Z' axis implies that instead of a single oxide thickness, these oxides have a distribution of thicknesses. This distribution of thicknesses produces arcs that are not clearly separable in most of the samples. Although some of the samples exhibited two separable arc distributions. The "12C Sp A (Material 12)" and the "18847 Material 10" exhibited EIS arcs that are consistent with dense oxide scales in the micron range. Samples "18850 Material 13" and '18855 Material 21" have EIS arcs that are consistent with oxide scales in the tenths of a micron. All samples exhibited further arcs in the nanometer range as well.

4.5 Microstructural Characterization of Oxide Scales

4.5.1 Unirradiated Zr-2 Tube, 50 mm, RR2015, 500°C for 72 days, 5-9 µm oxide layer

The SEM analysis of this tube confirmed that the oxide layer was typically >5 um on the outer surface of the tube, as shown in Figure 84. Laminar cracks/pores are present that are aligned parallel to the M/O interface, and in isolated regions nanopores are present within 200 nm or less from the M/O interface. The base metal shows evidence of hydride platelets, some of which may be surface hydrides introduced from the colloidal silica polish.

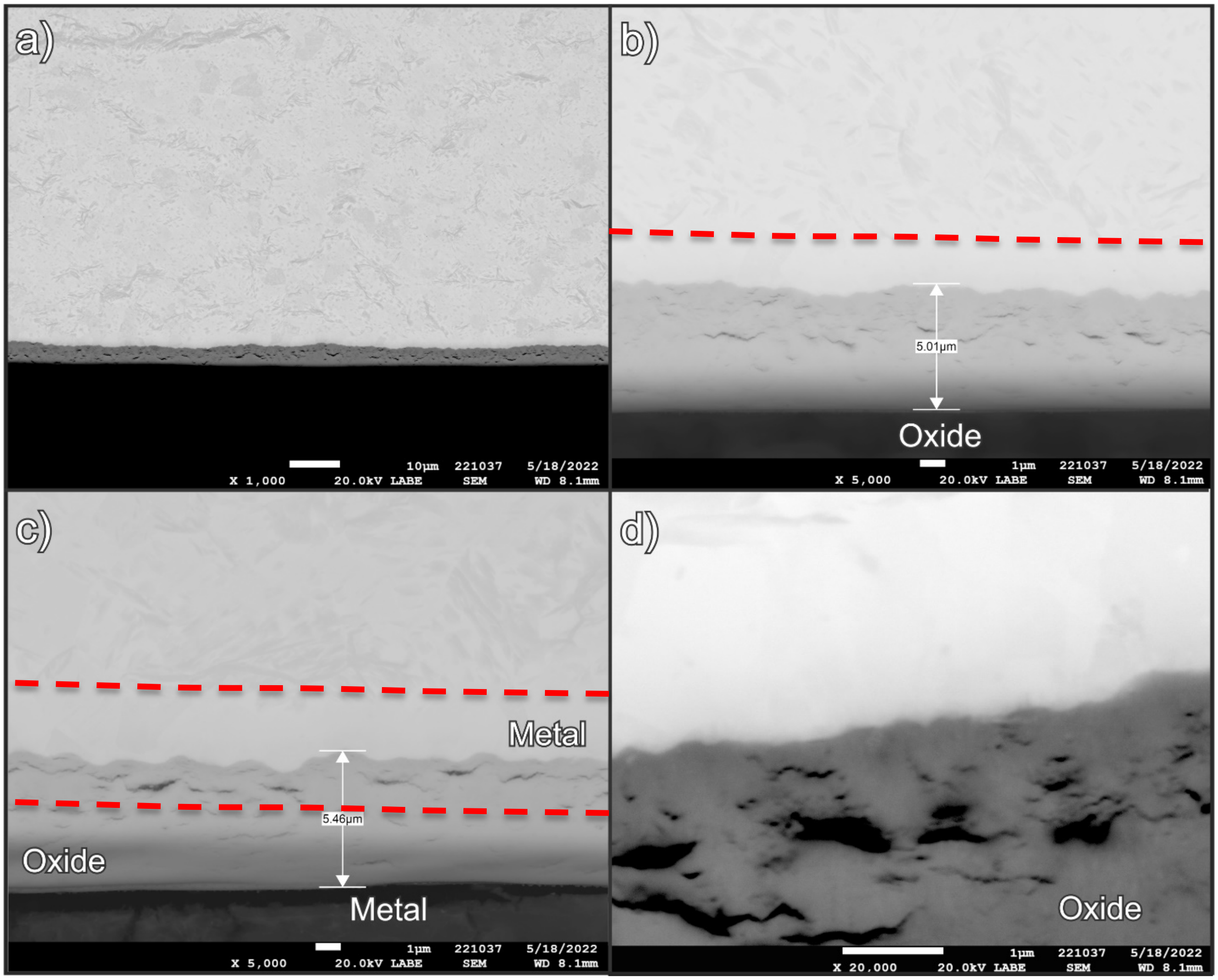

Figure 84: Unirradiated Zr-2 Tube, 500°C for 72 hours, 5-9 µm oxide layer: Backscatter SEM images are provided that confirm the nominal thickness of the outer oxide layer. The image in (d) shows that some of the pores are within 200 nm of the metal/oxide interface. The red dashes in (b) and (c) show a region with minimal contrast, and no evidence of hydrides. This region may have polished differently due to compressive stresses near the M/O interface that are relaxed past a certain distance from the M/O interface.

4.5.2 Unirradiated Zr-2 Tube, 50 mm, RR2013, 400°C for 3 days, ~1 μm oxide layer

In the case of the oxide scale grown for a short duration, the degree of laminar porosity is lower, but some of the pores are still present within 200 nm or less of the M/O interface. The band of minimal contrast observed in the previous sample is not present in this sample (see Figure 85).

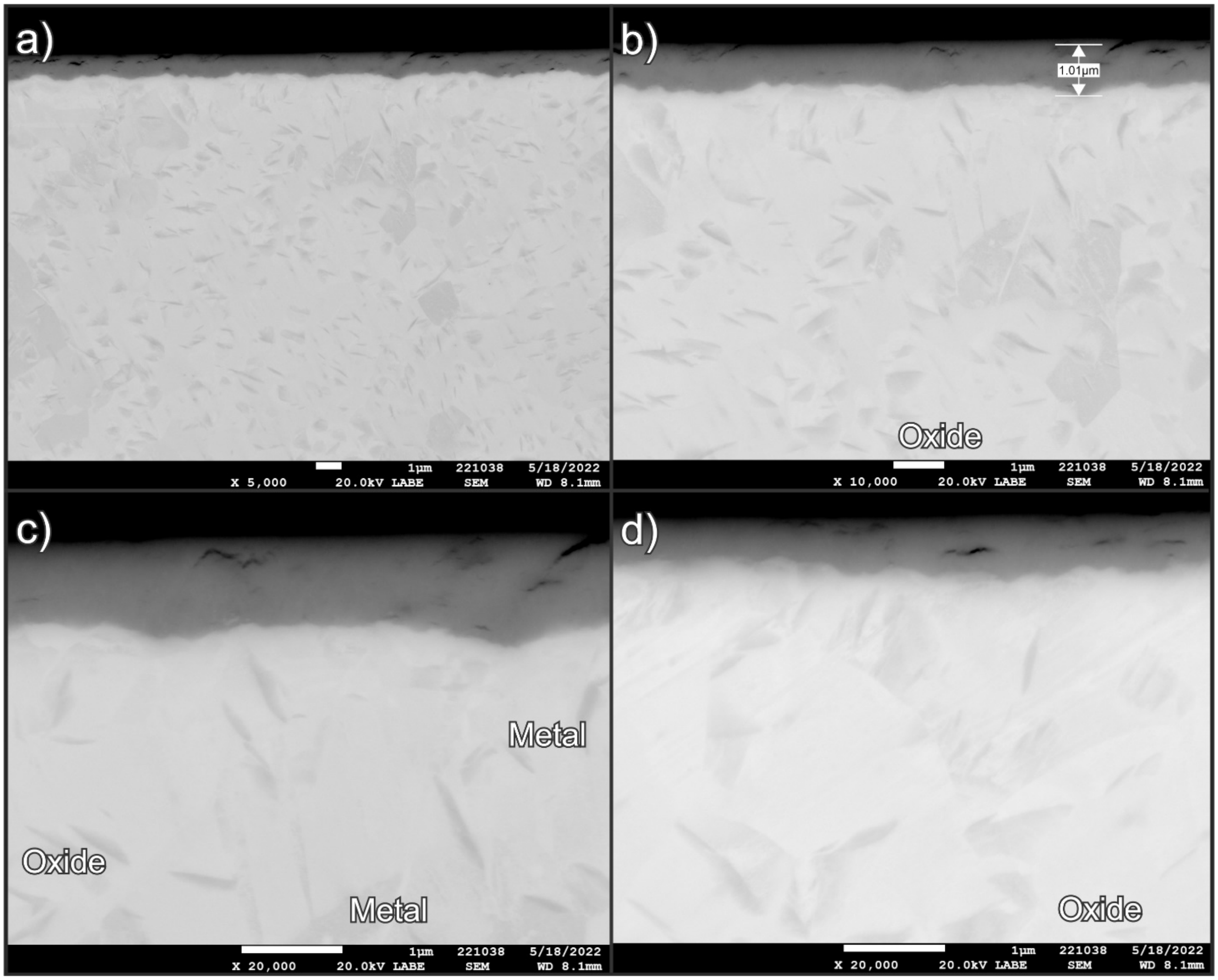

Figure 85: Unirradiated Zr-2 Tube, 400°C for 3 hours, ~1 μm oxide layer: Backscatter SEM images are provided that confirm the nominal thickness of the outer oxide layer. The image in (c) and (d) show that some of the pores are within 200 nm of the metal/oxide interface. Under these exposure conditions, there was no evidence of the band of minimal contrast as shown in the previous figure, and the hydrides are visible up to the M/O interface.

4.5.3 Unirradiated Zr-2 Tube, 20 mm, RR2013, 415°C for 90 days, ~6 µm oxide layer

For this condition the microstructure was examined using both SEM and STEM, revealing similar features as observed for the thicker oxide grown at 500°C. The SEM images also show a region of minimal contrast, as outlined by the red dashes in Figure 86. The SEM images demonstrate that the laminar porosity is often in contact with the M/O interface. The STEM images confirm this behavior, as shown in Figures 87 and 88.

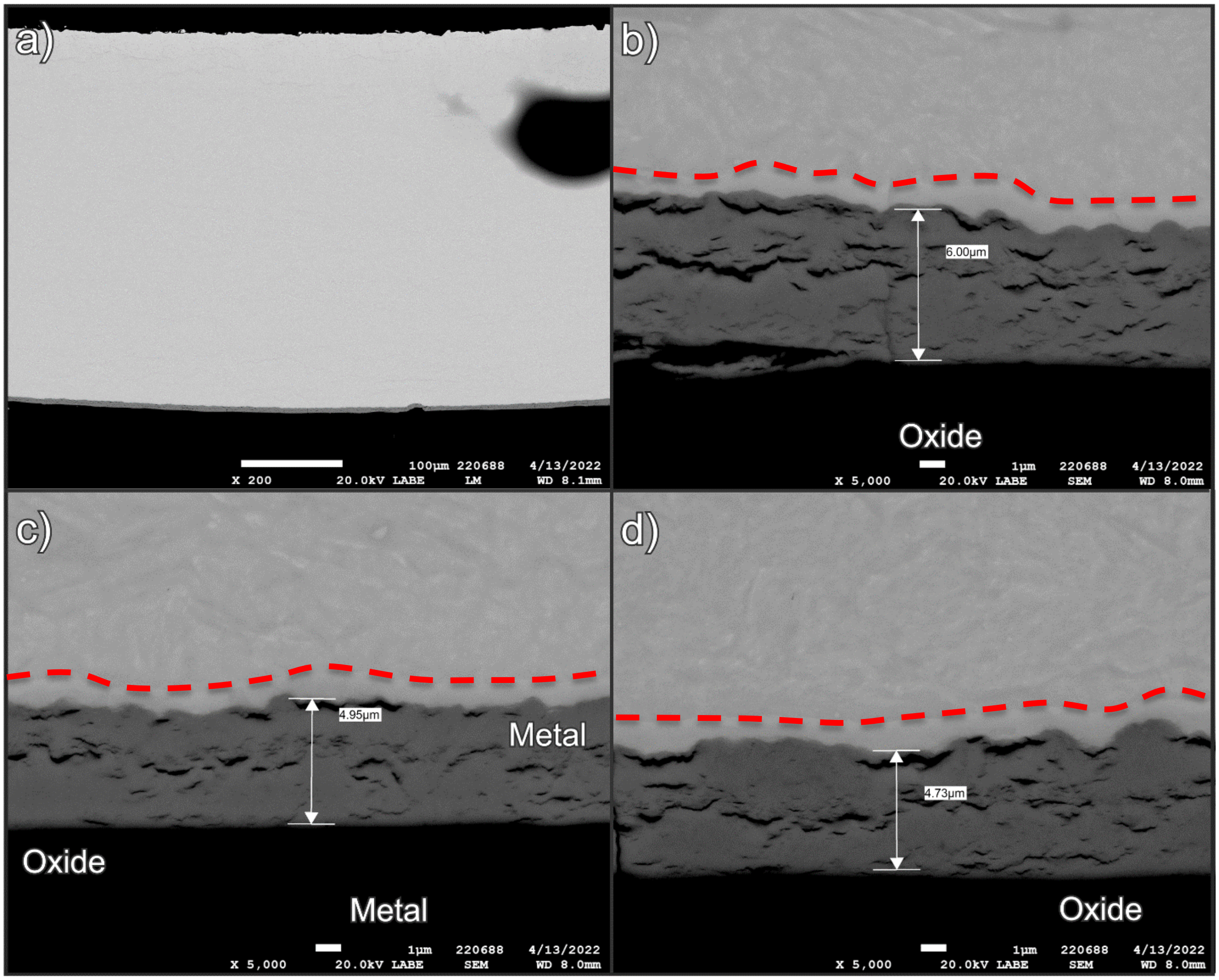

Figure 86: Unirradiated Zr-2 Tube, 415°C for 90 hours, ~6 µm oxide layer: Backscatter SEM images are provided that confirm the nominal thickness of the outer oxide layer. The images show considerable laminar porosity, some of which are within 200 nm of the metal/oxide interface and appear to intersect the M/O interface. The red dashes in (b) and (c) show a region with minimal contrast, and no evidence of hydrides visible further away from the M/O interface. This region may have polished differently due to compressive stresses near the M/O interface that are relaxed past a certain distance from the M/O interface.

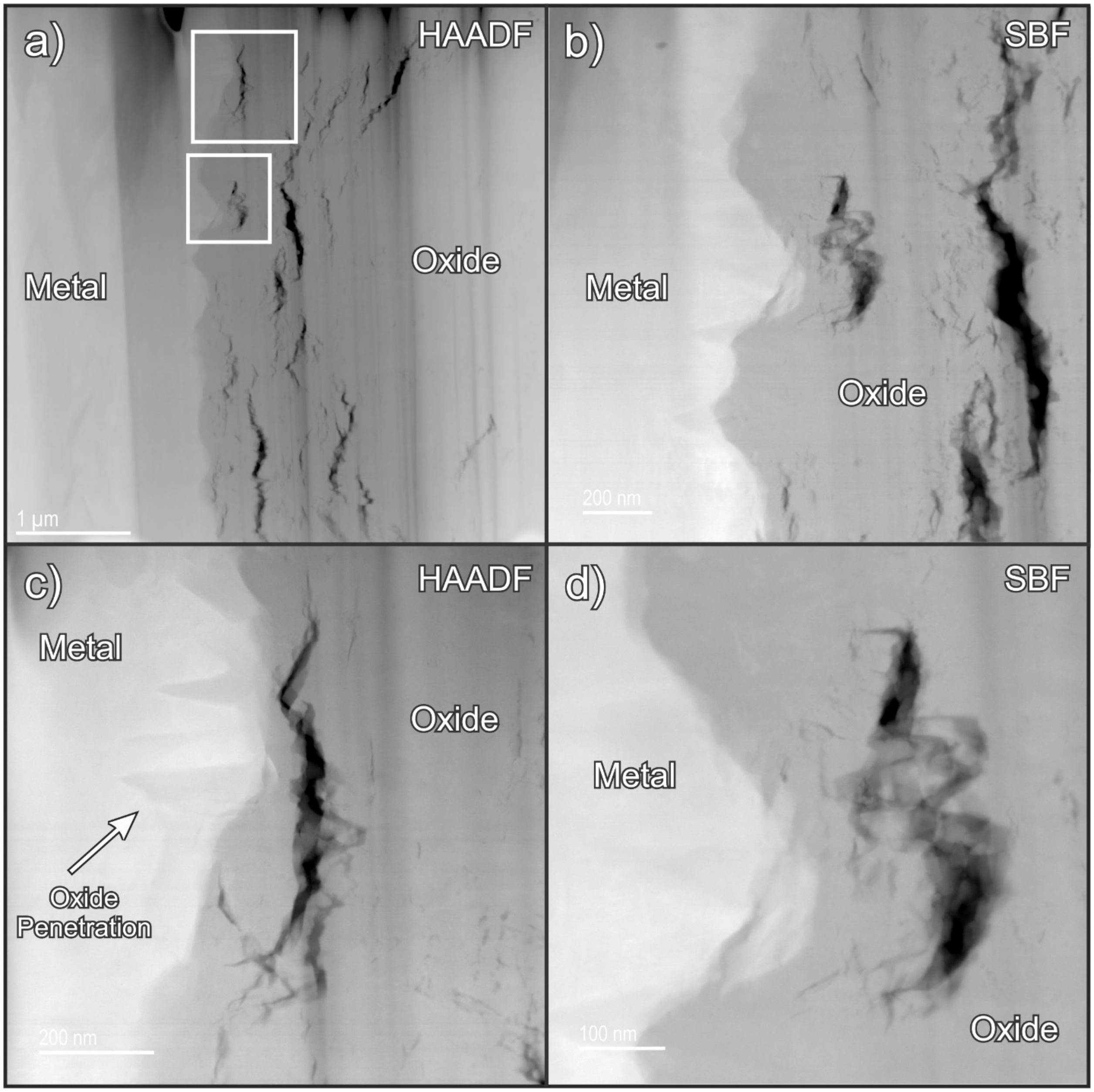

Figure 87: Unirradiated Zr-2 Tube, 415°C for 90 hours, ~6 µm oxide layer; STEM High angle annular dark field reveals the fine scale nano-porosity that is comes in contact with the metal-oxide interface. There are tendrils of oxide that have penetrated into the metal from these regions where the nano-pores are in contact with the M/O interface.

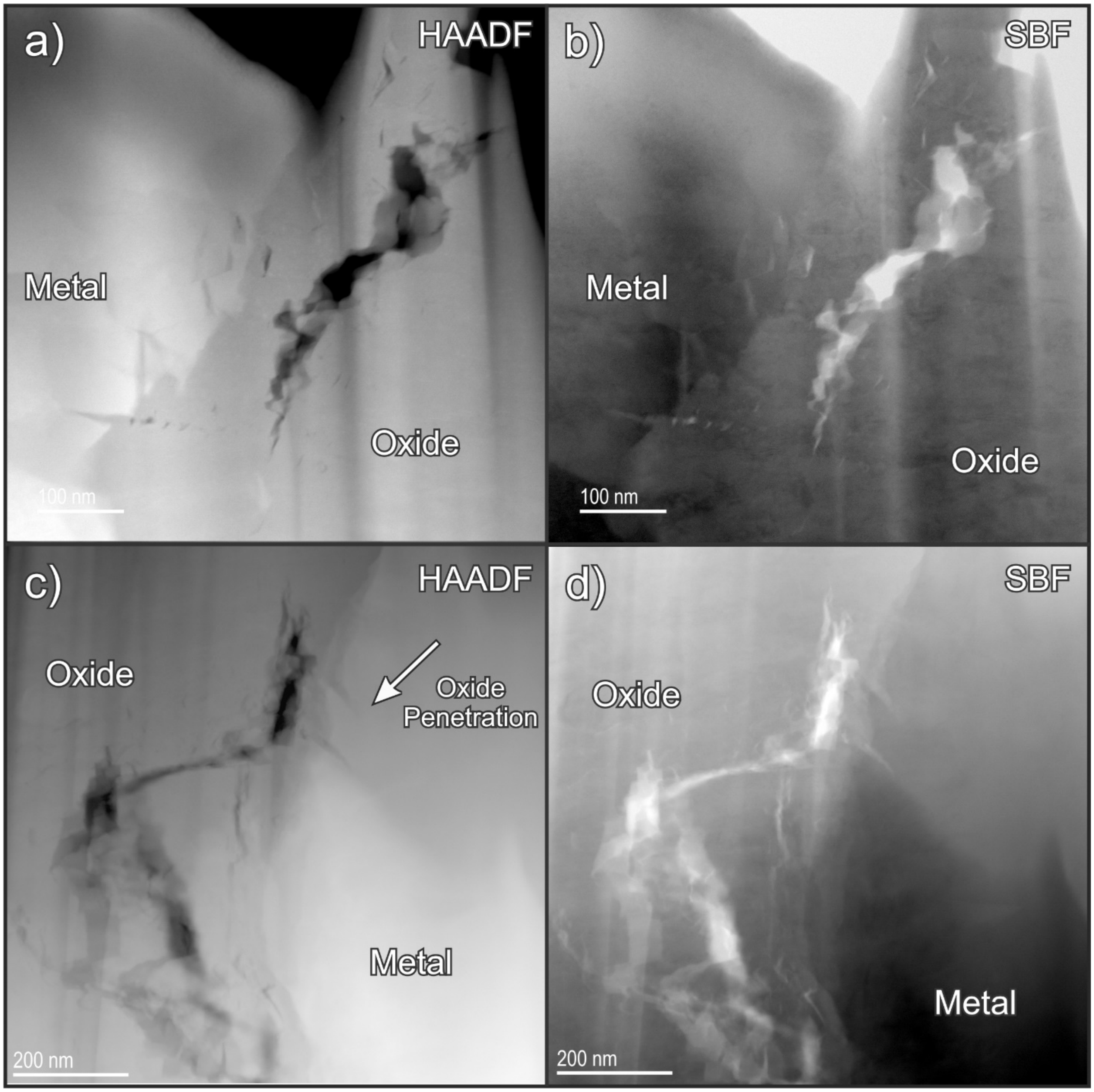

Figure 88: Unirradiated Zr-2 Tube, 415°C for 90 hours, ~6 µm oxide layer: Additional examples are shown of the nano-porosity that in some cases, intersects the M/O interface.

4.5.4 Irradiated Fuel Channels

STEM high angle annular dark field images and bright field images are provided in Figures 89-92 that illustrate a nature of the oxide film near the metal in the irradiated fuel channel Material 16-1, Material 16 and Material 12-1. The main thrust of this STEM analysis was to confirm the distribution of porosity and cracks that may have allowed water to reach the metal during EIS testing, or if not in contact with the metal directly, reduced the depth of dense oxide that separates the metal from the reactor water that likely penetrates through the pores in the film. The metal/oxide interface is wavy and uneven at the nanoscale, with a sawtooth appearance. The oxide grain structure within the first 500-2000 nm consists of a fine grained, columnar network of grains whose orientation follows the curvature of the metal/oxide interface, but eventually that orientated oxide appearance gives way to fine grained equiaxed oxide grains that lose the oriented morphology. The columnar grains are in the range of 25 nm, while in the equiaxed regions the grains are typically in the 50 nm or greater range. Elemental mapping didn't reveal any Fe, Cr, Sn or Ni discernible elemental segregation in the oxide film beyond the occasional second particle remnant.

Both the STEM bright field and HAADF images reveal that in each of the samples there are nano-pores and cracks within 200 nm of the M/O interface. The images in Figures 90 and 91 show definitive evidence of nano porosity in contact with the M/O interface. This distribution of porosity may create a network of interconnected pores and cracks that allows the autoclave's pressurized water to percolate near to or actually come in contact with the metal. This may explain why the EIS results predict oxide films that range from nanometers to microns (when can measure many microns of oxide in the SEM and optical microscope), it is effectively capturing the effect of the interconnected porosity which may be highly variable across the sample.

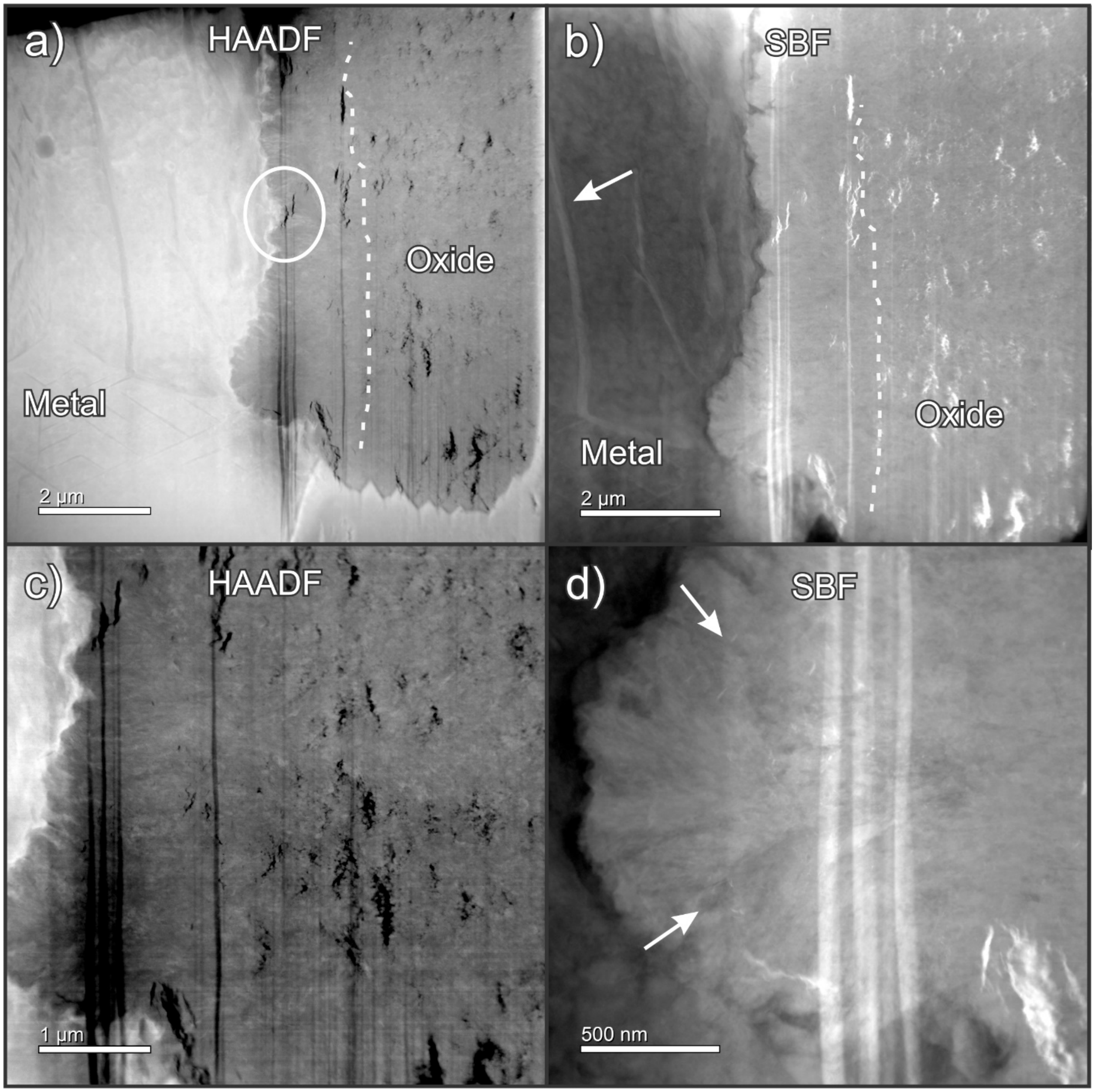

Figure 89: Material 16-1: STEM bright field and high angle annular dark field images show that 1-2 μm of relatively dense columnar oxide exists near the M/O interface, which then transitions to a more equiaxed grain structure past the dashed line in (a) and (b). The arrows in (d) point to small nanopores that are present within a 200 nm or less from the M/O interface.

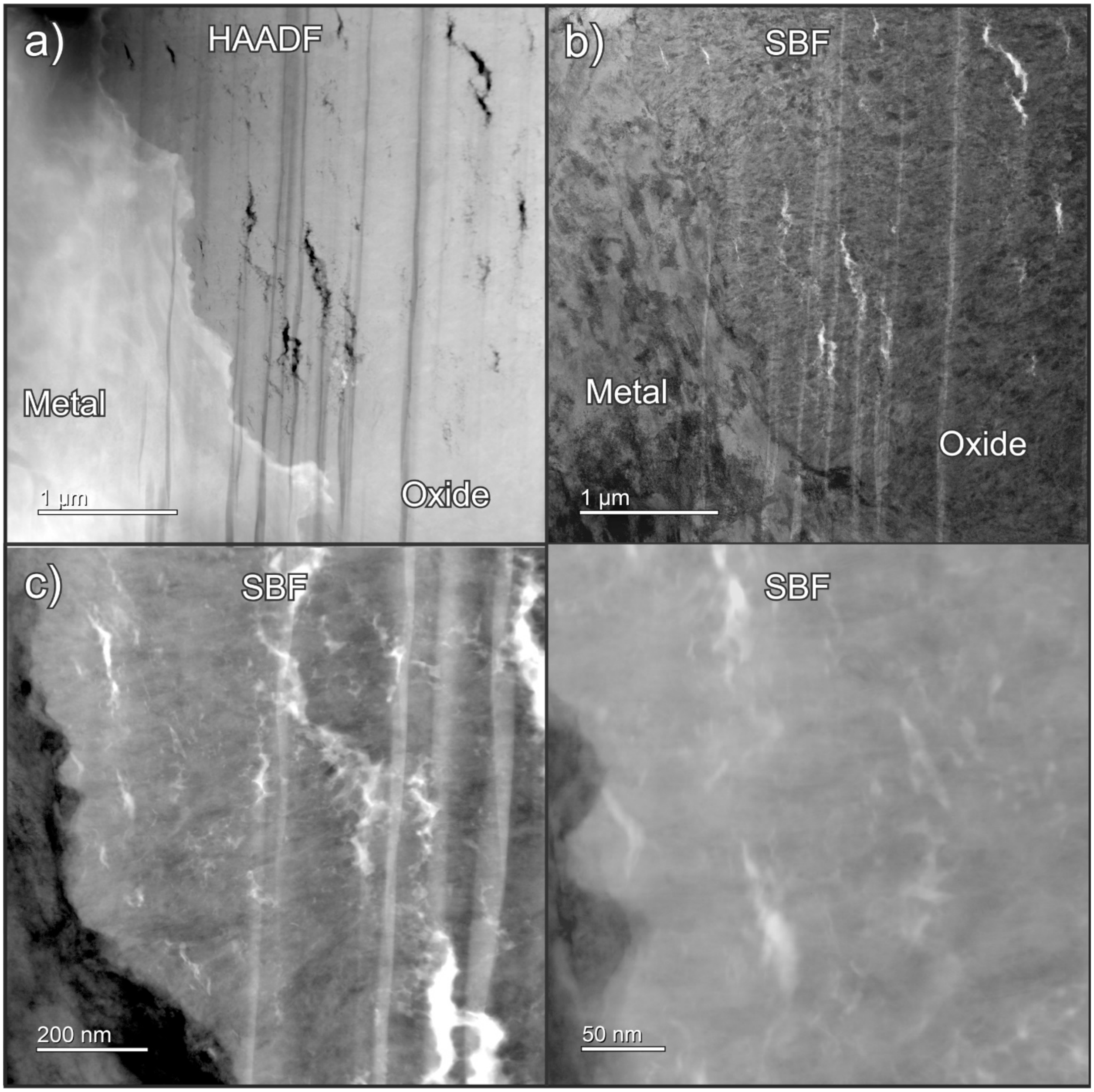

Figure 90: Material 16: STEM bright field and high angle annular dark field images were taken to document the differences in porosity. A high density of laminar pores exist that are aligned parallel to the M/O interface. The oxide layer near the M/O interface is not as dense and doesn’t appear as a distinct layer as in the case of 22A. The porosity is present in this layer and in direct contact with the M/O interface.

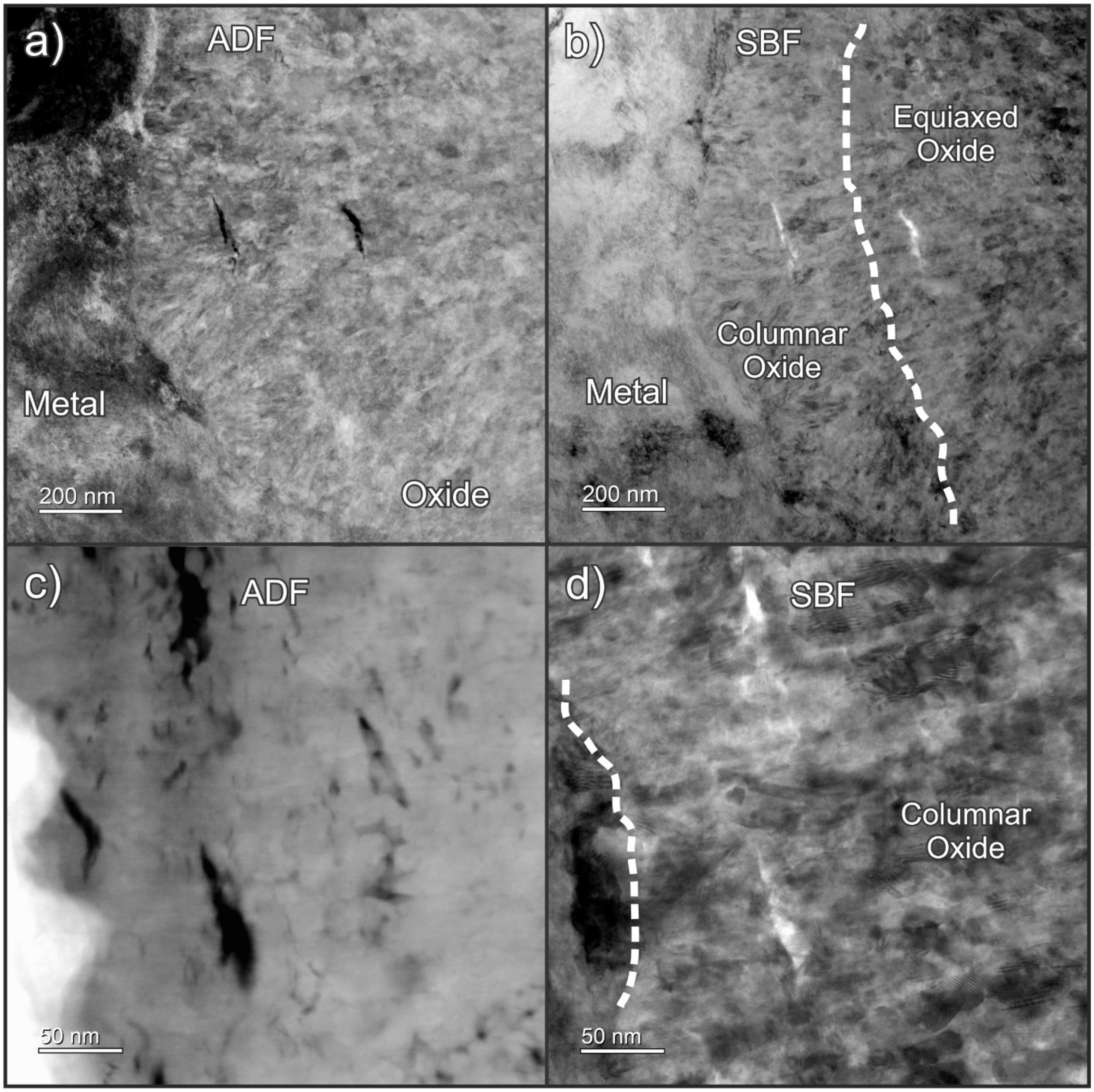

Figure 91: Material 16: Additional STEM bright field and high angle annular dark field images are provided that show the presence of small nanopores and cracks in contact with the M/O interface. The dashed line in (b) represents the transition from columnar to equiaxed oxide, and the dashed line in (d) indicates the metal/oxide interface.

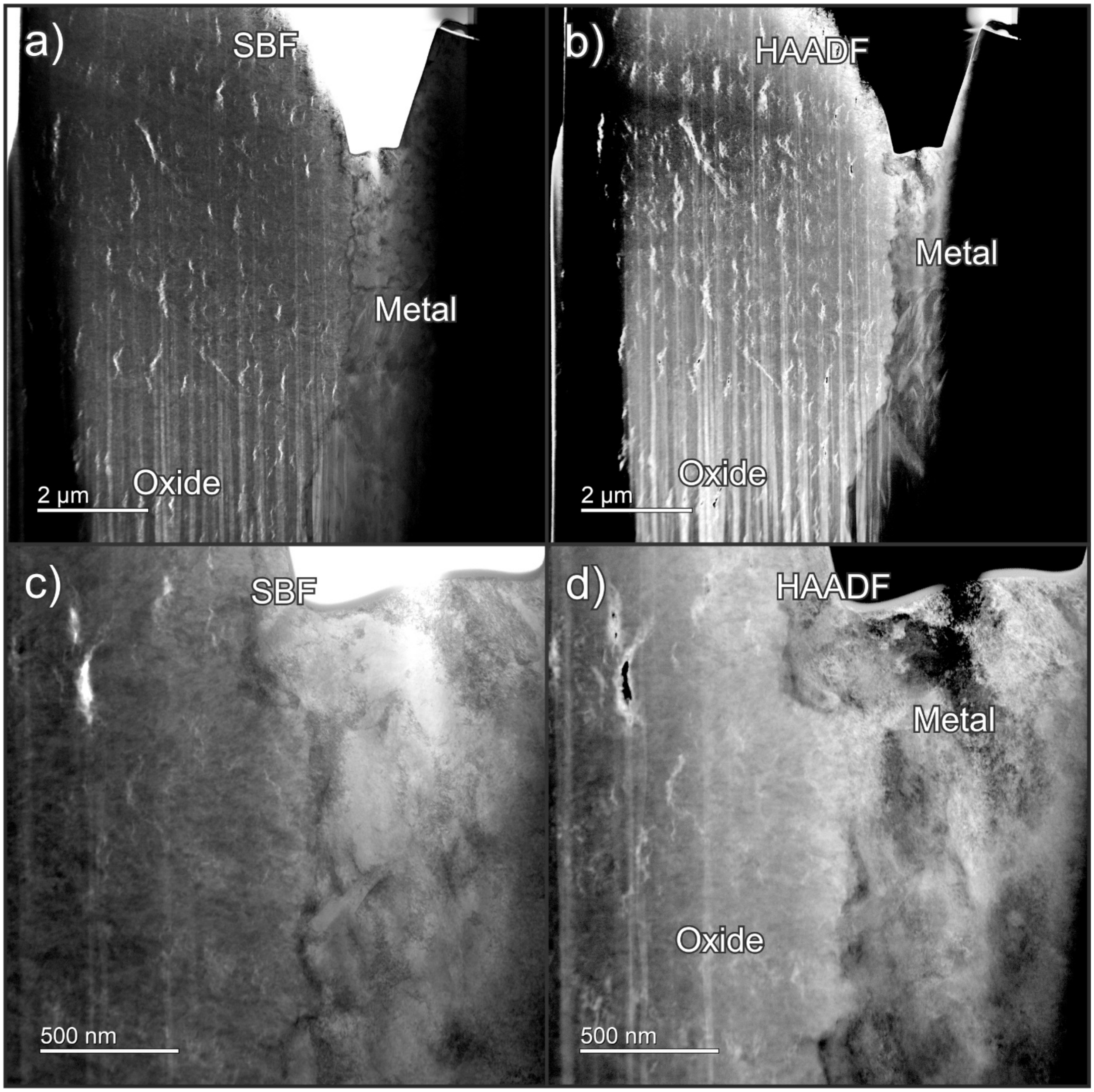

Figure 92. Material 12-1: STEM HAADF and bright field images show a highly porous oxide, with laminar pores aligned parallel to the M/O interface. A dense oxide is present near the M/O interface, and there is little evidence of pores in contact with the interface.

5.0 Summary of Work

Using an instrumented autoclave operating at 288°C and 1100 psi, electrical impedance spectroscopy (EIS) measurements were taken from three neutron irradiated fuel channel samples (Zircaloy-2 and Zircaloy-4). The three high priority fuel channel samples were tested at 288°C using a simulated PWR water with the AC frequency range extending down through 10^{-4} Hz, with corresponding DC measurements to validate the resistance measurements. EIS measurements were also taken at room temperature using a simulated PWR water from four neutron irradiated fuel channel samples (Zircaloy-2 and Zircaloy-4). and four water rod samples (Zircaloy-2). EIS measurements were also performed on unirradiated Zircaloy-2 tubes that were previously oxidized in autoclaves at various temperatures for different time durations to obtain oxide layers of different thicknesses.

EIS measurements were performed along with supporting microstructural characterization on the oxide and metal/oxide interface. These experiments proved to be more challenging than anticipated because of the small size of the samples, which required development of fixtures to allow valid testing of the materials, some of which are radioactive, under pressure and temperature.

At the start of this work, it was assumed that despite the laminar cracks and porosity visible in both optical and SEM, the oxide scale is dense near the metal, effectively preventing the water from contacting the metal directly. While it is generally accepted that the large laminar cracks pores allow the water to percolate into the oxide film, it is unknown just how deep it can go, and how interconnected is the porosity, which will dictate how much the porosity is connected electrically to the water within the oxide scale. The EIS results demonstrate that there is in fact a distribution of oxide thicknesses over the various samples, and within each material condition, that are communicating to the liquid. This is derived from the fact that Nyquist plots have an arc radius whose center point is often below the Z’ axis, implying that instead of a single oxide thickness, these oxides have a distribution of thicknesses. This distribution of thicknesses produces arcs that are not clearly separable in most of the samples. There were only two sample conditions that exhibited two separable arc distributions, Material 12-1 and Material 10, which exhibited EIS arcs that are consistent with dense oxide scales in the micron range. Samples Material 13 and Material 21 have EIS arcs that are consistent with oxide scales in the tenths of a micron, and the remaining samples exhibited further arcs in the nanometer range as well.

6.0 Acknowledgements

This work was funded through the Department of Energy-Nuclear Energy National User Science Facility at Idaho National Laboratory. The authors would like to acknowledge the assistance of Alan Schemer-Kohrn for his help in working with the radioactive samples. We wish to acknowledge the help of Kayla Yano in conducting TEM preparation and examination of TEM foils. We also express our appreciation for the assistance of Rob Seffens and Ferdinan Colon, who worked with Ramprashad Prabhakaran to resolve some of the issues with leaking around the instrumentation feedthroughs and continuity issues inside the autoclave. The authors would also like to acknowledge Dave Senor for technical editing.

7.0 References

[1] T. Miyashita et al., “Corrosion and hydrogen pickup behaviors of cladding and structural components in BWR high burnup 9x9 lead use assemblies”, ANS LWR Fuel Performance Conference, San Francisco, 2007, paper 1015.

[2] Draft Regulatory Guide DG-1263, Establishing analytical limits for zirconium-based alloy cladding, NRC-2012-0043-0002_DG-1263, March 2014.

[3] Waterside corrosion of zirconium alloys in nuclear power plants, IAEA-TECDOC-996.

[4] F. Garzarolli, B. Cox and P. Rudling, “Optimization of Zry-2 for high burnups”, 16th ASTM Symposium, Chengdu, China, 2010, pp. 711.

[5] A. Shivprasad, A. T. Motta, A. Kucuk, S. Yagnik, Z. Cai, “Microbeam X-ray absorption near-edge spectroscopic studies of high-burnup Zircaloy-2 oxide layers”, 18th International Symposium on Zirconium in the Nuclear Industry, May 15-19 2016.

[6] A. Kucuk, “High hydrogen pickup at high burnup in BWRs”, Proceedings of ANS Top Fuel 2016, September 14, 2016.

[7] A. Couet, A.T. Motta, R.J. Comstock, A. Ambard, “Hydrogen pickup mechanism in zirconium alloys”, 18th International Symposium on Zirconium in the Nuclear Industry, May 15-19 2016.

[8] A. Couet, A. T. Motta, A. Ambard, D. Livigni, “In-situ electrochemical impedance spectroscopy measurements of zirconium alloy oxide conductivity: relationship to hydrogen pickup”, Corrosion Science, 119 (2017) 1-13.

[9] D. Rishel et al., “In-situ EIS measurements of irradiated Zircaloy-4 post-transition corrosion kinetics behavior”, 15th International Symposium on Zirconium in the Nuclear Industry, June 24-28, 2007. pp. 326.

[10] N. Ramasubramanian, P. Billot, and S. Yagnik, “Hydrogen evolution of pickup during the corrosion of zirconium alloys: A critical evolution of the solid state and porous oxide electrochemistry”, 13th International Symposium on Zirconium in the Nuclear Industry, June 10-14, 2001. pp. 222.

[11] M. Bojinov, L. Hansson-Lyyra, P. Kinnunen, T. Saario, and P. Sirkia, “In-situ studies of the oxide fil properties on BWR fuel cladding materials”, 14th International Symposium on Zirconium in the Nuclear Industry, June 13-14, 2004. pp.367.

[12] I Arimescu, “Heat flux HPU model: role of nickel in Zr-2,” Hydrogen Impacts in Zirconium Alloy Materials Panel, Proceedings of ANS Top Fuel 2016, September 14, 2016

[13] M. Lindgren, G. Sundell, I. Panas, L Halstadius, M. Thuvander, H-O Andren, “Towards a comprehensive understanding of hydrogen uptake in zirconium alloys by combining atom

probe analysis with electronic structure calculations," 17th International Symposium on Zirconium in the Nuclear Industry, Hyderabad, February 3-7, 2013. pp. 515.

[14] E. Fromm and H. Uchida, "Surface phenomena in hydrogen absorption kinetics of metals and intermetallic compounds," Jo. Of the Less-Common Metals, 131 (1987) 1-12.

[15] H. H. Uchida, H.-G. Wulz and E. Fromm, "Catalytic effect of nickel, iron and palladium on hydriding titanium and storage materials," Jo. Of the Less-Common Metals, 172-174 (1991) 1076-1083.

[16] P. Bossis et al, "Study of the mechanisms controlling the oxide growth under irradiation: characterization of irradiated Zircaloy-4 and Zr-1Nb-O oxide scales," Thirteenth International Symposium on Zirconium in the Nuclear Industry, Annecy, June 10-14, 2001. pp. 190.

[17] R. Prabhakaran, et al., "Progress report on improved understanding of Zr-2 hydrogen pickup mechanisms in BWRs", PNNL-28573, Pacific Northwest National Laboratory, Richland, WA, March 2019.

[18] R. Prabhakaran, et al., "FY20 Report: Improved Understanding of Zr-2 Hydrogen Pickup Mechanisms in BWRs", PNNL- 30477, Pacific Northwest National Laboratory, Richland, WA, September 2020.

[19] Gebhardt, A phase reference procedure for interpretation of impedance spectroscopy experiments, Electrochimica Acta, Vol. 38. No. 5, pp. 633-641, 1993.

[20] Gebhardt & Hermann, "Microscopic and electrochemical impedance spectroscopy analyses of Zircaloy oxide films formed in highly concentrated LiOH solution", Electrochimica Acta, Vol. 41. No. 7-8. pp. 1181-1190 (1996).

[21] Schefold, et al., "The cyclic nature of corrosion of Zr and Zr-Sn in high-temperature water (633 K): A aong-term in situ impedance spectroscopic study", Journal of the Electrochem Society, 150 (10) B451-B461 (2003).

[22] Durand-Keklikian, et al., In situ A.C. impedance studies of oxide film growth on Zircaloy-4 in high temperature/high pressure steam, Corrosion Science, Vol. 32, No. 3, pp. 361-365, 1991.

[23] S. Forsberg, E. Ahlberg, U. Andersson, "Studies of corrosion of cladding materials in simulated BWR-environment using impedance spectroscopy", SKI report 2004:54, September 2004.

8.0 Appendix

8.1 Test fixture designs used by other researchers

PNNL conducted a literature survey and obtained EIS test fixture designs utilized by other researchers. Most of these fixtures were designed for conducting EIS testing of unirradiated samples in the form of tubes, which is much easier to handle, and test compared to small and thin neutron-irradiated rectangular and curved specimens. In some articles, critical information was missing, such as performance of various insulating media used at different temperatures; fixture design; specimen geometry and others. Examples of fixtures utilized by other researchers are shown below.

8.1.1 Studsvik's design for room temperature testing of Zr tubes

During October 2019, EPRI shared the fixture design that was employed by Studsvik for testing unirradiated oxidized Zr tubes at room temperature. This design could not be utilized at PNNL for testing irradiated fuel channels and water rods for two reasons: higher test temperature (288ºC) and complex specimen geometry (rectangular pieces or curved sections).

8.1.2 Gebhardt's setup

As per the Gebhardt's setup shown in Figure 93, a cylindrical tube specimen was positioned between two watertight overlapping plastic end pieces [19-20]. This was utilized for testing at room temperature and 80°C. This design prevented the penetration of the electrolyte to the inner surface of the specimen.

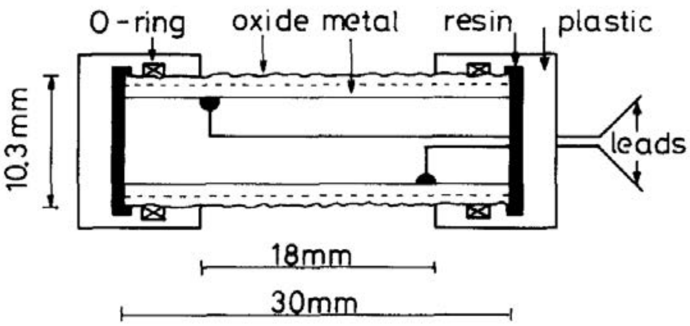

Figure 93: Gebhardt's setup for testing cylindrical tube specimen at room temperature and 80ºC[19-20]

8.1.3 Schefold's setup

As per Schefold's setup shown in Figure 94, a perforated Pt cylinder served as a coaxial counter electrode for a Zr-Sn sample (about 1 mm electrode distance), leading to a symmetrical two-electrode configuration [21]. Test parameters were: Oxygen-free pressurized water at 360°C, with 0.1 wt % B as H_3BO_3 and 2-5 ppm Li as LiOH for pH stabilization as electrolyte in a static autoclave pressure of 18 MPa (2600 psi)

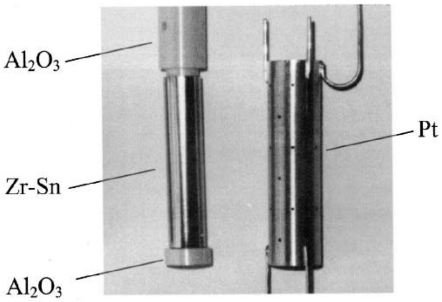

Figure 1. Cell elements for high-temperature IS: Zr-Sn sample with ceramic seals (contact wire inside ceramics) and Pt counter/reference electrode for coaxial mounting.

Figure 94: Schefold's setup[21] for testing cylindrical tube specimen at 360°C

8.1.4 Couet's setup

Couet et al. performed in-situ EIS experiments on Zircaloy-4 and Zr-2.5Nb in 360°C water [8]. Electrical feedthroughs were provided by Pt wires in cooled Teflon seal elements at the top of the autoclave. A zirconium alloy tube served as the working electrode. A perforated Pt cylinder served as coaxial quasi-reference electrode, as shown in Figure 95. This electrode was placed at an approximate distance of 0.5 mm between the electrodes leading to a symmetrical two-electrode configuration. A two-electrode cell was used, since electrochemical reactions at the Pt electrode are much faster than at the Zr electrode making the Pt electrode a very good quasi-reference electrode. Tube ends were isolated with spring-loaded Al_2O_3 ceramic caps, leaving an exposed outer surface area of about 8 cm^2. The connectivity between the tubes and the Pt wire was maintained by welding a Zr-Sn wire to the inside of the tube.

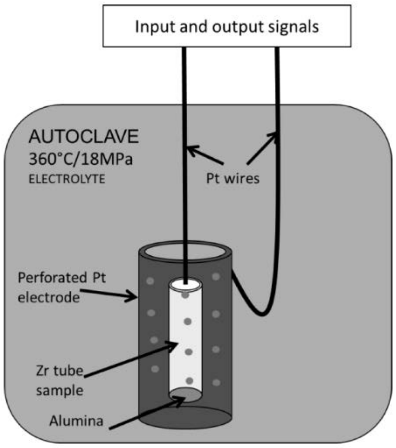

Figure 95: Couet's setup[8] for EIS testing of unirradiated Zr tube samples in 360°C water

8.1.5 Durand-Keklikian's setup

As per Durand-Keklikian's setup, in situ A.C. impedance measurements were carried out to study the electrical properties of the oxide films formed on as-received Zr-4 exposed to steam at 500°C and 650 psi [22]. A three-electrode configuration commonly used for measuring interfacial impedance as a function of frequency poses undue mechanical and cell fabrication constraints on high temperature, in situ studies. Hence, a two-electrode configuration, in which Zr-4 and spring-loaded graphite utilized as the electrodes were used for studying interfacial impedance as a function of frequency in steam.

The specimen probe (upper and lower ends) shown in Figure 96 on the left and right, respectively were designed to introduce the specimen into the test section, and to permit wide frequency band-width impedance measurements to be carried out on the growing oxide film as a function of time. The test section (Figure 96: right) had four openings through which four specimens were introduced into the high-pressure steam environment. In order to perform impedance measurements, it was necessary to establish a reproducible electrical contact with the outer surface of the oxide film. This was done by using a spring-loaded graphite contact as described below.

During periods between impedance measurements, the graphite contact was withdrawn from the surface to ensure unimpeded access of the steam to the specimen surface. Mechanical contact between the graphite and the specimen was established with a constant (and reproducible) force maintained by a spring situated under the specimen (see Figure 96: right). The contact force was readily varied by adjusting the thrust nut located outside the pressure boundary at the upper end of the specimen probe, as shown in Figure 96 (left). The graphite and the specimen were both located in a steel housing in which two openings allowed the steam to circulate above the specimen surface, as shown in Figure 96 (right). The graphite and the specimen were both insulated from the test section structure by alumina tubing.

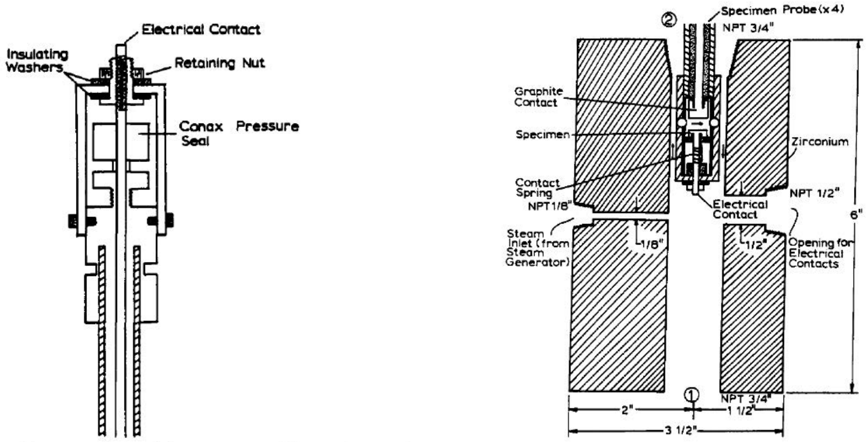

FIG. 1. Schematic of the test section and the upper part of the specimen probe.

FIG. 2. Schematic of the test section and the lower part of the specimen probe.

Figure 96: Durand-Keklikian's setup[22] for EIS testing of samples in steam at 500°C and 650 psi